Spring 2015

# Investigation of effect of process parameters on multilayer builds by direct metal deposition

Tarak Amine



Department: Mechanical and Aerospace Engineering

# INVESTIGATION OF EFFECT OF PROCESS PARAMETERS ON MULTILAYER BUILDS BY DIRECT METAL DEPOSITION

by

TARAK AMINE

A DISSERTATION

Presented to the Faculty of the Graduate School of the

MISSOURI UNIVERSITY OF SCIENCE AND TECHNOLOGY

In Partial Fulfillment of the Requirements for the Degree

DOCTOR OF PHILOSOPHY

in

MECHANICAL ENGINEERING

2015

Approved
Frank Liou, Advisor
Joseph W. Newkirk, Co-Advisor
K. Chandrashekhara
Hailung Tsai
V.A. Samaranayake

## PUBLICATION DISSERTATION OPTION

This dissertation has been prepared in the university format. Five journal articles are presented. Page 3 to 20 *"Numerical simulation of the thermal history multiple laser deposited layers"* is in the style required by International Journal Advanced Manufacturing Technology. It has been accepted and published. Page 21 to 42 *"An investigation of the effect of laser deposition parameters on characteristics of multilayered 316 l deposits"* is in the style required by International Journal Advanced Manufacturing Technology. It has been accepted and published. Page 44 to 65 *"Microstructural and hardness investigation of tool steel d2 processed by laser surface melting and alloying"* is in the style required by International Journal Advanced Manufacturing Technology. It has been accepted and published. . Page 67 to 100 *"Investigation of effect of process parameters on multilayer builds by direct metal deposition"* is in the style required by Applied Thermal Engineering. It has been accepted and published. Page 102 to 123 *"Methodology for studying effect of cooling rate during laser deposition on microstructure"* has been submitted to Journal of Materials Engineering and Performance.

## ABSTRACT

Multilayer direct laser deposition (DLD) is a fabrication process through which parts are fabricated by creating a molten pool into which metal powder is injected as. During fabrication, complex thermal activity occurs in different regions of the build; for example, newly deposited layers will reheat previously deposited layers. The objective of this study was to provide insight into the thermal activity that occurs during the DLD process. This work focused on the effect of the deposition parameters of deposited layers on the microstructure and mechanical properties of the previously deposited layers. Varying the parameters was shown to produce different effects on the microstructure morphology and property values, presumably resulting from in-situ quench and tempering. A commercial ABAQUS/CAE software was used to model this process by developing a thermo-mechanical 3D finite element model. This work presents a 3D heat transfer model that considers the continuous addition of mass in front of a moving laser beam using ABAQUS/CAE software. The model assumes the deposit geometry appropriate to each experimental condition and calculates the temperature distribution, cooling rates and re-melted layer depth, which can affect the final microstructure. Model simulations were qualitatively compared with experimental results acquired in situ using a K-type thermocouple.

Moreover, the work focused on the effect of cooling rate and other processing variables on microstructure and mechanical properties. The influence of the cooling rate on the microstructure and mechanical properties was investigated. The differed cooling rate led to varied grain size and resulted in affected varied hardness and tensile strength.

# ACKNOWLEDGMENTS

I wish to express my sincere appreciation to my thesis committee, including Dr. Frank Liou, Dr. Joseph W. Newkirk, Dr. K. Chandrashekhara, Dr. Hailung Tsai, and Dr. V.A. Samaranayake for their valuable advice and support.

My deepest gratitude goes to my advisor Dr. Frank Liou and my Co-advisor Dr. Joseph W. Newkirk for their guidance, encouragement and support throughout this thesis work. Their hardworking and rigorous scientific has influenced every aspect of my life. I learned from them more than anyone about laser deposition process, rapid prototyping, metallurgy.

Finally, I wish to express my deep gratitude to my parents and sister for their encouragement, understanding, patience and love.

# TABLE OF CONTENTS

# LIST OF ILLUSTRATIONS

Page

PAPER I



PAPER II

# LIST OF TABLES

Page

# 1. INTRODUCTION

In the direct laser deposition (DLD) process, the material in a single deposited layer typically is not enough to create a part. Several layers must be deposited to achieve a fully built part. With each newly deposited layer, the previously deposited layers begin to reheat, just one example of the multiple temperature gradients at play in the additive layering process that influence the material deposition.

The thermal behavior that occurs during the DLD process results in a complex microstructure evolution. Attributable to its stepwise additive nature, the thermal cycles associated with the DLD process can involve several reheating cycles. Thus, the goal of any assessment of microstructural evolution is to determine the response of the alloy to these cycles [1].

During the DLD process, the complex thermal distribution resulting from the repeated non-uniform heating and cooling process not only affects the mechanical performance and the post-machining precision of the fabricated component, but also results in fabricated component distortion, and possibly even cracking.

The microstructure of the material formed by the molten pool is related to the cooling rate during the solidification process. Further microstructural evolution takes place in the solid state depending on the subsequent temperature field and profiles developed within the samples as the laser is traversed during the build operation. Thus, it is important to control the temperature profiles during the DLD process so that an ideal microstructure can be achieved in the fabricated component. The most important DLD parameters include the laser power (W), travel speed (mm/min) and powder feed rate (g/min), which all significantly affect the microstructure of the formed parts [2].

The microstructure of DLD-fabricated materials clearly depends on the cooling rate and temperature gradient of the melt pool. Much research on the thermal behavior has concentrated on investigating the temperature distribution and cooling rate during the solidification process. However, the DLD process is more complicated than a series of successive solidifications of molten pools. During laser deposition, the previously deposited layers reheat when a new layer is deposited on top of them. The temperature of the sample varies from one location to another and from one point in time to another.

Ghosh (2006) developed a model to simulate the temperature distribution and residual stresses in the single-pass laser cladding process, which is very similar to DLD [3]. Giuliani (2009) developed a model to predict the powder temperature distribution for a laser with top-hat and Gaussian intensity distribution, as well as the temperature profile for a single-track laser [4]. Vahid et al. (2011) developed a model to simulate the shape and geometries of the real-time melt-pool and to predict the local solidification condition along the solid/liquid interface for a single-track laser [5]. However, it is important to understand and control the thermal behavior and reheating cycle attributed to building subsequent layers during the laser deposition process. So far, however, research on the effect of the reheating process that accompanies a multilayer build has been limited. In order to understand the evolution of and to control the microstructure, it is important to understand the thermal history of the deposited component during the DLD process, as was the focus of this work. Additionally, a transient thermal model of multi-thin wall multi-layers was developed to reveal the heating and reheating cycles during layer-by-layer deposition in the DLD process. The model was used to predict the temperature distribution, thermal gradient, re-melted layer depths, peak temperatures and cooling rate as a function of the DLD process parameters, such as laser travel speed (mm/min) and laser power (W).

The temperature history during the DLD process was measured by three thermocouples positioned to validate the model on the underneath surface of the substrate at the midpoint and ends of the laser track. The locations at which temperatures were measured were determined from finite element analysis (FEA) model; regions were selected in which the temperatures would not damage the thermocouples. These locations will be referred to as the reference positions for the measured temperatures. The thermocouples were connected via an interface box to a computer that monitored the temperatures at those positions during material deposition. The modeling results were qualitatively compared with experimental results acquired in situ using a K-type thermocouple. Moreover, the model ensures a constant molten pool temperature consistent with the number of deposited layers by reducing the laser power and increasing the laser travel speed as more layers are deposited.

**PAPER**

# I. NUMERICAL SIMULATION OF THE THERMAL HISTORY MULTIPLE LASER DEPOSITED LAYERS

Tarak Amine, Joseph W. Newkirk and Frank Liou

International Journal Advanced Manufacturing Technology

Received: 13 September 2013 /Accepted: 14 May 2014



**ABSTRACT**

Multilayer direct laser metal deposition is a fabrication process in which the parts are fabricated by creating a molten pool into which metal powder particles are injected, and a layer is laid down by moving the pool. Height is added by creating additional layers on top of the first layer. During fabrication, a complex thermal history is experienced in different regions of the build. The thermal history includes the reheating process for previously deposited layers caused by subsequently deposited layers. The objective of this study is to provide insight into the thermal history during the direct laser deposition process. Using the commercial ABAQUS/CAE software, a thermomechanical 3D finite element model was developed. This work presents a 3D heat transfer model that considers the continuous addition of powder particles in the front of a moving laser beam using ABAQUS/CAE software. The model assumes the deposit geometry appropriate to each experimental condition and calculates temperature distribution, cooling rates, and remelted layer depth which can affect the final microstructure. Model simulations were qualitatively compared with experiments results acquired in situ using a Ktype thermocouple.

**Keywords:** Direct laser deposition process, 3D finite element modeling, heat transfer

# 1. INTRODUCTION

Over the last few years, the technology of direct laser deposition (DLD) has gained increasing interest in the industry for rapid manufacture, repair of parts, and modification of metallic components. Building a part involves the application of a concentrated laser beam on the substrate to create a small melt pool into which powder particles are injected. As the laser beam moves away, the molten material solidifies thereby creating the shape for each layer. After depositing a layer, the laser beam with powder delivery nozzle is raised up an incremental distance and a new layer is started. The next layer remelts some of the previous layer and upon solidification the two layers are joined by a strong metallurgical bond. Consecutive layers are sequentially deposited, thereby creating a three-dimensional metal component. In addition to the remelting of the previous layer's top surface, several previous layers may see some degree of reheating. Thus, the layering process will cause multiple temperature gradients during the course of the deposition.

Some finite element modeling studies have been reported for the application of some materials including titanium alloys, stainless steel alloys, nickel-based alloys, tool steel and other specialty materials, as well as composite and functionally graded material deposition using simultaneous feed of powder and wire in DLD processing with single layer. Fu (2010) developed a model to simulate the temperature distribution and residual stresses in the single-pass powder laser deposition process, the results showed that less difference of thermal conductivity and thermal expansion coefficient between powder material and substrate material produces lower residual stress; higher laser power, laser scanning speed, and smaller laser beam diameter can lead to higher peak temperature and higher residual stress [1]. Giuliani (2009) developed a model to predict the powder temperature distribution for a laser with top-hat and Gaussian intensity distribution, as well as the temperature profile for a single-track laser The results showed that a more vertical position of powder delivery nozzle will lead to a higher and more uniform particle temperature distribution, in particular for the top-hat intensity distribution case [2]. Vahid et al. (2011) developed a model to simulate the shape and geometries of the real-time melt pool and to predict the local solidification condition along the solid/liquid

interface for a single-track laser, the temperature gradient and interface velocity can be accurately evaluated along the predicted solid/ liquid interface [3]. However, it is important to understand the thermal behavior and reheating cycle attributed to building subsequent layers during the laser deposition process, and subsequently to control it. In this work, a transient thermal model of multithin wall multilayers was developed to reveal the heating and reheating cycles during layer by layer deposition in the (DLD) process. The model assumes certain geometries appropriate to process parameter combinations and was used to predict the temperature distribution, thermal gradient, remelted layer depths, peak temperatures, and cooling rate as a function of process parameters, such as laser travel speed (mm/min) and laser power (W) which can affect the final microstructure and elemental distribution in the part as well as the mechanical properties of deposited material.

In order to validate the model, the temperature history during the (DLD) process was experimentally measured by three Ktype thermocouples positioned on the underneath surface of the substrate at the midpoint and the ends of the laser track. The depth was varied such that the thermocouples were located 1, 2, and 3 mm below the top surface of the substrate as shown in Fig. 1.1. These locations were evaluated with the FEA model output as ones where the temperatures attained in that region would not damage the thermocouples. These locations will be referred to as the reference positions for the measured temperatures. The temperatures were recorded with a data logging system at a rate of 100 Hz reading per second. The data logging system was initiated prior to the deposition and continued for several minutes after the deposition had finished. The thermocouples were connected via an interface box to a computer that monitored the temperatures at those positions during material deposition. As a result, the whole thermal history of the instrumented locations during the deposition process, including the cooling period after the deposition, was recorded. The modeling results were compared with the experimental results. The model is important to determine the parameters that would assure a constant molten pool temperature consistent with a multilayer deposition and therefore this validation step is critical in the development of this model.

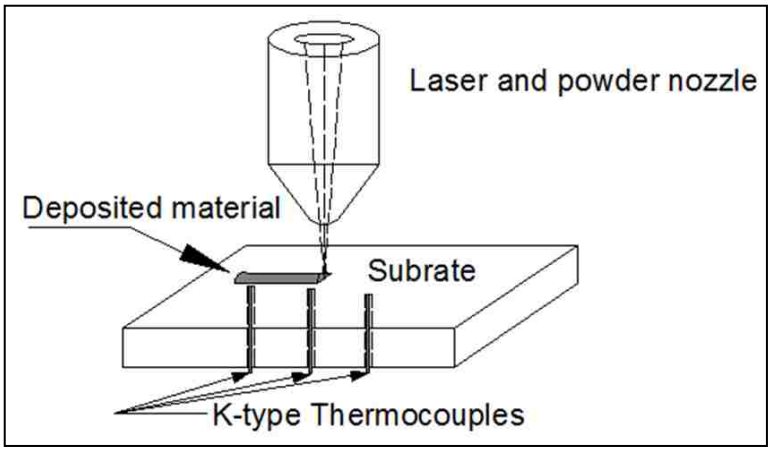


Figure 1.1. Scheme for locating thermocouples on the substrate

# 2. THERMAL MODELING

Figure 2.1 depicts a flow chart showing various steps in the computational scheme employed in the study. The entire deposition process was modeled as a multistep transient heat transfer analysis in which each time step was further divided into a number of smaller time increments. The continuous addition of metal powders was considered by means of the successive, discrete addition of a new set of elements into the computational domain at the beginning of each time step, which was fixed such that the laser beam scanned a distance equal to a set of newly activated elements.

The number of elements activated at each time step was determined from the volume of powder materials expected to enter the melt pool during that time step, which depended on powder feed rate (f), and the travel speed of the laser (v).

A 3D finite element temperature field model for DLD developed by ABAQUS/CAE software demonstrated the model's thermal history in stainless steel SS316L. Transient thermal analysis first was performed within ABAQUS/CAE to determine the temperature history at each point of interest in the deposited material. Eq. (1) is the heat conduction governing equation:

$$\frac{\partial}{\partial x}\left(K\frac{\partial T}{\partial x}\right)+\frac{\partial}{\partial y}\left(K\frac{\partial T}{\partial x}\right)+\frac{\partial}{\partial z}\left(K\frac{\partial T}{\partial z}\right)=\rho Cp\frac{\partial T}{\partial t} \qquad (1)$$

where ρ, Cp, and K refer to density, specific heat, and thermal conductivity, respectively of the metal powder and the substrate material; T and t refer to temperature and time variable, respectively. The terms on the left side of the Eq. (1) refer conductivity heat transfer in x, y, and z directions, respectively. The term on the right side of the Eq. (1) refer to the transient nature of the heat transfer process.

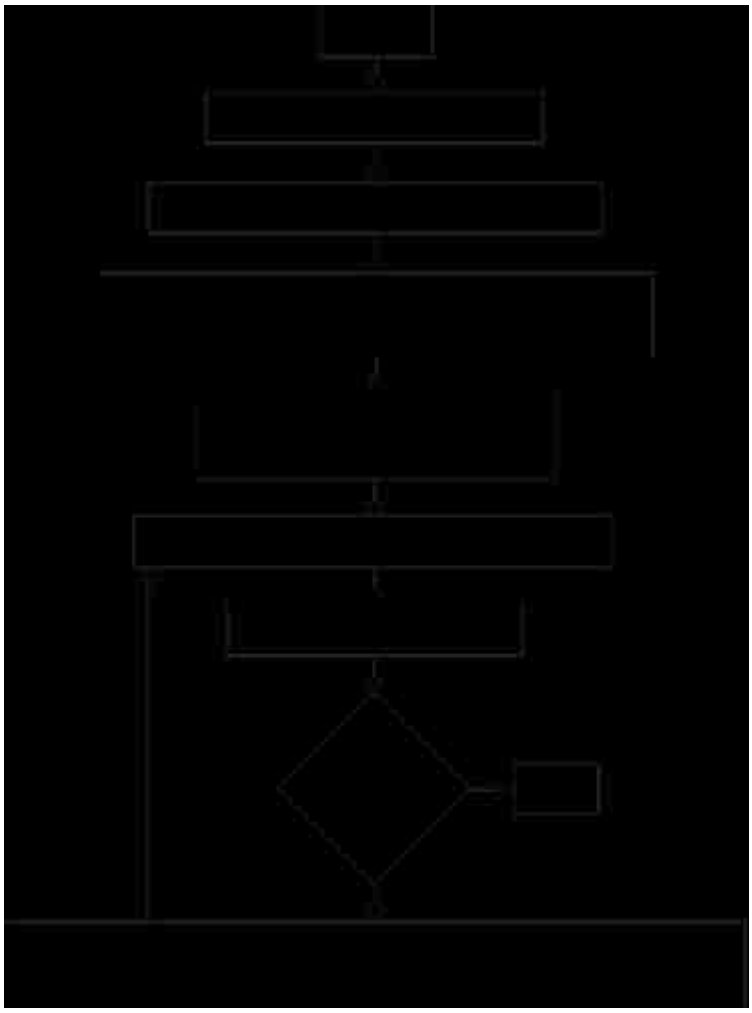

Figure 2.1. Flow chart showing various steps involved in the temperature distribution model

The first step began with a substrate material, T0, initially at room temperature, as shown in Eq. (2). At beginning of each subsequent step, a new group of finite elements was activated.

$$T(x, y, z) = T_0 \qquad (2)$$

Given the melt generation and resolidification associated with the phase change effects, the specific material properties used as inputs in the current analysis were

density, thermal conductivity (k), specific heat, expansion coefficient alpha, and latent heat for varying temperature ranges. Numerical values of these material properties as adopted from [4] and used in the analysis appear in Table 2.1. All substrate surfaces exposed to the environment were assumed to have lost heat due to free convection.

Table 2.1. Thermal material properties for stainless steel 316L as used in the finite element modeling

| Temperature (k) | 300 | 500 | 700 | 1000 |
|---|---|---|---|---|
| Specific heat (kj/kg k) | 468 | 527 | 563 | 602 |
| Expansion Coefficient alpha (m/mk) | 1.52E-5 | 1.69E-5 | 1.79E-5 | 1.88E-5 |
| conductivity (w/mk) | 13.4 | 16.75 | 19.8 | 24.2 |

In order to simulate mass addition (powder deposition), the "birth and death" feature in ABAQUS/CAE was used. Initially, all elements in the deposited track were "killed." The total time required for the laser beam to travel along the deposited track of each layer was divided into a number of small time steps to which variable flux and boundary conditions were applied. The first born of the element set appeared with applying these conditions. For the subsequent element sets, the model used the results of the previous step as the initial condition for the new active element set.

Finally, according to Rosenthal's Eq. (3), the moving heat source was simulated by applying a concentrated surface heat flux on the model for a time equal to the distance between the model element sets divided by the laser travel speed. A user subroutine was written to calculate the position of the laser at a given time as a function of its speed (v) and the Gaussian flux distribution in terms of spatial coordinates.

In DLD process, a moving laser beam strikes on the substrate at time t=0. The metal powder being added gets melted and subsequently solidified after cooling to form the deposit. The transient temperature distribution T(x,y,z,t) is obtained from the three-dimensional heat conduction equation in the substrate as:

$$\rho Cp\frac{\partial T}{\partial t}+\rho Cp\nabla.(vT)-\nabla.(K\nabla T)=Q \qquad (3)$$

where T is temperature filed, Q is the power generation per unit volume of the material (W/m3), K is the thermal conductivity (W/mK), Cp is specific heat capacity (J/kgK), ρ is density (kg/m3), t is time (s), and v is the travel speed (m/s).

As assumed in the simulation, the interaction of the heat flux with both the substrate and the deposited material follows the schematic in Fig. 2.2, such that at time t during beam scanning, the heat flux as the source of heat from the laser beam was modeled at the location Lt on the surface of the substrate along the path of scanning. This simulated the impingement of the laser beam onto this surface at that instant, resulting in the generation of the melt pool. The deposit was the solidified volume of powder particles added into the melt pool, so it was modeled on top of the heat source to simulate the volume of added powder particles.As the beammoves to a new location after a time t+dt, the heat flux correspondingly moved to the location, Lt+dt, with vdt being the length of deposited material over the incremental time dt.

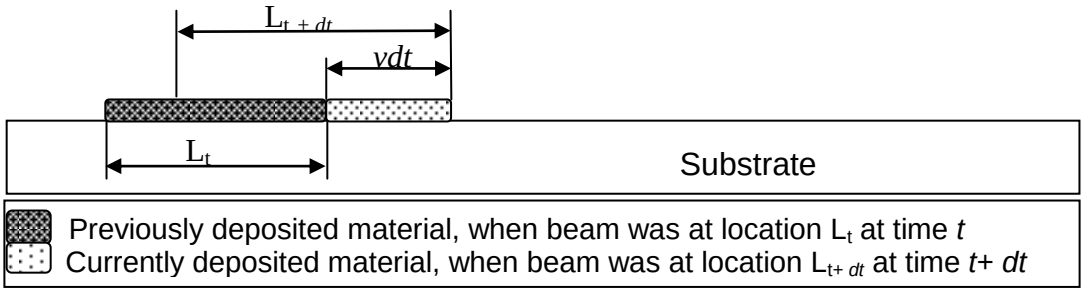


Figure 2.2. Schematic illustration of beam/substrate interaction substrate at different times during beam scanning and length of clad, vdt, which is manufactured in every scan over a time of dt

The analysis was divided into several steps in order to move the heat flux from the laser over the nodes in the laser path. The process parameter combinations used in the

model and also in the experimental runs are shown in Table 2.2. DOE model was used with three levels for each of the three parameters. The DOE was repeated for build schemes which used a zigzag laser scan versus a parallel laser scan. Residual stress was not investigated in this study.

Table 2.2. Process conditions monitored

| Sample # | Laser power(w) | Traveling speed (mm/min) | Powder feed rate (g/min) |
|---|---|---|---|
| 1 | 600 | 300 | 8 |
| 2 | 600 | 375 | 10 |
| 3 | 600 | 450 | 12 |
| 4 | 750 | 300 | 10 |
| 5 | 750 | 375 | 12 |
| 6 | 750 | 450 | 8 |
| 7 | 900 | 300 | 12 |
| 8 | 900 | 375 | 8 |
| 9 | 900 | 450 | 10 |

## 2.1. GEOMETRIC MODEL OF THIN WALL

In order to predict the temperature distribution of the deposited thin wall in the DLD process, a 3D finite element and meshes were built using Hypermesh software, as shown in Fig. 2.3. The mesh on the geometry, which represents its discretization into the elemental form, is made of thermal 8-node linear brick type elements. It was generated such that the wall region, where fusion occurs and more severe temperature gradients are expected, was assigned the finest mesh, and regions further from the wall were assigned a relatively coarse mesh [5–8]. The DLD process was simulated using ABAQUS/CAE.

The structure of the deposited thin wall in the modeling was built by depositing multiple single layer tracks on top of each other with a length of 30 mm, height of 14 mm, and width of 2.5 mm. The wall was fabricated on a substrate of 316L stainless steel

that was 50 mm wide, 50 mm long, and 12.7 mm thick, as shown in Fig. 2.3. To simulate the laser deposition process, the following assumptions were made:

- An initial temperature of the workpiece was assumed as 295 K. The workpiece and the coordinate mesh were fixed. The laser beam was moved in positive and negative Z-direction with a constant speed v. For newly deposited layers, the laser beam was moved up in positive Ydirection.
- A subroutine was written to consider the effect of conduction, convection, and radiation during the laser deposition process.
- The following boundary conditions were applied to the deposited thin wall:

$$q = -h(T - T_0)$$
$$q = \sigma(T^4 - T_0^4)$$

where q is heat flux per unit area, h is the convective heat transfer coefficient is emissivity, σ is the Stephan-Boltzmann constant, and $T_0$ is ambient temperature.

- The thermophysical properties for stainless steel 316L was considered as function of temperature as illustrated in Table 2.1.
- A radiation boundary condition was applied to the entire deposited thin wall and the emissivity was assigned a value 0.4.

The thin walls were built using a 1-kW diode laser, a multiaxis numerical control working table, and a powder feeder with coaxial nozzle.

The thermal load applied as a function of the distance for a Gaussian beam was determined using Eq. 4

$$DFLUX(1) = -q(0) \times e^{-cr^2} \qquad (4)$$

where r=x2+y2+z12, and z1=z−v(T−t). v is the speed of movement in z-direction, T is the lag factor that defines the time at which of the laser gun is at first position, t is time, z1 is movement along z-axis, and z is a fixed coordinate axis.

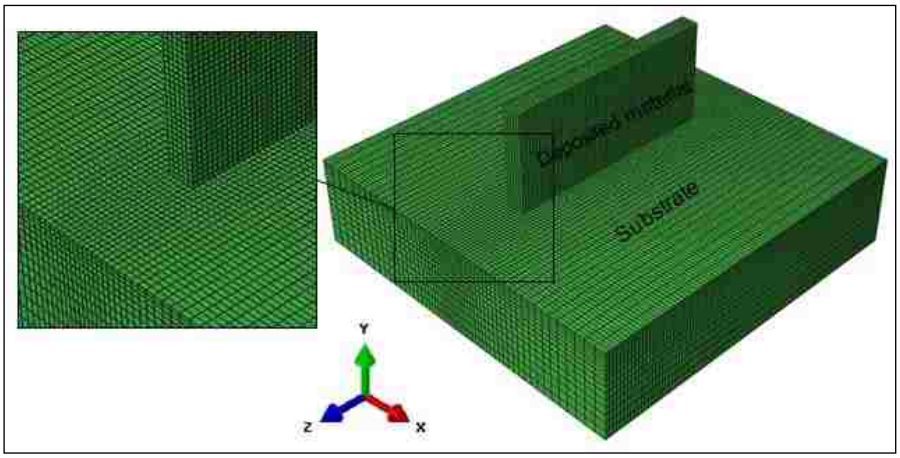


Figure 2.3. Three D finite element model build and meshes using Hypermesh software

## 3. RESULTS AND DISCUSSIONS

Figure 3.1 illustrates the transient temperature distribution contour plot for the first deposited layer for the case of laser power=600 W and travel speed=300 mm/min. The location of the laser beam is evident from the intensity of the temperature distribution, where the maximum contour limit of 1,996 °C signifies the melt pool. The thermal history was essentially independent of the vertical free edges once the laser reached the center of the wall, where the mesh was highly refined, as shown in Fig. 2.3, for accurate extraction of the thermal gradient and cooling rate.

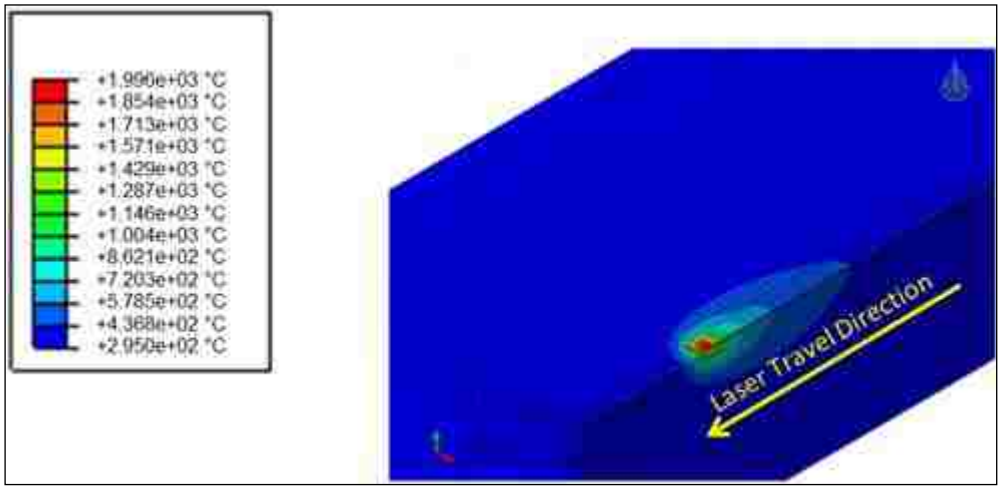


Figure 3.1. Temperature contours for Q=600 Wand V=300 mm/min

Figure 3.2a and b illustrates the temperature distribution along the deposited layers and substrate simulated using the defined laser parameters. The temperature of each nodal point within the solid was calculated as a function of time. The bottom of the deposited layers cooled faster than the top because of heat conduction to the substrate, while showing significant temperature gradients along the height of the deposited layers.

Thermal energy from the laser increased the node temperature beyond the melting temperature. Once the laser moved away along its track, the node began to cool. The next

pass of the laser caused the temperature of that node to increase higher than during the previous laser pass.

As seen in Fig. 3.2a and b, the numerical results are similar to the experimental. The simulated results for different values of absorptivity were compared with the experimental results, and a maximum error of approximately 20 % was observed in the simulated results for absorptivity of 0.6. The difference in the measurement compared to the model was approximately 100 °C at the maximum temperature. Also, a slight phase shift is apparent between the graphs of the simulated and experimental graphs results. This difference was somewhat reduced during the cooling stage; this difference in temperature between model and experiment has been observed by other experiments [7, 9]. One explanation was that the acceleration/deceleration of the laser and the dwell times while changing laser tracks between layers was not considered in the model [7]. Another explanation for the difference in temperature is that it may be caused by the differences of the real material properties, processing conditions, shielding gas, and powder delivery gas, and those from the literature that were used in the modeling.

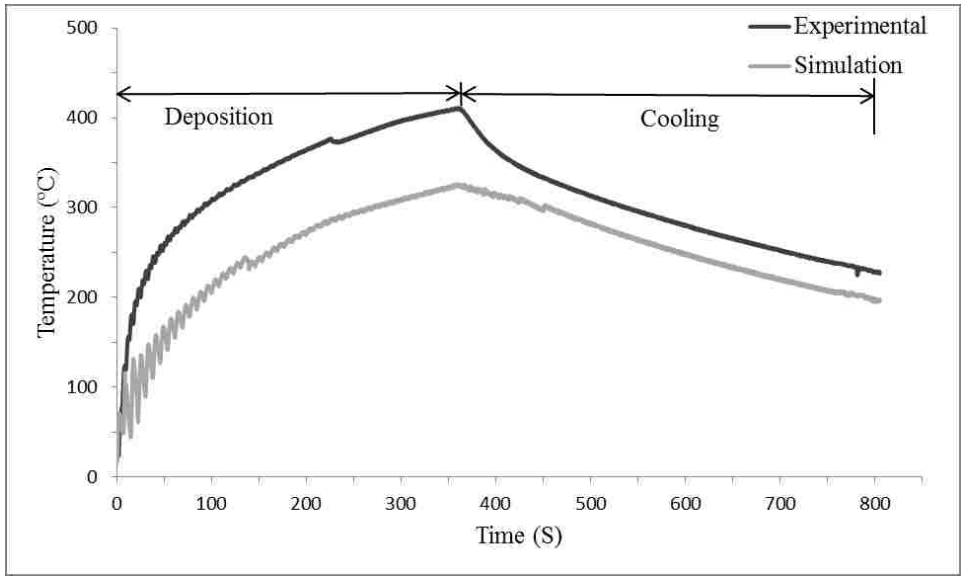


a

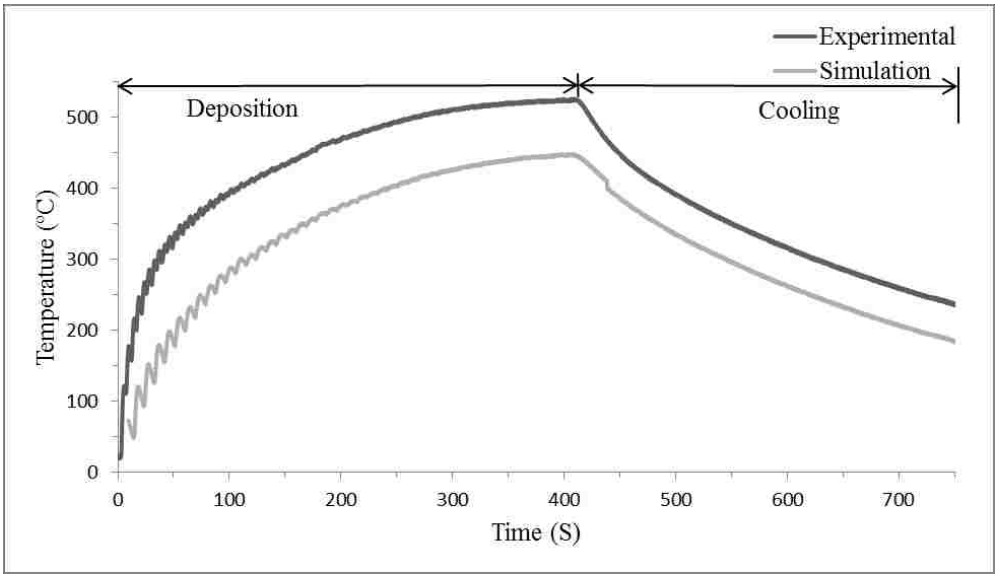


b

Figure 3.2. The simulation and experimental results comparison predicted at the reference position, a 600 W, 450 mm/min, 12 g/min and b 900 W, 375 mm/min, 8 g/min

The cooling rate of the FEA model was extracted from the time difference between when the nodes in the center of the deposited material were seen at the last

liquids temperature and at the next solidus temperature. At each nodal location, the solidification cooling rate was determined using Eq. (6):

$$\frac{\partial T}{\partial t} = \left|T_1 - T_S\right| / \left|t_1 - t_s\right| \quad (6)$$

Where dT/dt is the cooling rate, $T_l - T_s$ is the difference between the liquids and solid temperatures, and $t_l - t_s$ is the time interval between $T_l$ and $T_s$.

The computed results of the FEA model showed that the cooling rate of the thin wall was affected by the height of the built wall. The cooling rate was high at the beginning of the deposition process in the first and second layers because of the greater heat transferred to the substrate, but then it decreased with the addition of subsequent layers. The predicted cooling rate at the top of the build was 200 °C/s, while adjacent to the substrate was 5,500 °C/s. This large difference in the cooling rate could be detrimental to the building of a uniform microstructure. Controlling the laser power to follow the increasing height of the deposition would be required to alleviate this phenomenon.

The model was also used to predict the remelting depth during laser deposition, an important factor to consider. The frequent remelting of previous layers can lead to unwanted precipitation of phases or solutes, which can become detrimental metallurgically. Figure 3.3a and b shows the simulated remelted layer depths of deposited layers. These results were extracted from the simulation when the solidified node remelted (T>Tm) each time the laser beam passed over it. In general, the depths of the remelted layers were high, except for in the first layer, which was adjacent to the substrate and had difficulty melting completely because of the heat extraction by the substrate via heat conduction.

Figure 3.3a and b illustrates that the remelted depth accompanying the parallel laser scanning path was lower than that accompanying the zigzag path during the early stage of deposition because of the slightly higher cooling rate, though this effect eventually disappeared. Also, a lower laser power resulted in fewer remelted layers as a result of the higher cooling rate of the build wall.

Increasing the laser travel speed and/or decreasing the laser power reduced the melt pool depth. All of these extracted results provide important metallurgical information.

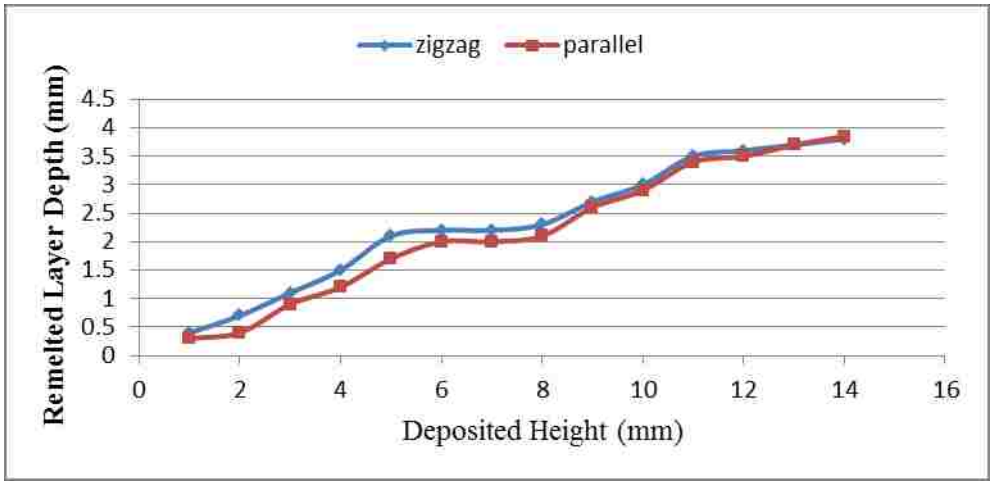


a

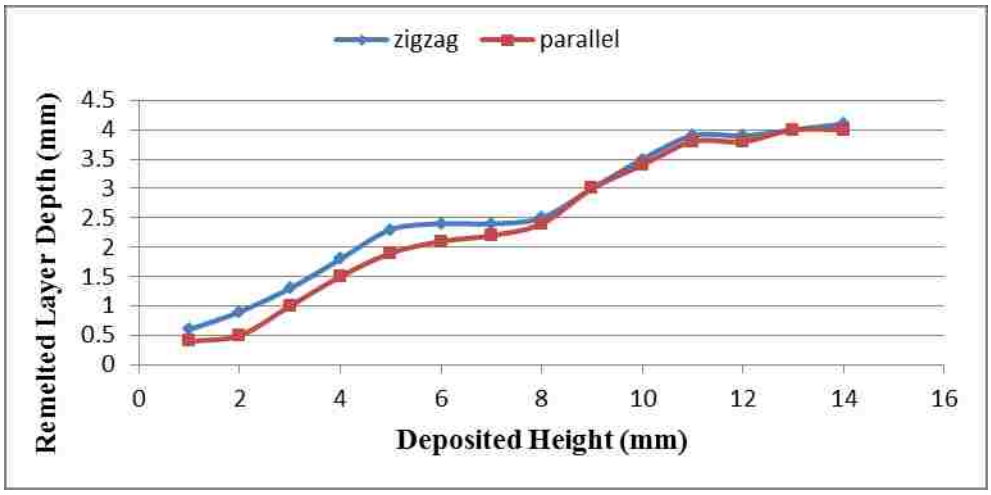


b

Figure 3.3. Computed remelted layer depth at a 600 W, 300 mm/min and b 900 W, 300 mm/min

# 4. CONCLUSION

The thermal behavior associated with the DLD process involves numerous reheating cycles. As a result, the temperature history of the deposited materials can be considered as a series of discrete pulses. A 3D transient thermomechanical finite model with a moving laser beam was developed to predict the temperature at any location and time during the laser deposition process. Element removal and reactivation technology was used in the modeling to realize the stepwise pattern of material addition.

The FEA model revealed the significant effects of the processing parameters, such as the laser power and travel speed. The results showed that increasing the laser power and/or decreasing the laser travel speed markedly increased the peak temperatures, cooling rates, and dimensions of the melt pool.

A k-type thermocouple was used to measure the temperature history of multiple layers of deposited material. The measurements were qualitatively and quantitatively compared with the prediction of the 3D transient thermomechanical finite model.

The model can be used to determine the laser parameters that would assure a constant molten pool temperature consistent with a multilayer deposition and therefore this validation step is critical in the development of this model. The model accurately predicted the shape of the heating and cooling curves but had a 20 % lower maximum temperature similar to what other experimenters have reported.

The remelted depth accompanying the parallel laser scanning path was lower than that for the zigzag path during the first layers to be deposited; therefore, the cooling rate was higher in the parallel path deposition when compared with the zigzag case. The remelted depth increased approximately linearly with layer height up to a total height of 14 mm for both parallel and zigzag cases, indicating that the cooling rate decreases with subsequent layers in this range of height values.

## REFERENCES


[1] Fu Y, Xie S, Xu X, Huang G, Cheng L, He Y (2010) Optimization of processing parameters for laser powder deposition using finite element method. J Wuhan Univ Technol Mater Sci Educ 25(5):832–837.

[2] Giuliani V, Hugo R, Gu P (2009) Powder particle temperature distribution in laser deposition technologies. Rapid Prototyp J 15(4):244– 254.

[3] Fallah V, Alimardani M, Corbin S, Khajepour A (2011) Temporal development of melt-pool morphology and clad geometry in laser powder deposition. Comput Mater Sci 50:2124–2134

[4] Goodfellow.Metals, alloys, compounds, ceramics, polymers, composites. Catalogue 1993/94.

[5] Abid M, Siddique M (2005) Numerical simulation to study the effect of tack welds and root gap on welding deformations and residual stresses of a pipe-flange joint. Int J Press Vessel Pip 82:860–871

[6] Long RS, Liu WJ, Xing F, Wang HB (2008) Numerical simulation of thermal behavior during laser metal deposition shaping. Trans Nonferrous Metals Soc China 18:691–699

[7] Deng D, Murakawa H (2006) Numerical simulation of temperature field and residual stress in multi-pass welds in stainless steel pipe and comparison with experimental measurements. Comput Mater Sci 37: 269–277

[8] JiaW, Tong H, HeW, Lin X, HuangW(2010) Numerical microstructure simulation of laser rapid forming 316L stainless steel. Acta Metall Sin (China) 46(2):135–140

[9] Qi H, Mazumder J (2006) Numerical simulation of heat transfer and fluid flow in coaxial laser cladding process for direct metal deposition. J Appl Phys 100:024903–1–024903–11

# II. AN INVESTIGATION OF THE EFFECT OF LASER DEPOSITION PARAMETERS ON CHARACTERISTICS OF MULTILAYERED 316 L DEPOSITS

Tarak Amine, Joseph W. Newkirk and Frank Liou

International Journal Advanced Manufacturing Technology
Received: 12 September 2013 /Accepted: 13 May 2014


**ABSTRACT**

A potential problem in applying the direct laser deposition (DLD) technique to material fabrication is the effect that subsequent deposited layers have on reheating previous laser deposition layers. Most of the previous investigations examined the effect of the laser deposition parameters on the microstructure and mechanical properties of a single layer. This work focused on the effect of the laser parameters of subsequent layers on the microstructure and mechanical properties of the deposited layers to select proper parameters and characterize the effect. The microstructure morphology and property values are affected by the varied parameters. This leads to some tempering and aging effects in the steels. The microstructure of the top layer was equiaxed, while the near substrate region was fine dendritic. Typically, both of the travel speed and power of the laser show the significant effects on microstructure and hardness.

**Keywords:** Laser deposition, Direct laser deposition (DLD) technique, Microstructure

# 1. INTRODUCTION

A single deposited material layer typically is not enough material deposition to create a part. Several layers have to be deposited in order to build a complete component. With each subsequent layer, previous layers may be reheated. The additive layering process causes multiple temperature gradients to influence the deposition.

The complex thermal behavior that occurs during the direct laser deposition (DLD) process results in a complex microstructural evolution. Mostly attributable to its stepwise additive nature, the thermal cycles associated with the DLD process can involve several reheating cycles as shown in Fig. 1.1. However, in building complex geometries, adjacent deposition tracks, junctions, and interrupted deposition could all add further reheating steps to a reference volume. Thus, the goal of any assessment of microstructural evolution is to determine the response of the deposited alloy to these cycles [1].

During the DLD process, the complex thermal history, resulting from the repeated non-uniform heating and cooling process, not only affects the mechanical performance and the post-machining precision of the fabricated component, but also results in fabricated component distortion, even possibly cracking.

The microstructure of the material formed from the molten pool is most strongly related to the cooling rate during the solidification process. Further microstructural evolution takes place in the solid state depending on the subsequent temperature field and profiles developed within the samples as the laser is traversed during the build operation. Thus it is important to control the temperature profiles during the DLD process so that an ideal microstructure can be achieved in the fabricated component. The most important parameters for the DLD process are laser power (W), travel speed (mm/min) and powder feed rate (g/min), which all have been suggested to have significant effects on the microstructure of the formed parts [2].

It is clear that the microstructure of fabricated materials by DLD depends on the cooling rate and the temperature gradient of the melt pool. A significant number of research efforts on the thermal behavior has concentrated on investigating the temperature distribution and cooling rate from the solidification process only. On the

other hand, the DLD process is more complicated than a series of successive solidification of molten pools. During laser deposition, the pervious deposition layers will be reheated when a new layer is deposited on top of them. The temperature of the sample varies from one location to another and from time to time.

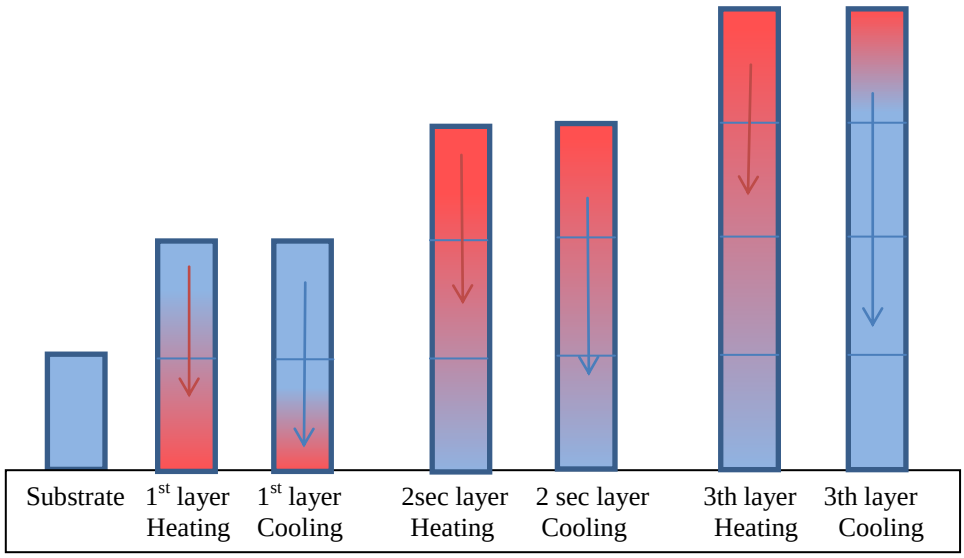


Figure 1.1. Schematic illustrating the method used to simulate additive layer deposition for multilayers

There have been a number of studies looking at deposition parameters on the resulting properties and structure. Zhang [3] carried out some experiments depositing 316SS to determine the influence of processing parameters on dilution ratio in the laser clad layer. The results showed that the influence of the degree of scanning speed is most significant, while that of laser power is relatively slight [3]. Wu [4] studied the effects of processing conditions, such as laser power, scan speed, and powder feed rate. On the microstructure of Ti–6Al–4 V. They concluded that the microstructure of deposited Ti–6Al–4 V is influenced by laser power, scan speed or powder feed rate, but the effects of each parameter are not straightforward [4]. Rasheedat [5] investigated the influence of the scanning velocity on the evolving physical properties, the microstructure, the microhardness and the wear resistance behavior of Ti6Al4V/TiC composite. The deposit

was crack free at scanning velocities between 0.015 and 0.105 m/s at an interval of 0.01 m/s. As the scanning velocity was increased, the microhardness also increased. Also, the wear resistance performance of the samples increased as the scanning velocity was increased [5].

Much fundamental research on the thermal behavior has concentrated on investigating the temperature distribution and cooling rate during the solidification process. However, the DLD process is more complicated than a series of successive solidifications of molten pools. As already stated, during laser deposition, the previously deposited layers reheat when a new layer is deposited on top of them. The temperature of the sample varies from one location to another and from one point in time to another. So far, however, there has been limited research on the effect of the reheating process which accompanies a multilayer build. In order to understand the evolution of the microstructure and control the microstructure, it is important to understand the thermal history of the deposited component during the DLD process.

# 2. EXPERIMENTAL PROCEDURE

The apparatus used for DLD consists of a 1-kW diode laser (coherent diode laser), a powder feeder and a 5-axis FADAL computer numerical control CNC (VMC3016. This system has been described in more detail previously [6]. A computer aided design (CAD) file and CNC control system were used to control the X and Y movement and Z increment. A diode laser of wavelength 808 nm (maximum power of 1 kW, spot size of 2.5 mm, top hat power profile) was used for materials processing. The influence of laser parameters on the shape and size of the laser melt pool is evaluated by specifying the power density (P), travel speed (v) and beam diameter (Db) as the specific energy (Es) by means of Eq. 1.

$$E_s = P/(D_b \times v) \quad (1)$$

A series of multilayer thin walls were deposited. The process parameter combinations used in the experimental runs are shown in Table 2.1. A DOE model was used with three levels for each of the three parameters. The values for laser power and powder mass feed rate are chosen on the basis of experience and previous experiments as being those values of specific energy and line mass close to the limits required for successful deposition. In order to examine the influences of these parameters on the microstructure and properties of the deposited layers, the change of the microstructure of the cross-sections of the deposited layers obtained at different laser powers and traveling speeds was observed and analyzed using a scanning electron microscope (SEM). Subsequently, the mechanical properties, such as hardness, were examined at different positions in the deposited wall layers.

The temperature history during the DLD process was experimentally measured by three K-type thermocouples positioned underneath the top surface of the substrate at the midpoint and the ends of the laser track. The depth was varied such that the thermocouples were located 1, 2, and 3 mm below the top surface of the substrate as shown in Fig. 2.1. The temperatures were recorded with a data logging system at a rate of 100 Hz. The data logging system was initiated prior to the deposition and continued for

several minutes after the deposition had finished. The thermocouples were connected via an interface box to a computer that monitored the temperatures at those positions during material deposition. As a result, the whole thermal history of the instrumented locations during the deposition process, including the cooling period after the deposition, was recorded.

Table 2.1. Process conditions monitored

| Sample # | Laser power(w) | Traveling speed(mm/min) | Powder feed rate(g/min) |
|---|---|---|---|
| 1 | 600 | 300 | 8 |
| 2 | 600 | 375 | 10 |
| 3 | 600 | 450 | 12 |
| 4 | 750 | 300 | 10 |
| 5 | 750 | 375 | 12 |
| 6 | 750 | 450 | 8 |
| 7 | 900 | 300 | 12 |
| 8 | 900 | 375 | 8 |
| 9 | 900 | 450 | 10 |

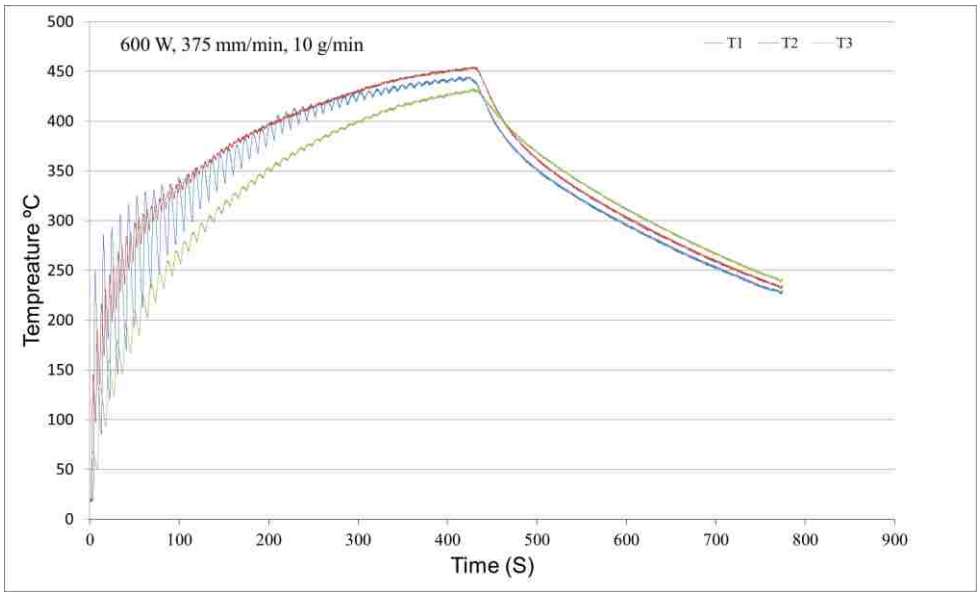


Figure 2.1. Thermal history at the underneath of the first deposited layer, while additional 87 deposited layers arrive in sequence

The substrate material and the deposition powder was 316 L stainless steel, a common commercial alloy. The substrate measured 50×50×12.7 mm (length×width×height). The chemical composition range of 316 L stainless steel is listed in Table 2.2. The offset between the laser head and deposition point was a constant 5mm.

Table 2.2. The Chemical Composition Range of 316L Stainless Steel

| Element | C | Mn | P | S | Si | Ni | Cr | Mo | Fe |
|---|---|---|---|---|---|---|---|---|---|
| (W %) | < 0.03 | < 2 | < 0.045 | < 0.03 | < 1 | 10 - 14 | 16 - 18.5 | 2 - 3 | Bal. |

Hardness tests were performed using a Vickers indenter and a 1-kg load. The substrate's original hardness was tested and an average hardness of 215 VHN was determined. Hardness was also evaluated after deposition as a function of depth as measured from the original substrate surface. The full height of the deposit was covered and tests were also carried out to below the heat affected zone.

# 3. RESULT AND ANALYSIS

## 3.1. THERMOCOUPLES MEASUREMENT

It is important to control the thermal behavior to reproducibly fabricate parts. In order to record the thermal gradient of the laser track as well as the reheating process due to the subsequent layers and correlate the evolution of unique microstructural features in multilayer builds, a new scheme has been designed for locating thermocouples on the substrate. Regarding the thermal histories within the deposited material during deposition, Fig. 3.1 shows the temperature variation of the underneath surface of the first deposited layer at right end (T1), middle (T2) and left end (T3) of deposited wall with different depths (1, 2, and 3 mm, respectively), which directly impinges on the substrate, while the subsequent 87 layers were deposited with a parallel track deposition.

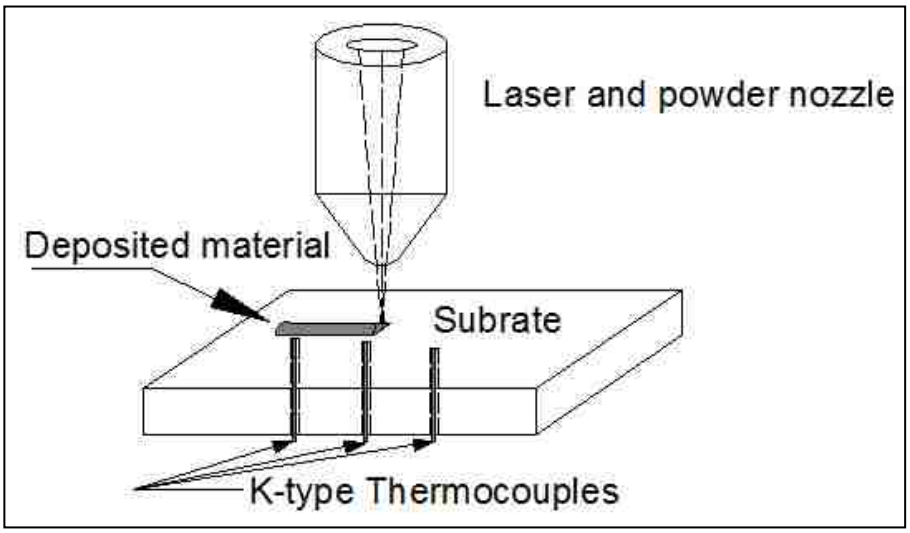


Figure 3.1. Scheme for locating thermocouples on the substrate

Oscillations are the most obvious characteristic of the temperature measurements. Each temperature peak represented the thermocouple's response as the maximum in the temperature field reached it. The temperature increased when more and more energy was transferred to this position by heat conduction. The thermal excursion decayed when

either the energy source moved away from thermocouple position during the deposition of a layer or when subsequent layers were deposited. The thermocouples were attached on the substrate, so the measured temperatures were much lower than those near the molten pool.

**3.2. MICROSTRUCTURE**

Microstructure plays a very crucial role in determining the properties of a component. In the present study, optical and scanning electron micrographs of the top surface and crosssection of laser assisted fabricated layer were observed in detail to study the morphology and secondary dendrite arm spacing, as well as how these were effected by the laser parameters.

The SEM micrographs of different positions of the laser deposition zone prepared with a nominal power of 600 W, laser travel speed of 300 mm/min and beam diameter of 5 mm are displayed in Fig. 3.2. Whenever the power of the laser increases, the dendrite structures of the deposited transitions from thin to coarse gradually, which means that the primary dendritic spacing augments, while the dendrite grows.

As the laser travel speed increases, the microstructural characteristic of the deposited layer changes from coarse dendrites to fine dendrites, which is attributed to a decrease of the ratio of the temperature gradient to the solidification rate. According to the literature [7], the ratio of the temperature gradient to the solidification rate can be estimated according to the following equation:

$$G/R = 2\lambda K(T - T_0)^2 / \eta P v COS\theta \qquad (2)$$

where G is the temperature gradient, R is the solidification rate, v is the laser traveling speed, T is the temperature of the liquid, $T_0$ is the preheated temperature of the substrate, $\eta$ is the laser absorption coefficient, P is the laser power and K is the thermal conductivity of the material.

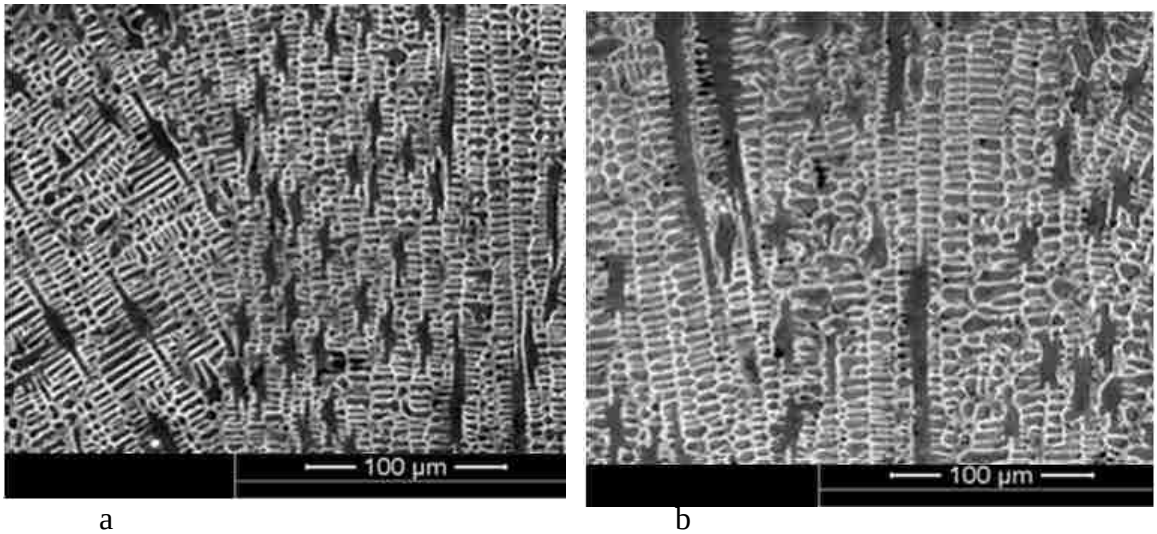


Figure 3.2. Microstructure at 600 W, 300 min of different positions of the laser deposition zone: a top layers, b bottom layers

A homogenous and defect free stainless steel 316 L deposited microstructure has been obtained and the microstructure of deposited material has been shown to be highly dependent on laser deposition process parameters. Figure 3.3 shows a cross-section view of the homogenous cellular appearance of the microstructure of DLD of stainless steel 316 L using the conditions defined in the caption. The deposition is crack free and the microstructure is mostly cellular, with an average secondary dendrite arm spacing varying from 15 to 35 µm. The highest hardness value also correspond to when a homogenous microstructure and small secondary dendrite arm spacing is occurred [8, 9].

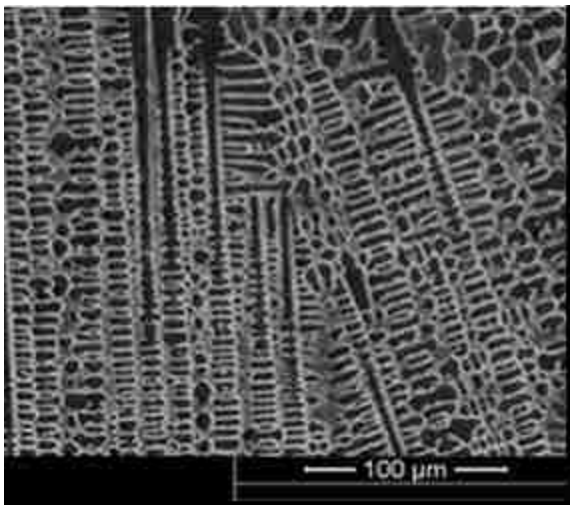


Figure 3.3. Homogenous cellular appearance microstructure of laser deposited stainless steel 316 L600, 450 mm/min

In the process of rapid directional solidification with an ultra-high temperature gradient, it is beneficial to obtain an ultrafine microstructure, resulting in a more uniform distribution of the components, and higher strength. The microstructure that forms in DLD parts is dependent on the cooling rate of each layer from the peak temperature during a certain time of the peak temperature period. The slower cooling rates results from conditions of high incident energy (high power setting and low travel speed); on the other hand, a low laser power and high laser travel speed result in faster cooling rates.

**3.3. HARDNESS ANALYSIS**

The hardness analysis of the deposited specimens showed that the average hardness varied from 185 to 280 HVacross all the samples in this work [10]. Hardness variations were observed in both the deposited and heat affected zone. The level of hardness was affected by the process parameters. Hardness in the deposit was similar to the baseline hardness of the substrate, while the hardness in the heat affected zone was actually higher than the baseline.

The hardness profiles of stainless steel 316 L samples subjected to the investigated laser parameters are illustrated respectively in Fig. 3.4a and b. Hardness measurements were taken at increments of 1,000 µm for the deposited region and 500 µm for the substrate.

The effect of the laser parameters on the hardness of the deposited material and heat affected zone are summarized in Fig. 3.5. It is important to mention that the hardness values reported in Fig. 3.5 are the average values of the hardness measured in the deposited material and heat affected zone. In general, the hardness of the deposited material decreased with increasing laser power and also decreased towards the topmost layers. At constant power, the deposit hardness increased with increased travel speed of the laser beam. At constant travel speed, the hardness decreased with increased laser power. The heat input has a direct relationship with the laser power. The higher power decreases to some limit the cooling rate after solidification. As a consequence of the relatively high cooling rate (that of lower power) the rapid cooling can refine the microstructure, which improve the hardness.

On the other hand, the hardness value of the heat affected zone is greater than that for the deposited material (and the baseline hardness) and decreased towards the topmost layers of the substrate. The hardness of the heat affected zone increased with increased laser power. At constant laser power, the hardness of the heat affected zone decreased with increased travel speed of the laser beam.

The rapid heating and cooling cycles associated with the laser deposition process increased the thermal stress and as a result the dislocation density. The most important factor in determining the secondary dendrite arm spacing and thus the hardness is the cooling rate. Increasing the cooling rate during solidification could produce deposited material with finer grains. Using high laser power leads to an important phenomenon. It lowers the cooling rate and as a result produces coarse dendrites which results in lower hardness.

Published work results showed that the thermal excursions dampen out when the energy source moves away from a substrate during the deposition. Early in the building of the layers, the heat is quickly dissipated away via heat conduction into the substrate. This initial thermal transient leads to a very rapid quenching rate effect at the beginning, resulting in a higher hardness [11].

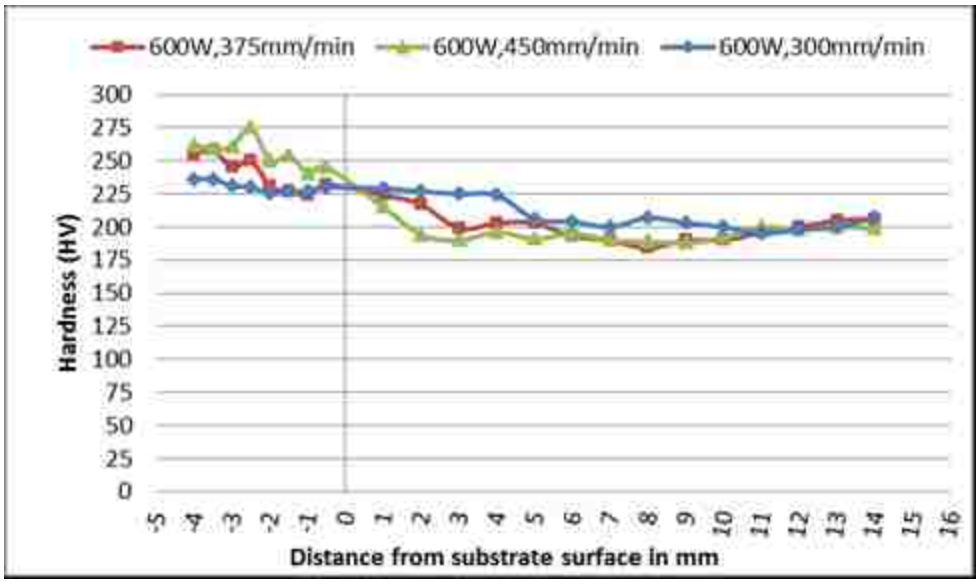


a

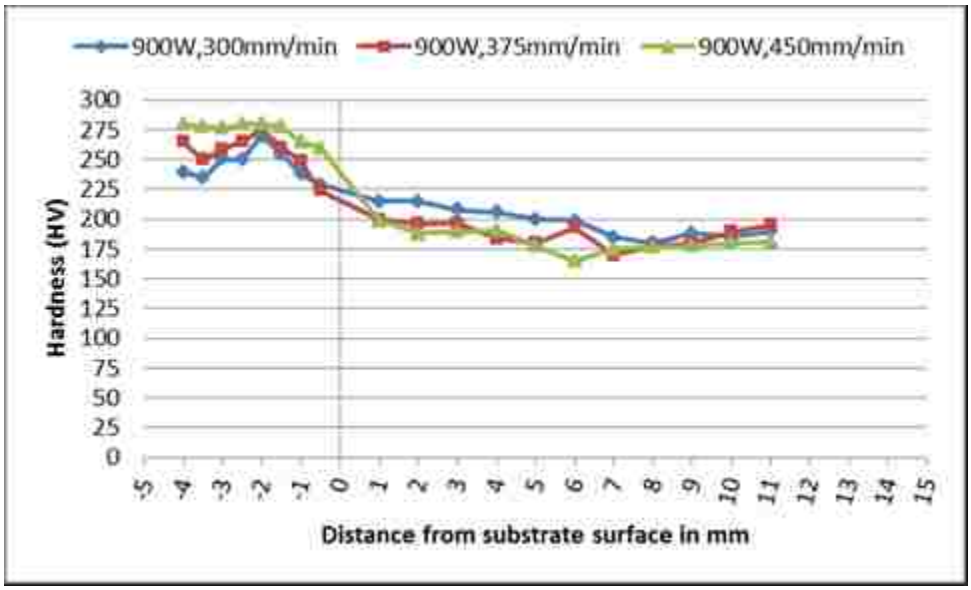


b

Figure 3.4. Hardness Profile at 300, 375 and 450 mm/min: a 600W, b 900 W

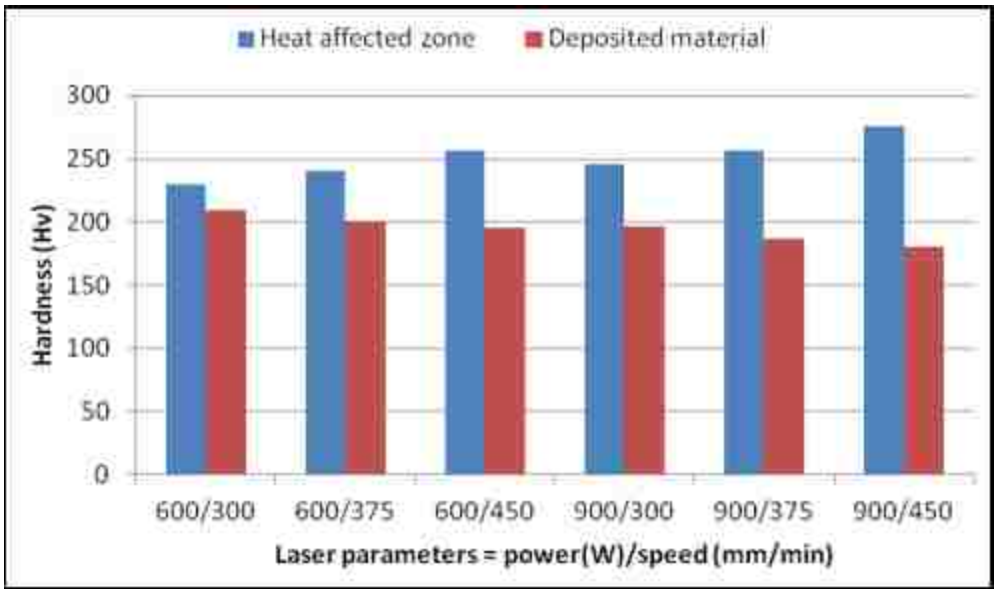


Figure 3.5. The effect of laser parameters on the hardness of deposited material and heat affected zone

In the heat-affected zone, the hardness varied according to the location in which it was measured. The region close to the deposited material had higher hardness values than those far away from the deposited material. An increase in hardness was observed with increased travel speed at constant laser power. This was mainly due to the short time of interaction between the laser beam and the powder, as lower energy was supplied during the melting. The low energy limited time for growth, and hence increased the hardness.

**3.4. SECONDARY DENDRITE ARM SPACING**

In general, the cooling rates experienced by laser-deposited stainless steel 316 L samples decreases with increasing distance from substrate due to the heat increasing and mass build up during deposition. When observed from the side, the surfaces of the components exhibit a layered structure from the laser deposition as well as shows large, elongated grains. These grains were growing epitaxially, inclined in a direction to the layers following the temperature field resulting from the moving laser beam.

The secondary dendrite arm spacing decreases with increasing traverse speed as shown in Fig. 3.6, but was most strongly affected by power level. Thus, secondary dendrite arm spacing also tended to increase with incident energy (=laser power/laser

traverse speed) as seen in Fig. 3.7. The observed trend of increasing secondary dendrite arm spacing with incident energy is as expected because secondary dendrite arm spacing tends to decrease with increasing cooling rate. A high energy results from a combination of high power and low travel speed, yielding a lower cooling rate. Conversely, low energy results from a combination of low power and high travel speed, yielding a higher cooling rate [12].

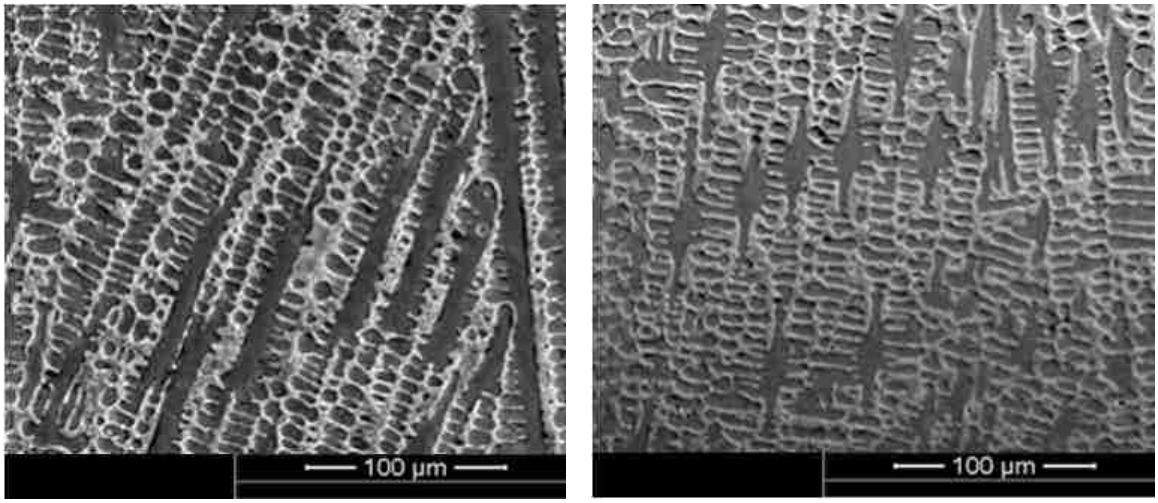


a b

Figure 3.6. Microstructure at 750 W, a 300 mm/min, b 450 mm/min

The secondary dendrite arm spacing was measured and is shown in Fig. 3.8a, b and c. The relationship between the hardness of the 316 L stainless steel and the secondary dendrite arm spacing is plotted in Fig. 3.9. The curve clearly indicates that the hardness of the 316 L stainless steel increases as the secondary dendrite arm spacing decreases. The hardness of the 316 l stainless steel was correlated with the secondary dendrite arm spacing (d) using a straight line (Eq. 3).

$$H = Ad + B \quad (3)$$

where A and B are constants, and H=−1.56d+220.6.

The secondary dendrite arm spacing cell size was determined using Eq. 4

$$d = (d_1 + d_2)/2 \quad (4)$$

where d1 is the length of a secondary arm and d2 is the approximate diameter.

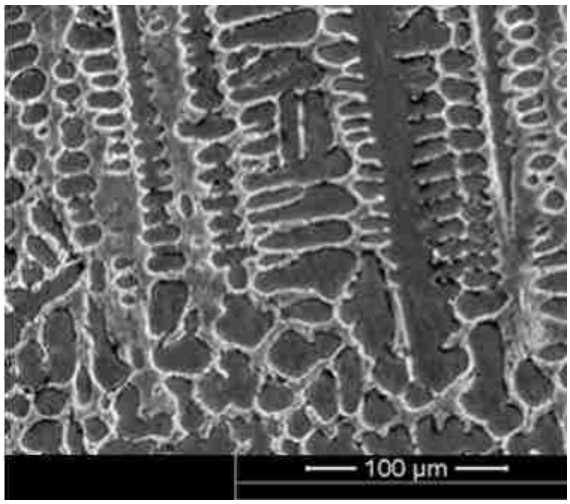


Figure 3.7. Microstructure at 900 W, 300 min/mm

In this work, it was found that the secondary dendrite arm spacing of the 316 L stainless steel decreases as the cooling rate increases. As the cooling rate decreases there is enough time for small dendrite arms to melt and disappear [6]. This occurs as a result of their high surface area to volume ratio that increases their total energy per unit volume. As the small dendrite arms disappear, the secondary dendrite arm spacing of the alloys increases [7].

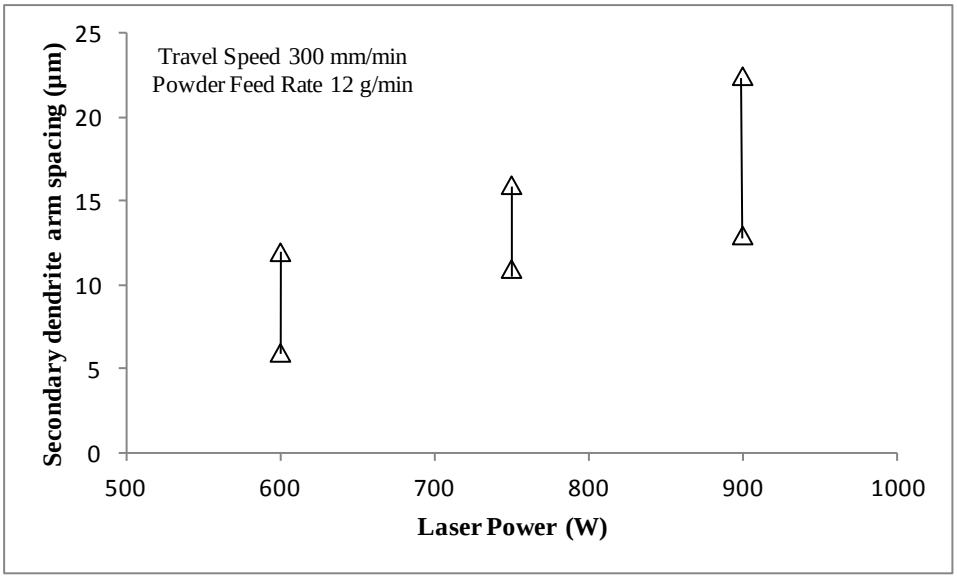


a

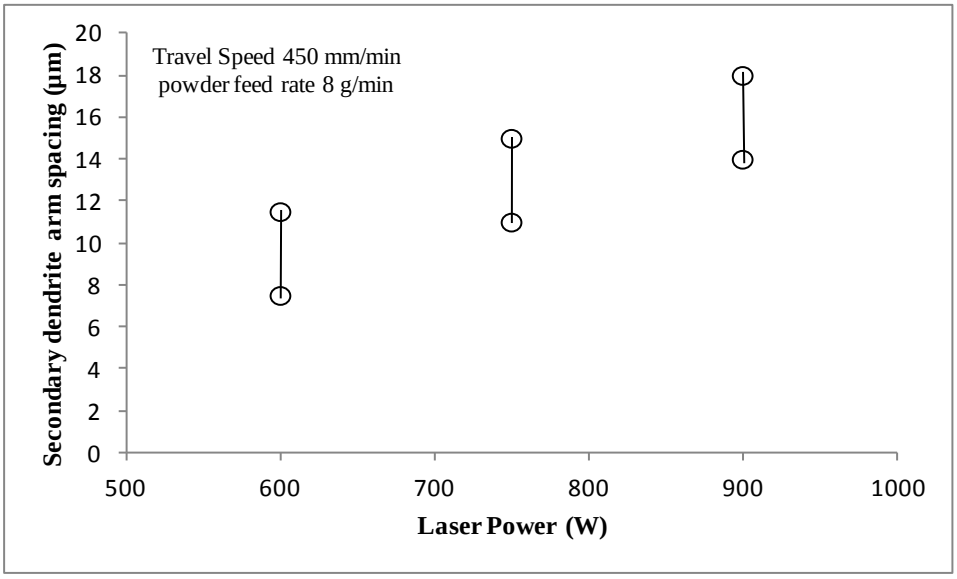


b

Figure 3.8. Range of secondary dendrite arm spacing (d) as function of applied laser power for direct laser deposition of 316 L stainless steel with a travel speed (v) of 300 mm/min, powder feed rate (f) of 12 g/min; b v= 450 mm/min, f=8 g/min; c v= 450 mm/min, f=12 g/min

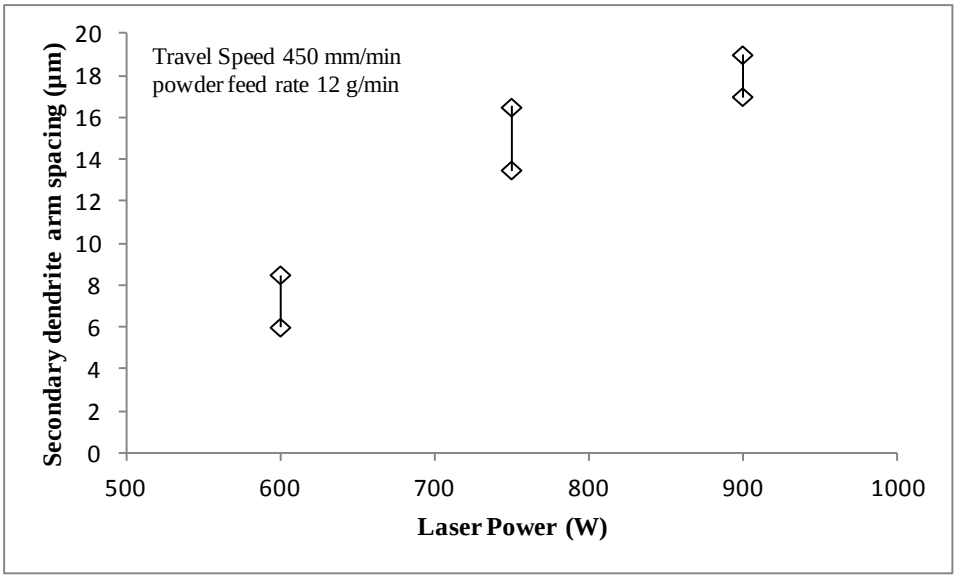


c

Figure 3.8. Range of secondary dendrite arm spacing (d) as function of applied laser power for direct laser deposition of 316 L stainless steel with a travel speed (v) of 300 mm/min, powder feed rate (f) of 12 g/min; b v= 450 mm/min, f=8 g/min; c v= 450 mm/min, f=12 g/min (cont.)

Secondary dendrite arm spacing of the 316 l stainless steel decreases as the cooling rate increases during solidification of laser deposition process. As the secondary dendrite arm spacing decreases, the hardness of the 316 l stainless steel increases.

An ANOVA analysis was employed to investigate the effect the process parameters (laser power, travel speed, and powder feed rate) had on both hardness and secondary dendrite arm spacing. The analysis showed that laser power and travel speed are strongly significant factors, while powder feed rate is not significant at all. Figure 3.10a and b shows the effect of these parameters. A good model was obtained for those two factors for both hardness and secondary dendrite arm spacing. The hardness relation is given above. The relation for secondary dendrite arm spacing is:

$$SDAS(\mu m) = 8.61 + 0.0244\,power(kW) - 0.0311 speed(mm/\min)$$

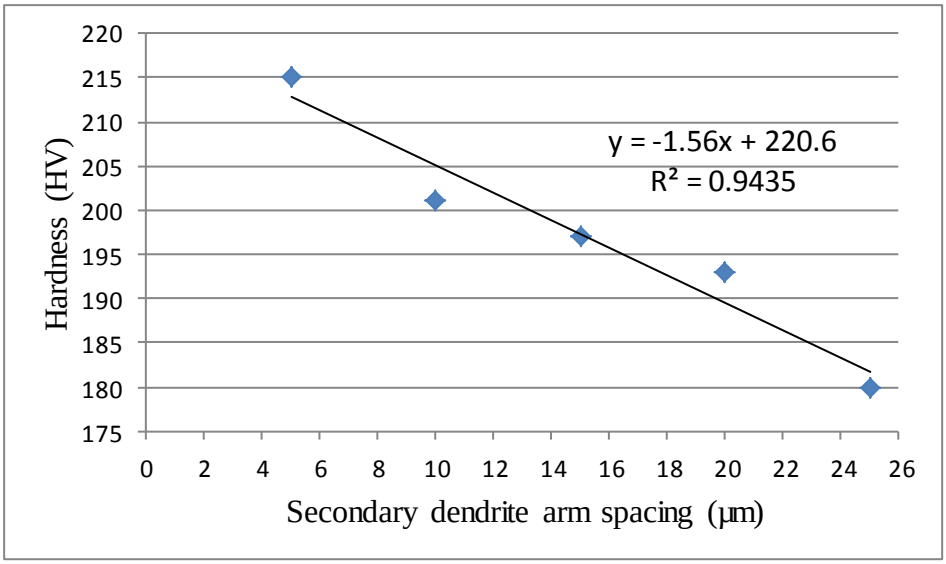


Figure 3.9. Curve showing the effect of secondary dendrite arm spacing (d) on the hardness of the 316 L stainless steel

The fact that the powder feed rate seems to have no effect on the deposit parameters can be explained by two competing factors. As the powder feed rate increases the melt pool temperature decreases, while the volume of the melt pool also increases. Thus, the amount of energy which must be conducted away remains the same.

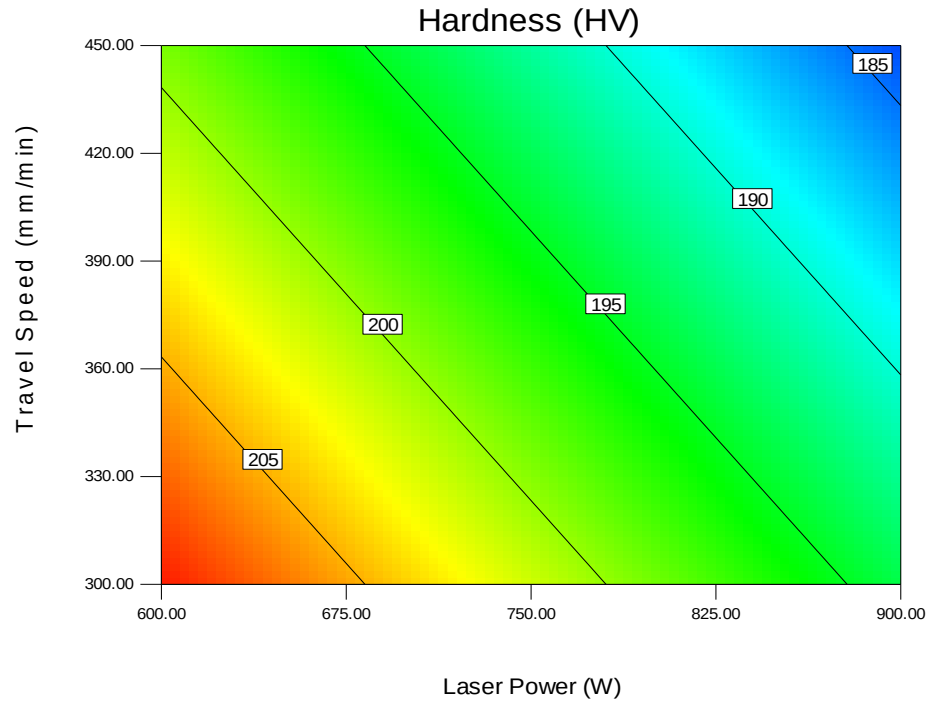


a

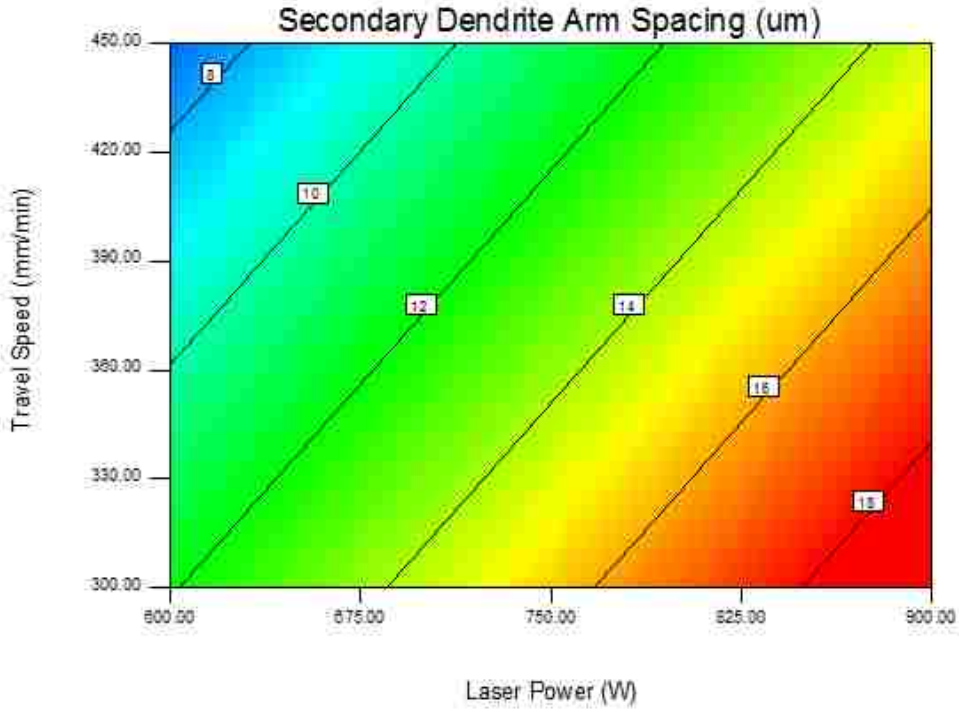


b

Figure 3.10. The effect of laser parameters on a hardness and b secondary dendrite arm spacing

# 4. CONCLUSION

The temperature field evolution, thermal cycling characteristics, temperature gradient and effects of different depositing directions on the thermal process of single-pass, multilayer laser deposition fabrication was investigated. Three process parameters (laser power, travel speed, and powder feed rate) were investigated.

The temperature distribution during the deposition cycle as well as the reheating process due to the subsequent layers was monitored by using thermocouples. The thermal behavior associated with the DLD process involves numerous reheating cycles. As a result, the temperature history of the deposited materials can be considered as a series of discrete pulses.

In general, the travel speed and laser power were shown to significantly affect the microstructure. The deposition was free of cracks, and the microstructure was mostly cellular, with secondary dendrite arm spacing s ranging from approximately 15 to 35 μm. The microstructure that forms in DLD parts is dependent on the cooling rate of each layer from the peak temperature at a certain point in the peak temperature period. The most important factor in determining the secondary dendrite arm spacing and thus the hardness is the cooling rate that associated with the DLD process. Increasing the cooling rate during solidification could produce deposited material with finer grains. The DLD process in the same deposition direction exhibited larger temperature gradients than in the reverse deposition direction, and heat diffusion in the same deposition direction was better.

Hardness distributions across the transverse cross-section of the samples show that as the laser scanning speed increases, the hardness of the deposited material increases. The hardness of the deposited material also decreased with increasing laser power. This is attributed to the finer microstructure. The hardness of the substrate was raised in the heat affected zone and was highest at a depth of around one to three millimeters below the original surface.

## REFERENCES


[1] Kell J, Tyrer JR, Higginson RL, Thomson RC (2005)Microstructural characterization of autogenous laser welds on 316L stainless steel using EBSD and EDS. J Microsc 217:167–173.

[2] Qin Y, Juster NP (2003) Advances in manufacturing technology XVII (1st Edition) p 132.

[3] Zhang K, Zhang X, Liu W (2012) Influences of processing parameters on dilution ratio of laser cladding layer during laser metal deposition shaping. Adv Mater Res 549:785–789.

[4] Wu X, Liang J, Mei J, Mitchell C, Goodwin PS, Voice W (2004) Microstructures of laser-deposited Ti–6Al–4V. Mater Des 25:137–144.

[5] Mahamood RM, Akinlabi ET, Shukla M, Pityana S (2013) Scanning velocity influence on microstructure, microhardness and wear resistance performance of laser deposited Ti6Al4V/TiC composite.Mater Des 50:656–666.

[6] Amine T, Sparks TE, Liou F (2011) A strategy for fabricating complex structures via a hybrid manufacturing process. Solid Freeform Fabrication Symposium, Proceedings of the Twenty Third Annual Solid Freeform Fabrication Symposium, Austin.

[7] Kattamis TZ, Coughlin JC, Flemings MC (1967) Trans Metall Soc TMS-AIME 239:1504.

[8] Dutta Majumdar J, Li L (2009) Studies on direct laser cladding of SiC dispersed AISI 316L stainless steel. Metallurgical and materials transactions. A, Phys Metall Mater Sci 40(12):3001–3008.

[9] Boisselier D, Sankaré S (2012) Influence of powder characteristics in laser direct metal deposition of ss316l for metallic parts manufacturing. Phys Procedia 39:455–463.

[10] Dutta Majumdar J, Pinkerton A, Liu Z, Manna I, Li L (2005) Mechanical and electrochemical properties of multiple-layer diode laser cladding of 316L stainless steel. Appl Surf Sci 247:373–377.

[11] Neela V, De A (2009) Three-dimensional heat transfer analysis of LENSTM process using finite element method. Int J Adv Manuf Technol 45:935–943.

[12] Dutta Majumdar J, Pinkerton A, Liu Z, Manna I, Li L (2005) Microstructure characterisation and process optimization of laser assisted rapid manufacturing of 316L stainless steel. Appl Surf Sci 247:320–327.

# III. MICROSTRUCTURAL AND HARDNESS INVESTIGATION OF TOOL STEEL D2 PROCESSED BY LASER SURFACE MELTING AND ALLOYING

Tarak Amine, Joseph W. Newkirk and Frank Liou

International Journal Advanced Manufacturing Technology
Received: 19 September 2013 /Accepted: 14 April 2014


**ABSTRACT**

Several techniques can be used to improve surface properties of metals. These can involve changes on the surface chemical composition such as alloying or on the surface microstructure, such as hardening. In the present work, melting of the surface by a 9 kW CO2 CW laser of wavelength 10.6 μm was used to alter surface features of D2 tool steel. Carbon powder and nitrogen gas were used as sources of alloying elements during laser processing. The effect of various laser parameters (power and speed) on the microstructure and hardness of D2 tool steel was investigated. Laser powers from 1 to 8 kW and laser speeds from 5 to 15 mm/s were employed. It was found that as the laser power increases, the hardness of the melted zone decreases while that of the heat affected zone increases. On the other hand, the depth of both of melted and heat-affected zones increases with power.

**Keywords:** Laser surface treatment, Laser surface alloying, Material heat treatment.

# 1. INTRODUCTION

A process of laser melting is being developed which includes compositional change in addition to the structural change. Alloying elements in the form of powder, thin foil or wire are pre-placed on the surface of the metal being treated. When the laser is applied, the surface of the alloy melts and the alloying elements can add to the composition resulting in an altered chemical composition after solidification. The composition and dimensions of the newly alloyed layer depend on many factors such as laser beam power density and the processing speed. Due to the change in surface chemical composition which takes a place during melting of the substrate and alloying elements, the process is known as laser surface alloying (LSA).

As the laser beam moves away from the melt zone (MZ) the latter cools quickly as heat is conducted into the bulk material which functions as an efficient heat sink. As a result, the MZ solidifies rapidly via conducting its heat to the layers beneath it. Accordingly, these underlying layers are heated rapidly to temperatures below the melting point of the material and then cooled quickly to the ambient temperature due to conduction to the bulk material [1–5]. Themaximum temperature reached in these layers as well as the rapid heating and cooling rates altering the nature of phases present and as a result the mechanical properties. According to Bourithis [6], the heating and cooling rates associated with laser application can be up to 106 and 104 °C/s, respectively. The layers which are heated to temperatures lower than the melting point of thematerial are called the heat-affected zone (HAZ). The depth and mechanical properties of the HAZ are strongly dependent on the laser parameters used. The base metal (BM) is the zone which has not been affected by the laser application.

Although there are a number of investigators who have studied the effect of laser surface melting on ferrous alloys, little work has been published on the use of carbon powder and nitrogen gas to alter the surface chemical composition of steels. Also, a $CO_2$ laser was used in this study due to the fact that efficiency of the Nd-YAG laser is only 2–3 % of that of $CO_2$ laser. The extremely rapid solidification rate associated with laser surface melting produces phases cannot usually be formed by conventional methods.

A number of D2 tool steel samples were subjected to various laser melting treatments in which several laser parameters (power and traverse speed) were used. Laser surface treatment involves directing a laser beam of a desired size, shape and with the required power at the surface of the material being treated. The absorption of laser energy and the conversion of its energy into thermal energy lead to very rapid surface heating. Melting of the surface will occur when heated to a temperature above its melting point. The layer melted at the surface is usually called the MZ.

Various laser parameters were employed in this study, some of them have exhibited the best combination of depth and hardness of the melted and heat-affected zones, and thus were selected for further study in this work. Microhardness measurements and metallographic inspections were employed to determine the hardness, nature of phases present, grain size, and the geometry (depth and width) of the melted and heat affected zones. In addition, X-ray diffraction technique was used to investigate the effect of laser parameters on the volume fraction of phases present in the melted zone.

# 2. EXPERIMENTAL PROCEDURE

## 2.1. MATERIAL

Cold work tool steels include the high-carbon, high-chromium steels or group D steels. Type D2 steel is the most commonly used steel among the group D steels. The nominal composition of D2 Cold Work Tool steel is 1.40 to 1.60 % of carbon, 11 to 13%of chromium, 1.10%max of vanadium, 0.6%max of both manganese and silicon, and 0.70 to 1.20 % of molybdenum. The alloy investigated in this study was D2 tool steel which was analyzed as having the following chemical composition, Table 2.1.

Table 2.1. Chemical Composition of the Material Used Investigation wt%

| Elements | C% | Si% | Mn% | Cr% | Mo% | V% | Fe% |
|---|---|---|---|---|---|---|---|
| Tool steel D2 | 1.55 | 0.25 | 0.35 | 11.8 | 0.8 | 0.95 | balance |

## 2.2. EXPERIMENTAL DEVICE

The surface treatment was carried out using CO2 laser, operated at powers up to 8 kW and travel speeds up to 15 m/min.

Figure 2.1, shows schematic diagramof the experimental setup. In this study, specimens of 30 mm thickness were fixed on the machine table and irradiated with the laser beam. Samples were divided into two groups. The first group of samples was coated with a carbon powder with an average of particle size of 25–50 μm before being subjected to laser melting. While the second group was shielded by nitrogen gas during laser processing.

A number of experiments were carried out on D2 tool steel including surface melting were performed using CO2 CW laser Gaussian beam with 1 mm of beam diameter at different laser beam energies and travel speed as shown in Table 2.2. The D2 samples were placed at a constant distance, the focus point of 10 mm. The specimen surface, the before laser treatment, were ground using a grinder to reduce the surface reflectivity. The samples were then cleaned with alcohol and dried. During treatment, a

total of three trackswere applied to each specimen with sufficient spacing between each track to prevent interaction.

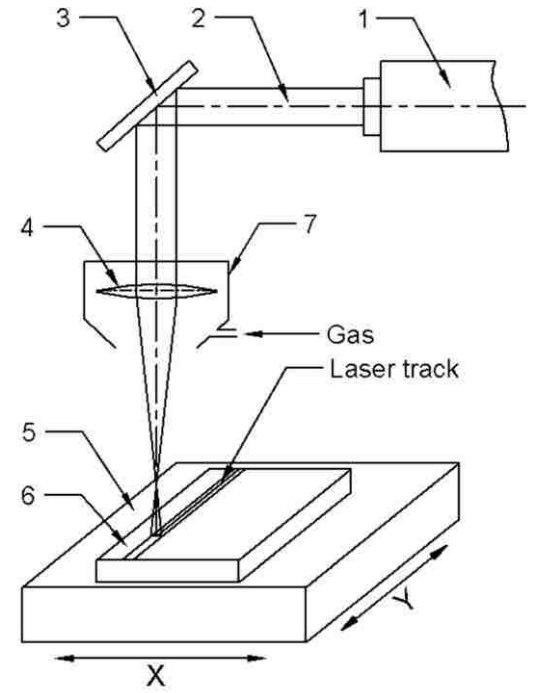


Figure 2.1. Schematic diagram of laser surface heat treatment

Table 2.2. Condition of laser processing parameters

| Specimen no. according to alloying element | | Laser parameters | |
|---|---|---|---|
| C | $N_2$ | Power kW | Speed mm/s |
| 1 | 13 | 1 | 5 |
| 2 | 14 | 1 | 10 |
| 3 | 15 | 2 | 5 |
| 4 | 16 | 2 | 10 |
| 5 | 17 | 3 | 5 |
| 6 | 18 | 3 | 10 |
| 7 | 19 | 6 | 10 |
| 8 | 20 | 6 | 15 |
| 9 | 21 | 7 | 10 |
| 10 | 22 | 7 | 15 |
| 11 | 23 | 8 | 10 |
| 12 | 24 | 8 | 15 |

Surface alloying of tool steel with carbon was carried out by pre-coating the specimen surface with graphite mixed with an acetone–resin solution. The coated thickness of the carbon powder mixture was about 50–100 μm. Argon gas was used as a shield gas. Surface alloying of tool steel with nitrogen gas was achieved by using nitrogen gas as shielded gas to flow. The nitrogen gas flow rate was maintained at 1,500 L/h.

After the laser treatment, transverse sections were cut from each treated zone using a saw with a jet of coolant liquid. This was to prevent any change in the microstructure. Standard methods of sample preparation for metallographic inspections were followed. To prevent the rounding off of edges of the small samples during grinding, a special fixture made of hard steel was manufacture and the fixture and sample were cold mounted together.

# 3. RESULT AND DISCUSSION

## 3.1. RESULTS

The D2 tool steel was supplied in the annealed condition which was heated to 850 °C followed by cooling at 10 °C/h to 650 °C and finally air cooled. It can be seen that the microstructure of the starting material consisted of coarse carbides (white phase) of different shapes and sizes embedded in a pearlitic matrix as shown in Fig. 3.1.

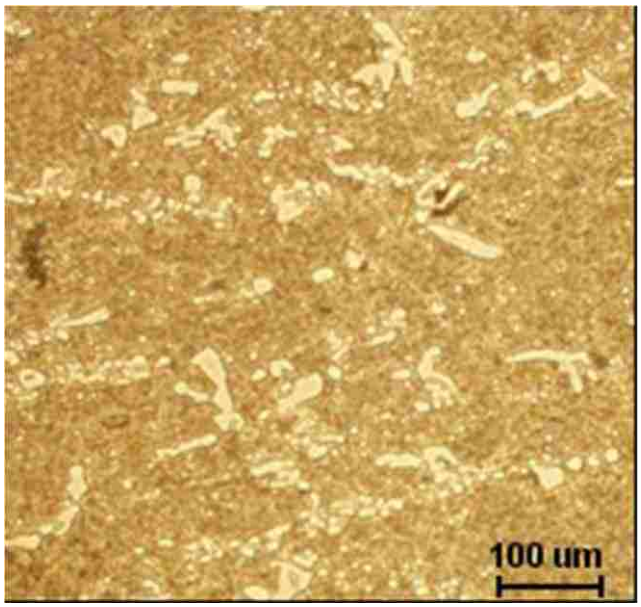


Figure 3.1. Microstructure of the as Received D2

The microstructure of the MZ in all laser melted samples consists of austenite cells surrounded by segregated carbides; such a structure is known as ledeburite. The rapidly solidified microstructure is refined. The grain size measurements show that the austenite grain size increased with increasing laser power, Fig. 3.2. When the laser power was kept constant, the grain size of austenite decreased as the laser speed was increased, Fig. 3.3. The influence of the laser parameters on the grain size of austenite in the MZ is shown in Table 3.1.

Themicrostructures of the HAZ in samples subjected to the applied laser parameters consisted of coarse carbides embedded in a matrix of martensite and retained austenite. At different distances from the MZ, the material in the HAZ was austenitized at differing temperatures and as a result, the hardness at any given distance from the MZ was strongly dependent on the laser parameters used. For the purpose of this investigation, the HAZ is defined as the depth beneath the melted zone with hardness greater than 5 % of that of the base metal, which had a average hardness of 300 HV. The BM is the zone which has not been affected by the laser application.

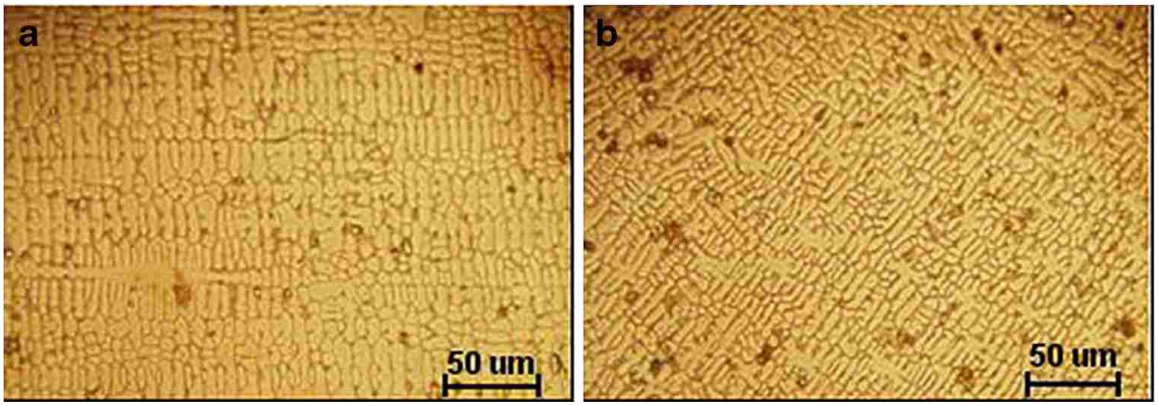


Figure 3.2. Microstructure of the laser melted zone at travel speed 15mm/s, at different energy level: a 7 kw, b 6 kw

Microhardness measurements were made on a cross section of heat-treated area and were taken at different increment. The increment was 50 μm for low laser powers (1, 2, and 3 kW) samples. The increment was 125 μm for high laser powers (6, 7, and 8 kW) samples because of larger heat-treated area which was produced in those samples. The hardness values presented in Table 3.2 are the average of three readings taken along a center line from the surface of the sample towards the center at the same depth from the surface, Fig. 3.4.

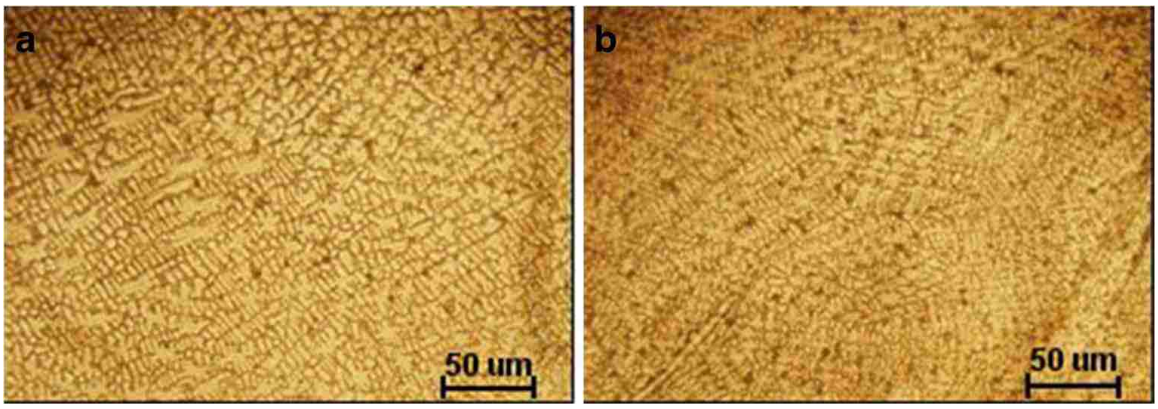


Figure 3.3. Microstructure of the laser melted zone at energy level 3 kW, at different travel speed: a 5 mm/s, b 10 mm/s

Table 3.1. The influence of laser parameters (power and travel speed) on grain size

| Laser parameters (power kW, travel speed mm/s) | Grain size (μms) |
|---|---|
| 1,5 | 2.50 |
| 1,10 | 2.10 |
| 2,5 | 2.97 |
| 2,10 | 2.56 |
| 3,5 | 3.86 |
| 3,10 | 3.68 |
| 6,10 | 5.00 |
| 6,15 | 4.81 |
| 7,10 | 6.82 |
| 7,15 | 6.61 |
| 8,10 | 7.12 |
| 8,15 | 6.98 |

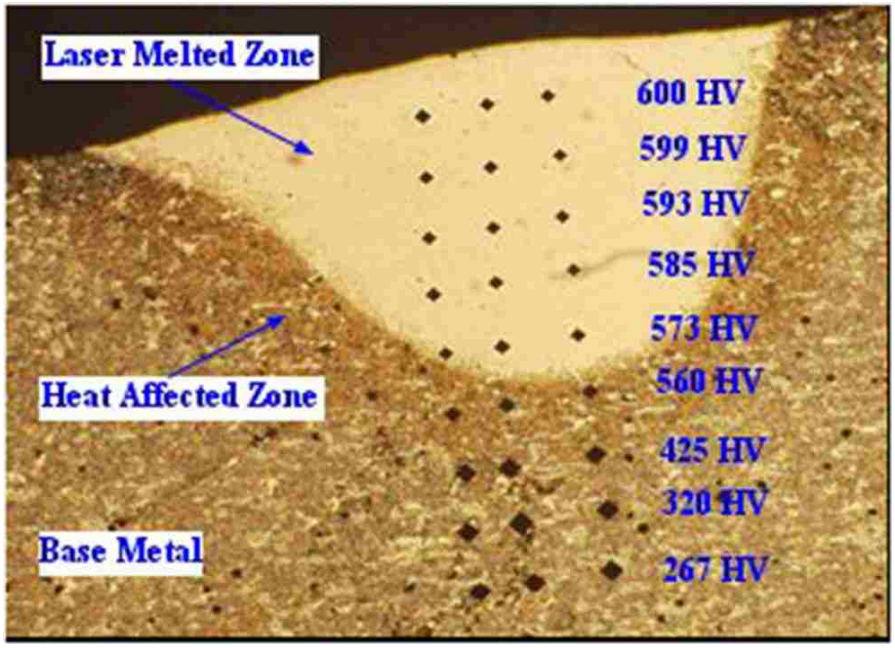


Figure 3.4. Microhardness indentation of sample with carbon alloying processed at (3 kW, 10 mm/s)

Table 3.2. The effect of laser parameters on the hardness of mz, haz zones

| Alloying Elements / Laser Parameters | | Carbon | | Nitrogen | |
|---|---|---|---|---|---|
| Power (kW) | Speed (mm/s) | Average of hardness of MZ (HV) | Average of hardness of HAZ (HV) | Average of hardness of MZ (HV) | Average of hardness of HAZ (HV) |
| 1 | 5 | 745 | 415 | 605 | 405 |
| 1 | 10 | 695 | 345 | 590 | 400 |
| 2 | 5 | 615 | 430 | 580 | 420 |
| 2 | 10 | 585 | 345 | 585 | 420 |
| 3 | 5 | 580 | 480 | 570 | 535 |
| 3 | 10 | 585 | 450 | 565 | 530 |
| 6 | 10 | 590 | 480 | 535 | 445 |
| 6 | 15 | 560 | 465 | 500 | 440 |
| 7 | 10 | 535 | 490 | 490 | 460 |
| 7 | 15 | 520 | 480 | 470 | 450 |
| 8 | 10 | 510 | 540 | 465 | 470 |
| 8 | 15 | 500 | 525 | 460 | 455 |

In general, the average of hardness of the MZ decreased linearly with the increase in power for a constant traverse speed of 10 mm/s as shown in Fig. 3.5.

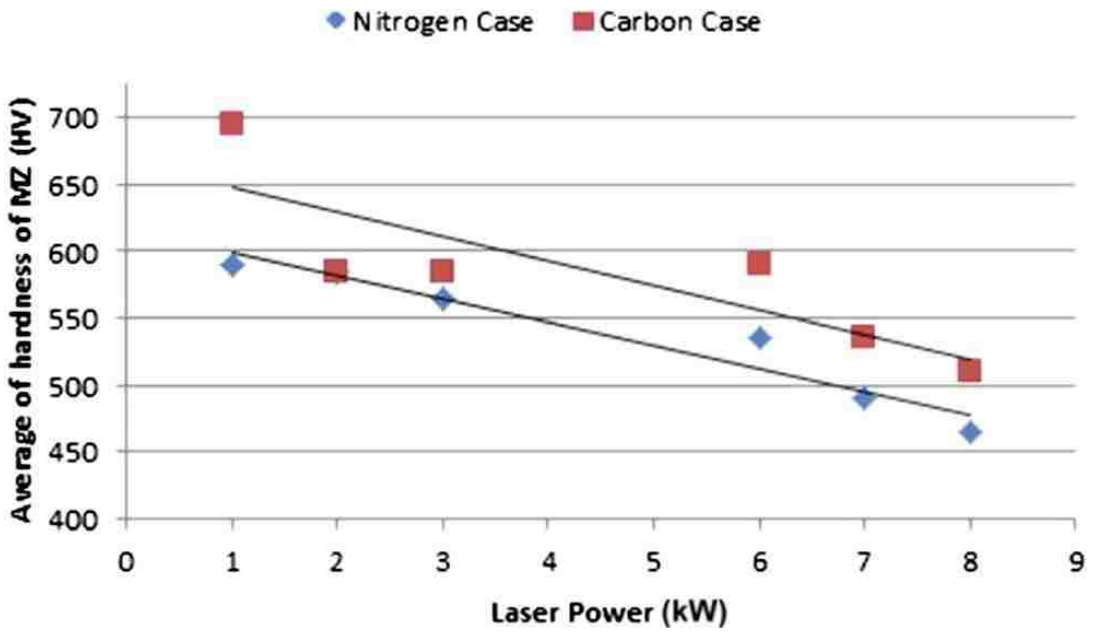


Figure 3.5. Average of hardness of the mz with change in power at a constant traverse speed 10 mm/s

Metallographic inspections and microhardness measurements were used to determine the depth and width of melted and heat-affected zones. Results showed that laser parameters used have a pronounced effect on the geometry (depth and width) of the generated hardened zones, i.e., MZ and HAZ. Figures 3.6 and 3.7 demonstrate the effect of laser parameters on the depth and width of melted and heat-affected zones, while Table 3.3 summarizes these results. However, the following observations were noted:

- In general, the depth of theMZ increased linearly with the increase in power from 1 to 7 kW for a constant traverse speed of 10 mm/s as shown in Fig. 3.8, however, when the power was further increased to 8 Kw the depth of MZ has surprisingly decreased. This was more pronounced in samples laser treated with nitrogen.

- The width of MZ and HAZ increased as the laser power was increased, this was more obvious in samples alloyed with carbon comparing to those alloyed with nitrogen.
- When the laser power was kept constant, the depth and width of MZ and HAZ decreased as the speed of the laser beam was increased.

Table 3.3. The effect of laser parameters on MZ, HAZ depth and width

| Alloying Elements / Laser Parameters | | Carbon | | | Nitrogen | | |
|---|---|---|---|---|---|---|---|
| Power (kW) | Speed (mm/s) | Depth of MZ (μm) | Thickness of HAZ (μm) | Melted width (μm) | Depth of MZ (μm) | Thickness of HAZ (μm) | Melted width (μm) |
| 1 | 5 | 685 | 200 | 995 | 645 | 185 | 950 |
| 1 | 10 | 605 | 190 | 970 | 555 | 175 | 850 |
| 2 | 5 | 1205 | 295 | 2005 | 1100 | 265 | 1850 |
| 2 | 10 | 1115 | 270 | 1700 | 950 | 225 | 1530 |
| 3 | 5 | 2015 | 565 | 2765 | 1930 | 455 | 2625 |
| 3 | 10 | 1665 | 500 | 2145 | 1425 | 345 | 2230 |
| 6 | 10 | 2225 | 595 | 2965 | 2100 | 550 | 2885 |
| 6 | 15 | 2200 | 545 | 2900 | 2010 | 460 | 2710 |
| 7 | 10 | 2295 | 615 | 3335 | 2150 | 590 | 3250 |
| 7 | 15 | 2100 | 595 | 3015 | 2050 | 560 | 2995 |
| 8 | 10 | 2195 | 600 | 3550 | 1950 | 555 | 3450 |
| 8 | 15 | 2045 | 585 | 3485 | 1900 | 505 | 3345 |

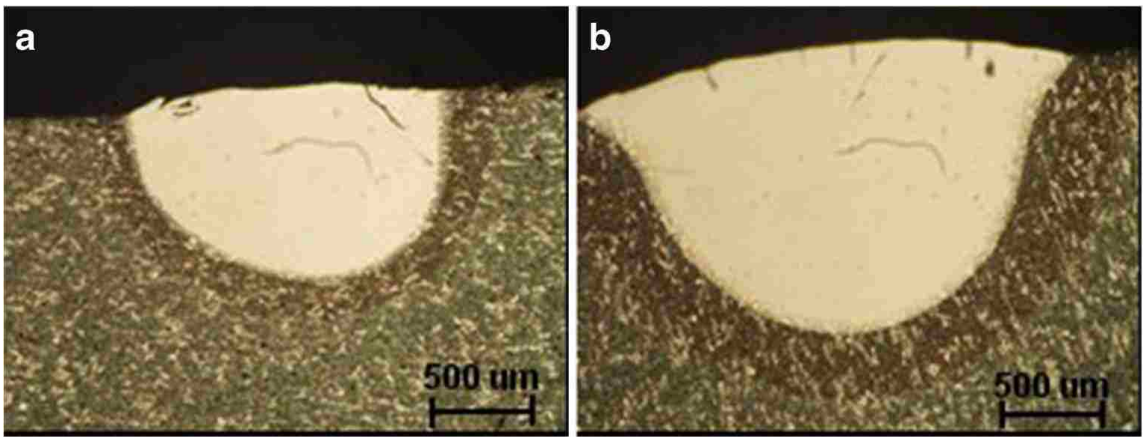


Figure 3.6. The width and the depth of the laser melted zone with nitrogen alloying at travel speed 10 mm/s, at different energy level: a 2 kW, b 3 Kw

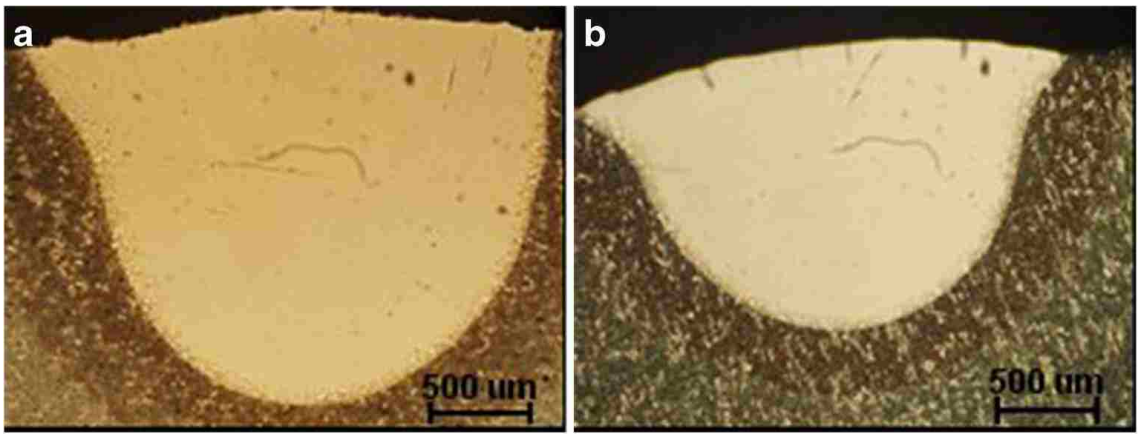


Figure 3.7. The width dimension samples with nitrogen alloying at energy level 3 kW, at different travel speed: a 5mm/s, b 10mm/s

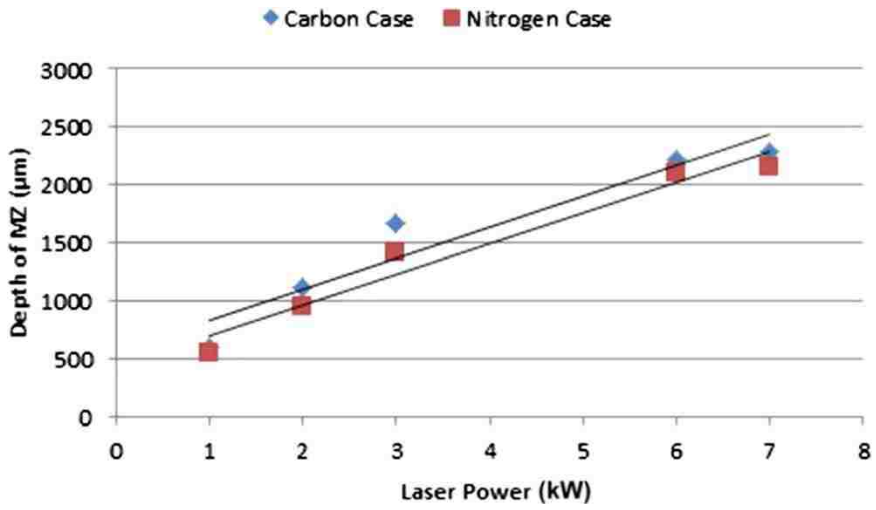


Figure 3.8. Variation of depth of MZ with change in power at a constant traverse speed 10 mm/s

X-ray diffraction techniques showed that at a constant speed, as the laser power was increased the volume fraction of the austenite increased and that of carbides decreased. It was also noted the presence of iron nitrides (Fe24 N10) when the nitrogen gas was used for shielding. X-ray diffraction results are shown in Figs. 3.9 and 3.10.

The effects of the laser parameters on the hardness of melted and heat-affected zones indicate the following:

- The hardness of the MZ decreased with increasing laser power. On the other hand, the hardness of the HAZ increased with power.
- At a constant laser power, the hardness of MZ and HAZ decreased with increasing the traverse speed of the laser beam.
- At constant laser parameters, the hardness of MZ and HAZ in samples coated with carbon powder for shielding were higher than the corresponding hardness of samples in which nitrogen gas was used for shielding.

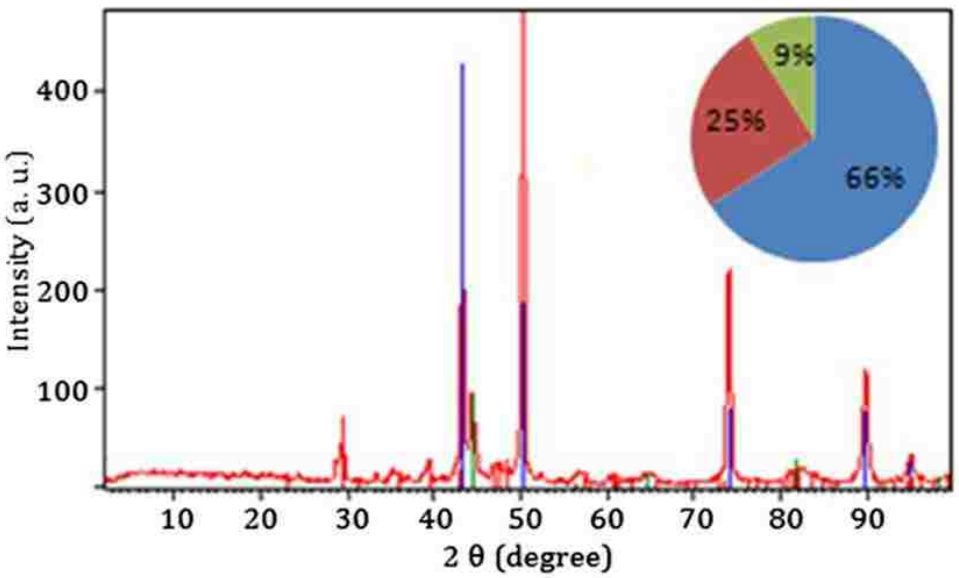


| Compound Name | Chemical Formula | Semi Quant [%] | Index Name |
|---|---|---|---|
| Austenite | C Fe15.1 | 66 | Iron Carbon |
| Carbides | (CrFe)23C6 | 25 | Carbides |
| Chromium Iron Vanadium | V Cr Fe8 | 9 | Chromium Iron Vanadium |

Figure 3.9. X-ray diffraction pattern taken from the surface of MZ sample with carbon alloying at 8 kWand 10 mm/s

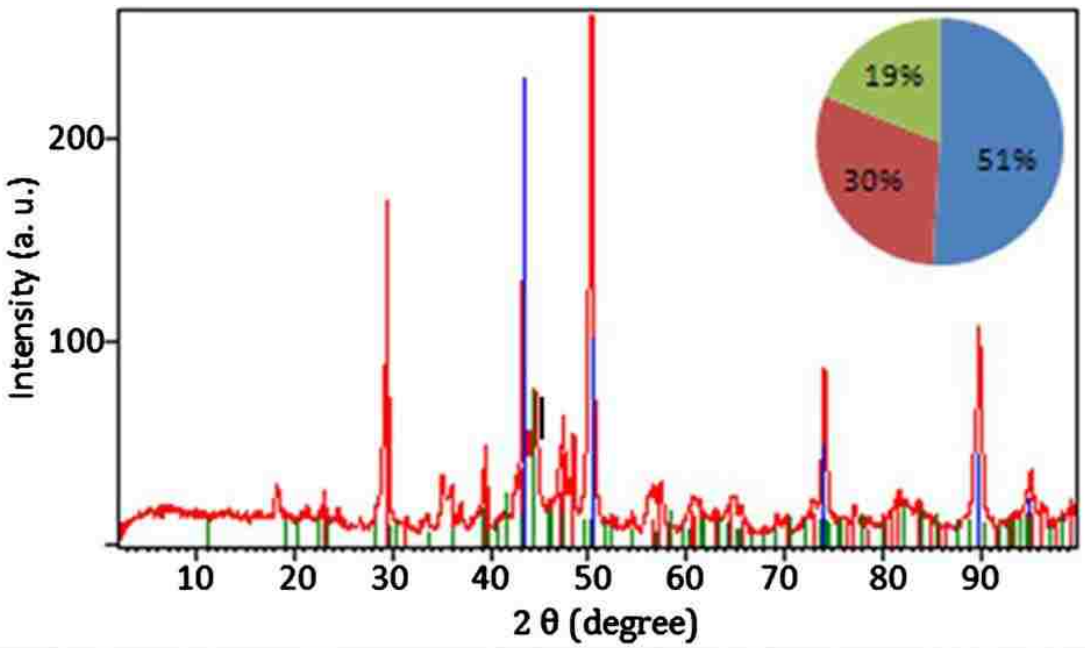


| Compound Name | Chemical Formula | Semi Quant [%] | Index Name |
|---|---|---|---|
| Carbides | $(CrFe)_{23}C_6$ | 51 | Carbides |
| Austenite | $C\ Fe_{15.1}$ | 30 | Iron Carbon |
| Nitride | $Fe_{24}\ N_{10}$ | 19 | Iron Nitride |

Figure 3.10. X-ray diffraction pattern taken from the surface of MZ sample with nitrogen alloying at 7 kWand 10 mm/s

### 3.2. DISCUSSION

The microstructure of D2 tool steel in the annealed condition consisted of carbides embedded in a pearlitic matrix. These carbides have a chemical formula of $(Fe+X)_{23}C_6$. These hard carbides are usually called K1 type carbides, the hardness of which can be up to 73 HRC. The microstructure of the MZ of all samples subjected to the different laser parameters consisted of austenite cells surrounded by segregated carbides. In fact, neither martensite nor any other phase was found in the microstructure of the melted zone of laser-treated samples. This is due to the effect of the alloying elements, particularly carbon and chromium, on the MS temperature. The influence of the former on the MS is shown in Fig. 3.11. It can be noted from this figure that as the percent of the carbon dissolved in austenite increases the $M_S$ and $M_f$ fall rapidly.

Furthermore, the combined effect of C and Cr and other alloying elements on the MS temperature is given by [7]:

MS (°F)=1,000 – (650 x %C) – (70 x %Mn) – (35 x Ni) – (70 x %Cr) – (50 x Mo)(1)

Thus, if only 0.7 % C and 8 % Cr have dissolved in the molten metal during laser melting and remained in the austenite as a result of the high cooling rate associated with the laser process, the MS temperature would be (−66 °C). This value of MS is enough to render a thermally stable austenite at room temperature.

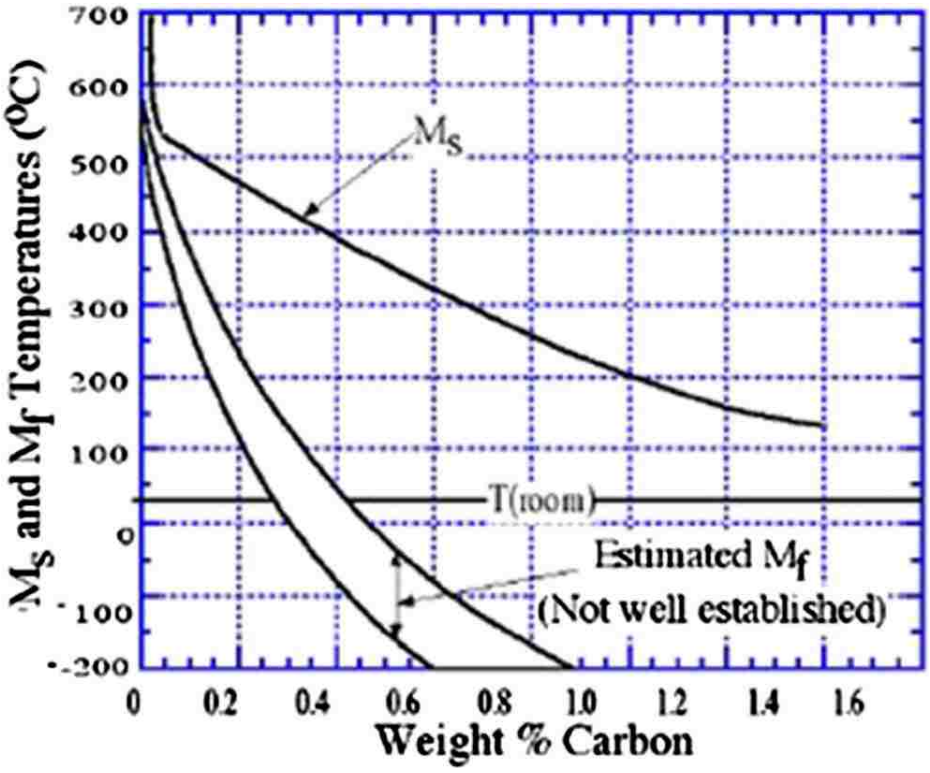


Figure 3.11. The MS and Mf temperatures both fall rapidly as%C in austenite increases

Metallographic inspections showed that the grain size of austenite cells increased as the power of the laser beam was increased. On the other hand, quantitative X-ray diffraction analysis showed that increasing laser power resulted in an increase in the

volume fraction of austenite phase and a decrease in the volume fraction of the segregated carbides.

In fact, it cannot be claimed that the laser parameters employed in this work have resulted in complete dissolution of carbides in the molten metal during laser treatments. This may explain the increase of the grain size of austenite and its volume fraction at expense of the volume fraction of carbides with increasing laser power. In other words, it was assumed that lower laser powers led to partly dissolving of carbides during melting. This is due to the short laser processing time. Although, the laser power densities used in this work were enough to raise the temperature of the surface to a temperature above the melting point of the alloy, however, a certain period of time is required to completely dissolve the massive coarse carbides present in the matrix [7]. In low laser powers, when the molten metal started to solidify as a result of eliminating the heating source, the partly dissolved carbides prevented the growth of austenite grains [8, 9].

When the laser power was increased, much more heat was given to the material. Consequently, much more time was needed for the alloy to lose the heat given. This has delayed solidification for longer times. As a result, more time was given to carbides to proceed in dissolving which has led finally in a great reduction in the volume fraction of carbides as the laser power were further increased. Thus it can be concluded that the elimination of carbides enhanced austenite grains ability to grow during solidification when high powers were employed. X-ray diffraction results support this hypothesis. The volume fraction austenite and carbides at a laser power of 7 kW were 30 and 51 %, respectively, Fig. 3.10. Raising the laser power to 8 kWand keeping the laser speed constant, altered the former volume fractions to 60 and 25 % respectively, Fig. 3.9.

The effect of laser parameters on the microstructure of the heat-affected zone was obtained for various laser parameters. As was mentioned in “Results” section, the microstructure of the HAZ generally consisted of martensite and retained austenite. These layers have been heated to different austenitsing temperatures. Layers in the HAZ located close to the boundary between the MZ and HAZ were austenitized at high temperatures.

The austenizing temperature falls as a function of depth in the HAZ. As the diffusion of carbon and other alloying elements in austenite is strongly dependent on the austenitizing temperature ($T\gamma$) and austenitizing time ($t\gamma$), different layers in the HAZ

were saturated with different fractions of carbon [10]. Due to the high quenching rate associated with the laser application, martensite and retained austenite of different carbon content and volume fractions were obtained in the HAZ. The closer the location to the boundary between the MZ and HAZ, the higher is the volume fraction of retained austenite and the carbon content of martensite.

The influence of laser parameters on the depth and width of MZ and HAZ, as mentioned earlier, the depth of the melted and the heat-affected zones increased as laser power was increased from 1W to 7 kW. Further increase in the power to 8 kW caused a remarkable reduction in the depth of both layers. This was true in all samples either coated with carbon powder or laser treated in the presence of nitrogen gas. In fact, the reduction in the depth of these zones was more pronounced in the later case.

This increase in the depth of both layers, with increasing power from 1 to 7 kW, is due to the increase of the input heat. On the other hand, the reduction in the depth of the melted zone can be attributed to vaporization. Higher laser densities can raise the surface temperature to the vaporization point. Two vaporization mechanisms may take place, namely surface or volumetric vaporization. The latter mechanism, results in a more rapid rate of material removal than the former [11, 12].

The laser surface melting process is followed by rapid selfquenching, leading to a high cooling rate of up to 106 °C/s [13, 14]. Thus, the cooling rate is the most important factor in determining the grain size and thus the hardness, as the, higher cooling rate during solidification would produce material with finer grains. As it has been mentioned before, using high laser power leads to two important phenomena. Firstly, it lowers the cooling rate and as a result austenite with coarse grains formed. Secondly, it lowers the volume fraction of carbides [15].

In fact, there are many mechanisms for strengthening (hardening) of materials [10, 16, 17]. Two of them are the grain refinement hardening and dispersion hardening. The first means decreasing the grain size of the matrix while the second means increasing the number of particles embedded in this matrix. Actually, as the grain boundaries and the number of small separate particles in a microstructure increase, they both impede the movement of dislocations which causes a hardness increase. Thus, it can be claimed that

softening of materials occurs as grain size of the matrix increases and the volume fraction of particles embedded in it decreases.

In this study, it was noted that when higher laser powers were used, the cooling rate was lowered causing austenite with large grains. Furthermore, the carbide volume fraction was decreased. This implies that dislocations were able to move easily in the resultant structures by using high powers, and this can explain the observed reduction in hardness.

The reduction of hardness observed with increasing the traverse speed at constant laser powers is due to the reduction in the amount of heat given to the material. However, the relative higher hardness values exhibited by samples coated with carbon comparing to the corresponding samples laser treated in the presence of nitrogen gas can be attributed to the increase of the carbon content of the melted zone as a result of dissolving the carbon powder in the molten metal; in general, increasing carbon content increases the hardness.

In the HAZ, the hardness was varied according to the location in which it was measured. Layers close to the MZ exhibited higher hardness values than those far away from the MZ. This is due to the difference in austenitising temperatures (Tγ). As Tγ increases more carbon and alloying elements dissolve in austenite. This is due to faster diffusion of carbon and alloying elements at higher temperatures. Austenite with higher carbon content yields harder martensite when rapidly quenched to room temperature. However, increasing carbon content increases the volume fraction of retained austenite.

As we go far from the boundary between the MZ and HAZ towards the base metal, the austenitzing temperature decreases. As a result, the present of carbon and alloying elements dissolved in austenite as well as the diffusivity of these elements in austenite decreases. Consequently, martensite with lower hardness values and a lower volume content of retained austenite is obtained. This explains the gradual decrease in the hardness of the hardness of the HAZ as distance from the samples surface increase. The reduction of hardness observed with increasing the traverse speed at constant laser powers is due to the reduction in the amount of heat given to the material.

# 4. CONCLUSIONS

- Laser surface melting of D2 tool steel can be used to melt 2,150 μm it nitrogen is used as a shielded gas and 2,225 μm it carbon is used as a coating powder. In both cases the melted zones were free of crakes.
- The width of the melted zone is strongly dependent on the laser power.
- Laser surface melting of D2 tool steel in presence of nitrogen resulted in the formation of some nitrides which generally improve the corrosion resistance of the alloy.
- Coating the D2 tool steel samples with carbon powder in laser melting produces deeper hardness layers than in samples treated with shielded nitrogen gas. This due to the reduction in the reflectivity of the laser beam.
- In general, low powers produce higher hardness melted zones than higher powers due to the partially dissolving of hard carbides.
- Laser surface melting of D2 tool steel in presence of nitrogen resulted in the formation of some nitrides which may improve the corrosion resistance of the alloy.

## REFERENCES


[1] Draper CW (1982) Laser surface alloying: the state of the art. J Metals 34:24–32

[2] Tiziani A, Giordano L, Ramous E (1983) Laser surface treatment by rapid solidification. Lasers Mater Process Conf Proc 108–114.

[3] Georges C, Semmar N, Boulmer-Leborgne C (2006) Effect of pulsed laser parameters on the corrosion limitation for electric connector coatings. Opt Lasers Eng 44:1283–1296.

[4] Adamczyk J, Grajcar A (2006) Effect of heat treatment conditions on the structure and mechanical properties of DP-type steel. J Achiev Mater Manuf Eng 17:305–308

[5] Li L (2000) The advances and characteristics of high-power diode laser materials processing. Opt Lasers Eng 34:231–253.

[6] Bourithis L, Papadimitriou GD, Sideris J (2006) Comparison of wear properties of tool steels AISI D2 and O1 with the same hardness. Tribol Int 39:479–489.

[7] Brooks CR (1992) Principles of the austenitization of steels. Elsevier, England.

[8] Torkamani H, Raygan Sh and Rassizadehghani J (2011) Evaluation of microstructure and toughness of AISI D2 steel by bright hardening in comparison with oil quenching. AIP Conf Proc. 438–442

[9] ASM International (2004) Metallography and microstructures, Vol 9, ASM Handbook, ASM International.

[10] Vural M, Muzafferoglu HF, Tapici UC (2007) The effect of welding fixtures on welding distortions. J Achiev MaterManuf Eng 20:511–515.

[11] Rykalin N, Uglov A, Zuev I, Kokora A (1988) Laser and electron beam material processing handbook. Mir Publishers, Moscow.

[12] Mordike BL (1995) Surface treatment with high power lasers. Lasers Eng 4:187–200.

[13] Amine T, Newkirk JW, Liou F (2014) An investigation of the effect of direct metal deposition parameters on the characteristics of the deposited layers. Case Stud Therm Eng 3:21–34.

[14] Kou S (2003) Welding metallurgy, 2nd edn. Wiley, Hoboken, pp 170–200.

15] Avner (1974) Introduction to physical metallurgy. Mc GRAW-Hill, New York.

[16] Bayraktar E, Grumbach M, Kaplan D (2007) Effect of forming rate on the impact tensile properties of the steels under crash test. J Achiev Mater Manuf Eng 20:55–61.

[17] Dobrzański LA, Piec M, Labisz K, Bonek M, Klimpel A (2007) Functional properties of surface layers of X38CrMoV5-3 hot work tool steel alloyed with HPDL laser. J Achiev Mater Manuf Eng 24: 191–194

# IV. INVESTIGATION OF EFFECT OF PROCESS PARAMETERS ON MULTILAYER BUILDS BY DIRECT METAL DEPOSITION

Tarak Amine, Joseph W. Newkirk and Frank Liou

Applied Thermal Engineering

Received 28 November 2013/ Accepted 2 August 2014



**ABSTRACT**

Multilayer direct laser deposition (DLD) is a fabrication process through which parts are fabricated by creating a molten pool into which metal powder is injected as. During fabrication, complex thermal activity occurs in different regions of the build; for example, newly deposited layers will reheat previously deposited layers. The objective of this study was to provide insight into the thermal activity that occurs during the DLD process. This work focused on the effect of the deposition parameters of deposited layers on the microstructure and mechanical properties of the previously deposited layers. It is important to characterize these effects in order to provide information for proper parameter selection in future DLD fabrication. Varying the parameters was shown to produce different effects on the microstructure morphology and property values, presumably resulting from in-situ quench and tempering of the steels. In general, the microstructure was secondary dendrite arm spacing. Typically, both the travel speed and laser power significantly affect the microstructure and hardness. A commercial ABAQUS/CAE software was used to model this process by developing a thermo-mechanical 3D finite element model. This work presents a 3D heat transfer model that considers the continuous addition of mass in front of a moving laser beam using ABAQUS/CAE software. The model assumes the deposit geometry appropriate to each experimental condition and calculates the temperature distribution, cooling rates and re-melted layer depth, which can affect the final microstructure. Model simulations were qualitatively compared with experimental results acquired in situ using a K-type thermocouple.

**Keywords**: Direct metal deposition, Microstructure, 3D finite element modeling, Stainless steel 316L.

# 1. INTRODUCTION

In the direct laser deposition (DLD) process, the material in a single deposited layer typically is not enough to create a part. Several layers must be deposited sequentially to achieve a fully built part. With each subsequent deposited layer, the previously deposited layers are reheated. This is but one simple example of how multiple temperature gradients can be created during the additive layering process, which could influence the material being deposited. These gradients, resulting from the repeated nonuniform heating and cooling process not only affects the mechanical performance and the post-machining precision of the fabricated component, but also results in fabricated component distortion, and possibly even cracking.

The complex thermal behavior that occurs during the DLD process results in a complex microstructure evolution. Mostly attributable to its stepwise additive nature, the thermal cycles associated with the DLD process can involve several reheating cycles. However, in building complex geometries adjacent deposition tracks, junctions, and interrupted deposition all could add further reheating steps to a reference volume. Thus, the goal of any assessment of microstructural evolution is to determine the response of the deposited alloy to these cycles [1].

The microstructure of the material formed from the molten pool is most strongly related to the cooling rate during the solidification process. Further microstructural evolution takes place in the solid state depending on the subsequent temperature field and profiles developed within the samples as the laser is traversed during the build operation. Thus, it is important to control the temperature profiles during the DLD process so that an ideal microstructure can be achieved in the fabricated component. The most important DLD parameters include the laser power (W), travel speed (mm/min) and powder feed rate (g/min), which all significantly affect the microstructure of the formed parts [2].

There have been a number of studies looking at deposition parameters on the resulting properties and structure. Zhang carried out some experiments depositing 316 SS to determine the influence of processing parameters on dilution ratio in laser clad layer. The results showed that the influence degree of scanning speed is most significant, while that of laser power is relative slight [3]. Wu studied the effects of processing conditions,

such as laser power, scan speed, powder feed rate on the microstructure of Ti6Al4V. They concluded that the microstructure of deposited Ti6Al4V is influenced by laser power, scan speed or powder feed rate, but the effects of each parameter are not straightforward [4]. Rasheedat investigated the influence of the scanning velocity on the evolving physical properties, the microstructure, the microhardness and the wear resistance behavior of Ti6Al4V/TiC composite. Ti6Al4V. The deposit was successfully at various scanning velocities between 0.015 and 0.105 m/s at an interval of 0.01 m/s. As the scanning velocity was increased, the microhardness also increased. Also, the wear resistance performance of the samples increased as the scanning velocity was increased [5].

Much fundamental research on the thermal behavior has concentrated on investigating the temperature distribution and cooling rate during the solidification process. However, the DLD process is more complicated than a series of successive solidifications of molten pools. As already stated, during laser deposition, the previously deposited layers reheat when a new layer is deposited on top of them. The temperature of the sample varies from one location to another and from one point in time to another. So far, however, there has been limited research on the effect of the reheating process which accompanies a multilayer build. In order to understand the evolution of the microstructure and control the microstructure, it is important to understand the thermal history of the deposited component during the DLD process.

There has been some work on the modeling of the thermal history of deposited metals. However, most of this work has been limited to modeling a single layer and has ignored the effects of subsequent deposition on the already deposited material. Finite element modeling studies have been reported for the application of some materials including stainless steel alloys, titanium alloys, nickel-based alloys, tool steel and other specialty materials, as well as composite and functionally graded material deposition using simultaneous feed of powder and wire in DLD processing for a single layer.

Fu, developed a model to simulate the temperature distribution and residual stresses in the single-pass powder laser deposition process, the results showed that less difference of thermal conductivity and thermal expansion coefficient between powder material and substrate material produces lower residual stress; higher laser power, laser

scanning speed and smaller laser beam diameter can lead higher peak temperature and higher residual stress [6]. Giuliani, developed a model to predict the powder temperature distribution for a laser with top-hat and Gaussian intensity distribution, as well as the temperature profile for a single-track laser The results showed that a more vertical position of powder delivery nozzle will lead to a higher and more uniform particle temperature distribution, in particular for the top-hat intensity distribution case [7]. Vahid et al. developed a model to simulate the shape and geometries of the real-time melt-pool and to predict the local solidification condition along the solid/liquid interface for a single-track laser the temperature gradient and interface velocity can be accurately evaluated along the predicted solid/liquid interface [8]. Pinkerton and Li developed a simple thermal model to analyze the temperature distribution and estimate the molten pool size in laser cladding [9]. Liu and Li established a model to investigate the effects of process parameters on laser direct formation of thin wall [10]. Jendrzejewski et al. developed a two-dimensional thermal model to understand the temperature distribution in laser multi-layer cladding [11].

In this work, a transient thermal model for a thin wall build by succeeding multiple layerswas developed to reveal the heating and reheating cycles during the DLD process. The model assumes certain geometries appropriate to process parameter combinations and was used to predict the temperature distribution, thermal gradient, remelted layer depths, peak temperatures and cooling rate as a function of process parameters, such as laser travel speed (mm/min) and laser power (W), which can affect the final microstructure and elemental distribution in the part as well as the mechanical properties of deposited material.

A 3D finite element temperature field model for DLD developed using ABAQUS/CAE software demonstrated the model's thermal history in stainless steel SS 316L. Transient thermal analysis first was performed within ABAQUS/CAE to determine the temperature history at each reference position in the deposited material. Eq. (1) is the heat conduction governing equation:

## 2. THERMAL MODELING

Fig. 2.1 depicts a flow chart showing various steps in the computational scheme employed in the study. The entire deposition process was modeled as a multistep transient heat transfer analysis in which each time step was further divided into a number of smaller time increments. The continuous addition of metal powders was considered by means of the successive, discrete addition of a new set of elements into the computational domain at the beginning of each time step, whichwas fixed such that the laser beam scanned a distance equal to a set of newly activated elements.

The number of elements activated at each time step was determined from the volume of powder materials expected to enter the melt pool during that time step, which depended on the powder feed rate (f) and the travel speed of the laser (v).

A 3D finite element temperature field model for DLD developed using ABAQUS/CAE software demonstrated the model's thermal history in stainless steel SS 316L. Transient thermal analysis first was performed within ABAQUS/CAE to determine the temperature history at each reference position in the deposited material. Eq. (1) is the heat conduction governing equation:

$$\frac{\partial}{\partial x}\left(K\frac{\partial T}{\partial x}\right)+\frac{\partial}{\partial y}\left(K\frac{\partial T}{\partial x}\right)+\frac{\partial}{\partial z}\left(K\frac{\partial T}{\partial z}\right)=\rho Cp\frac{\partial T}{\partial t} \qquad (1)$$

where r, Cp, and k refer to the density, specific heat, and thermal conductivity, respectively, of the metal powder and the substrate material; and T and t represent the temperature and time variables, respectively. The terms on the left side of Eq. (1) refer to the conductivity heat transfer in the x, y, and z directions, respectively.

The terms on the right side of Eq. (1) refer to the transient nature of the heat transfer process.

The first step began with a substrate material, $T_0$, initially at room temperature, as shown in Eq. (2). At the beginning of each subsequent step, a new group of finite elements was activated.

$$T(x,y,z)=T_0 \qquad (2)$$

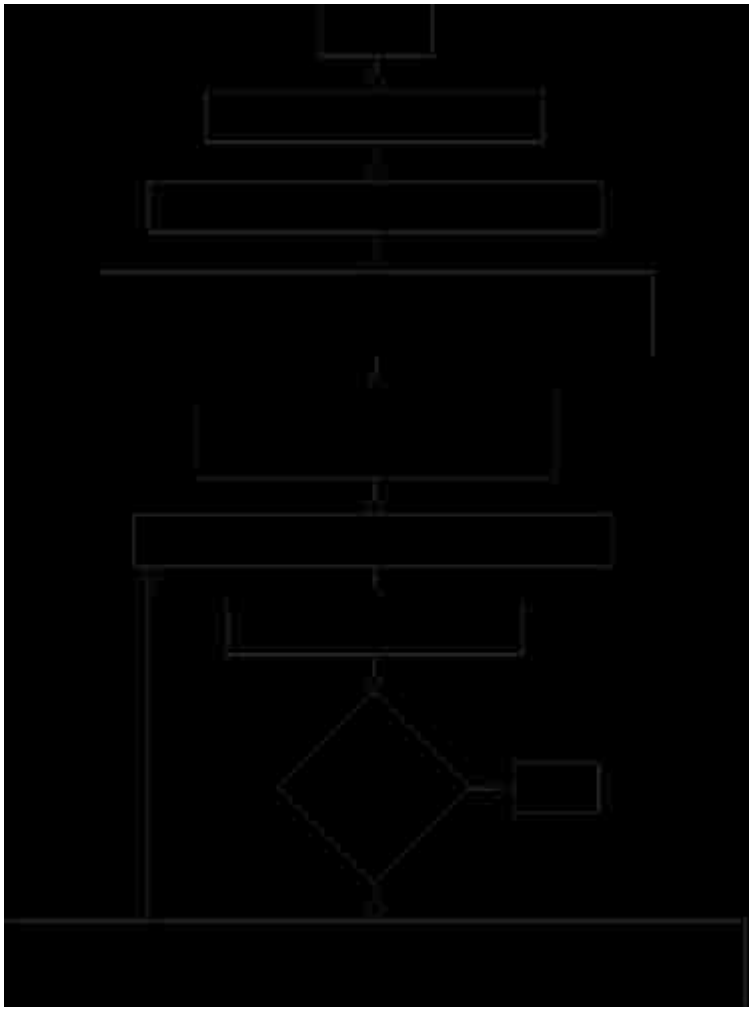

Figure 2.1. Flow chart showing various steps involved in the temperature distribution model

Given the melt generation and resolidification associated with the phase change effects, the specific material properties used as inputs in the current analysis were density, thermal conductivity (k), specific heat, enthalpy (H) and latent heat for varying temperature ranges. Numerical values of these material properties as adopted from Ref. [12] and used in the analysis appear in Table 2.1. All substrate surfaces exposed to the environment were assumed to have lost heat due to free convection.

Table 2.1. Thermal material properties for stainless steel 316L as used in the finite element modeling

| Temperature (K) | 300 | 400 | 500 | 600 | 700 | 800 | 1000 |
|---|---|---|---|---|---|---|---|
| Specific heat (kJ/kg K) | 468 | 504 | 527 | 550 | 563 | 602 | 602 |
| Expansion coefficient alpha (m/m K) | 1.52E-5 | 1.61E-5 | 1.69E-5 | 1.75E-5 | 1.79E-5 | 1.83E-5 | 1.88E-5 |
| Conductivity (W/m K) | 13.4 | 15.2 | 16.75 | 18.3 | 19.8 | 21.3 | 24.2 |

In order to simulate mass addition (powder deposition), the "birth and death" feature in ABAQUS/CAE was used. Initially, all elements in the deposited track were "killed". The total time required for the laser beam to travel along the deposited track of each layer was divided into a number of small time steps to which variable flux and boundary conditions were applied. The first born of the element set appeared with applying these conditions. For the subsequent element sets, the model used the results of the previous step as the initial condition for the new active element set.

Finally, according to Rosenthal's Eq. (3), the moving heat source was simulated by applying a concentrated surface heat flux on the model for a time equal to the distance between the model element sets divided by the laser travel speed. A user subroutinewas written to calculate the position of the laser at a given time as a function of its speed (v) and the Gaussian flux distribution in terms of spatial coordinates.

$$\rho Cp\frac{\partial T}{\partial t}+\rho Cp\nabla.(vT)-\nabla.(K\nabla T)=Q \qquad (3)$$

Where T is the temperature and Q is the power generation per unit volume of the material.

As assumed in the simulation, the interaction of the heat flux with both the substrate and the deposited material follows the schematic in Fig. 2.2, such that at time t during beamscanning, the heat flux as the source of heat from the laser beam was modeled at the location Lt on the surface of the substrate along the path of scanning. This

simulated the impinging beam onto this surface at that instant, resulting in the generation of a melt pool. The deposit was the solidified form of powder particles added into the melt pool, so it was modeled on top of the heat source to simulate the volume of added powder particles. As the beam moved to a new location after a time t þ dt, the heat flux correspondingly moved to the location Lt þ dt, with vdt being the length of deposited material over the incremental time dt. The analysis was divided into several steps in order to move the heat flux from the laser over the nodes in the laser path.

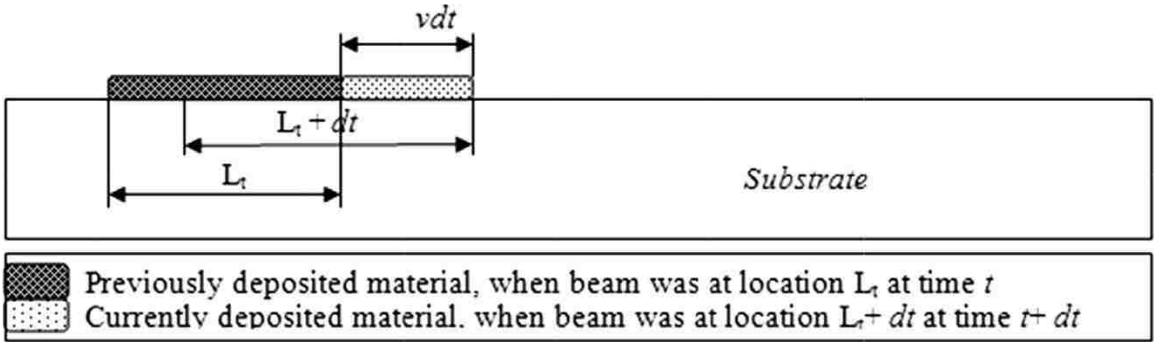


Figure 2.2. Schematic illustration of beam/substrate interaction at different times during beam scanning, and length of clad, vdt, which is manufactured in every scan over a time of dt.

## 2.1. GEOMETRIC MODEL OF THE THIN WALL

In order to predict the temperature distribution of the deposited thin wall in the DLD process, a 3D finite element and meshes were built using Hypermesh software, as shown in Fig. 2.3. The mesh on the geometry, which represents its discretization into the elemental form, is made of thermal 8-node linear brick type elements. It was generated such that the wall region, where fusion occurs and more severe temperature gradients are expected, was assigned the finest mesh, and regions further from the wall were assigned a relatively coarse mesh [13e16]. The DLD process was simulated using ABAQUS/CAE.

The structure of the deposited thinwall in themodel was built by depositing multi-layer and single-layer tracks on top of each other with a length of 30mm, total height of 14mm, and width of 2.5mm. The wall was fabricated on a surface of 316L stainless steel

that was 50 mm wide, 50 mm long and 12.7 mm thick. To simulate the laser deposition process, the following assumptions were made:

- The initial temperature of the workpiece was assumed as 295 K. The workpiece and the coordinate mesh were fixed. The laser beam was moved in both the positive and negative z-direction with a constant speed v. For newly deposited layers, the laser beam was moved up in the positive y-direction.
- A subroutine was written to consider the effect of conduction, convection and radiation during the laser deposition process.
- The following boundary conditions were applied to the deposited thin wall:

  $q = -h(T - T_0)$

  $q = \sigma(T^4 - T_0^4)$

  Where q is the heat flux per unit area, h is the convective heat transfer coefficient, ε is emissivity, s is the Stephane Boltzmann constant and T0 is the ambient temperature.
- The thermo-physical properties of 316L stainless steel were considered as function of the temperature, as illustrated in Table 2.1.
- A radiation boundary condition was applied to the entire deposited thin wall. The phase transformations in metal powder during deposition, melting and solidification results in changes of emissivity, a constant value of 0.4 was assumed.

The thermal load, applied as a function of the distance, was determined using Eq. (4):

$$DFLUX(1) = -q(0) \times e^{-cr^2} \qquad (4)$$

where r=x2+y2+z12, and z1=z−v(T−t). v is the speed of movement in z-direction, T is the lag factor that defines the time at which of the laser gun is at first position, t is time, z1 is movement along z-axis, and z is a fixed coordinate axis.

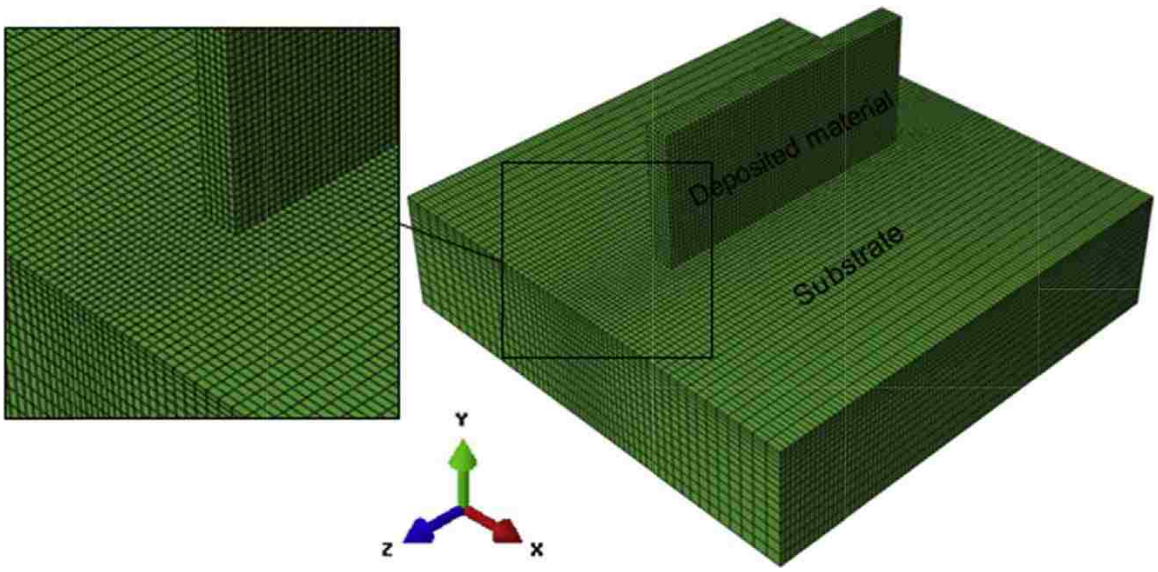


Figure 2.3. Three D finite element model build and meshes using hypermesh software

# 3. EXPERIMENTAL PROCEDURE

The apparatus used for DLD consists of a 1 KW diode laser (coherent diode laser) with a 5 mm beam diameter, a powder feeder and a 5-axis FADAL computer numerical control CNC (VMC3016). This system has been described in more detail in Ref. [17]. A computer-aided design (CAD) file and CNC control system were used to control the X, Y movement and Z increment.

The substrate material and the deposition powder was 316L stainless steel, a common commercial alloy. The substrate measured 50 * 50 * 12.7 mm in length, width and height, respectively. The chemical composition range of 316L stainless steel appears in Table 3.1. The offset between the laser head and deposition point was a constant 5mm.

Table 3.1. The chemical composition range of 316L stainless steel

| Element | C | Mn | P | S | Si | Ni | Cr | Mo | Fe |
|---|---|---|---|---|---|---|---|---|---|
| (W %) | < 0.03 | < 2 | < 0.045 | < 0.03 | < 1 | 10 - 14 | 16 - 18.5 | 2 - 3 | Bal. |

A series multi-layer thin walls were deposited. The process parameter combinations used in the model and also in the experimental runs are shown in Table 3.2. A DOE L9 Taguchi model was used with three levels for each of the three parameters. The DOEwas repeated for build schemes which used a zigzag laser scan, where alternating layers are deposited in the reverse direction versus a parallel laser scan where all layers are deposited in the same direction. In order to examine the influences of these parameters on the microstructure and properties of the deposited layers, the change of the microstructure of the cross-sections of the deposited layers obtained at different laser powers and traveling speeds was observed and analyzed using scanning electron microscope (SEM). Subsequently, the mechanical properties, such as hardness, were examined at different positions in the deposited wall layers.

In order to validate the model, the temperature history during the (DLD) process was experimentally measured by three K-type thermocouples positioned on the underneath surface of the substrate at the midpoint and the ends of the laser track. The depth was varied such that the thermocouples were located 1, 2, and 3 mm below the top surface of the substrate. These locations were evaluated with the FEA model output as ones where the temperatures attained in that region would not damage the thermocouples. These locations will be referred to as the reference positions for the measured temperatures.

Table 3.2. Process conditions monitored

| Sample # | Laser power(w) | Traveling speed (mm/min) | Powder feed rate (g/min) |
|---|---|---|---|
| 1 | 600 | 300 | 8 |
| 2 | 600 | 375 | 10 |
| 3 | 600 | 450 | 12 |
| 4 | 750 | 300 | 10 |
| 5 | 750 | 375 | 12 |
| 6 | 750 | 450 | 8 |
| 7 | 900 | 300 | 12 |
| 8 | 900 | 375 | 8 |
| 9 | 900 | 450 | 10 |

The temperatures were recorded with a data logging system at a rate of 100 Hz. The data logging system was initiated prior to the deposition and continued for several minutes after the deposition had finished. The thermocouples were connected via an interface box to a computer that monitored the temperatures at those positions during material deposition. As a result, the whole thermal history of the instrumented locations during the deposition process, including the cooling period after the deposition, was recorded. The modeling results were compared with the experimental results. The model

is important to determine the parameters that would assure a constant molten pool temperature consistent with a multilayer deposition and therefore this validation step is critical in the development of this model.

# 4. SIMULATION ANALYSIS

The influence of the laser parameters on the shape and size of the laser melting poolwas evaluated by specifying the actual power (P), travel speed (v) and beam diameter (Db) as the specific energy (Es) by means of Eq. (5).

$$E_s = P/(D_b \times v) \quad (5)$$

## 4.1. TEMPERATURE DISTRIBUTION DURING BUILD

Fig. 4.1 illustrates the transient temperature distribution contour plot for the first deposited layer for the case of Q = 600 W and V = 300 mm/min. The location of the laser beam is evident from the intensity of the temperature distribution, where the maximum contour limit of 1996 °C signifies the melt pool. The thermal history was essentially independent of the vertical free edges once the laser reached the center of the wall, where the mesh was highly refined, as shown in Fig. 2.3, for accurate extraction of the thermal gradient and cooling rate.

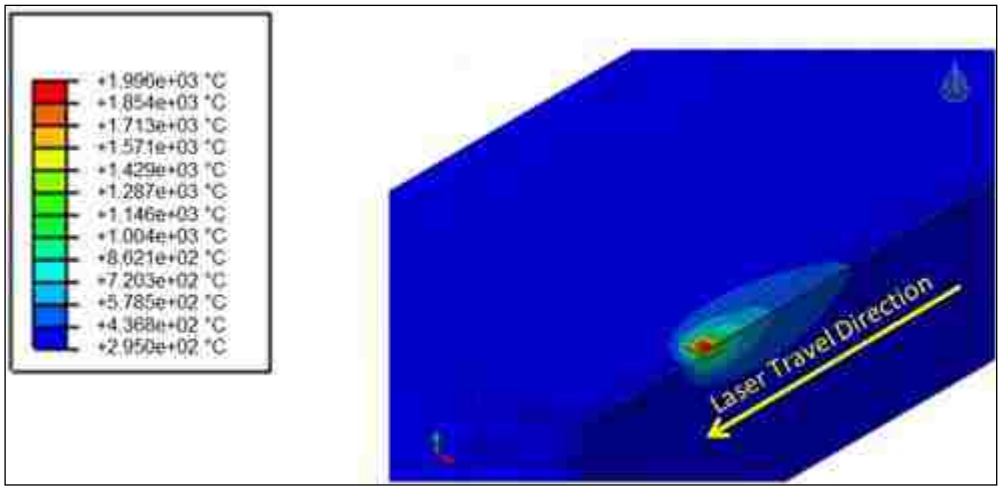


Figure 4.1. Temperature contours for Q=600 Wand V=300 mm/min

Fig. 4.2a and b illustrates the temperature distribution along the deposited layers and substrate simulated using the defined laser parameters. The temperature of each nodal point within the solid was calculated as a function of time. The bottom of the deposited layers cooled faster than the top because of heat conduction to the substrate, while showing significant temperature gradients along the height of the deposited layers.

Thermal energy from the laser increased the node temperature beyond the melting temperature. Once the laser moved away along its track, the node began to cool. The next pass of the laser caused the temperature of that node to increase higher than during the previous laser pass.

Regarding the thermal histories within the deposited material during deposition, Fig. 4.3 shows the temperature variation of the underneath surface of the first deposited layer at the right end (T1), middle (T2) and left end (T3) of the deposited wall with depths of 1, 2, and 3 mm, respectively, which directly impinged on the substrate, while the subsequent 87 layers were deposited in sequence with parallel deposition.

Oscillations were the most obvious characteristic of the temperature measurements. Each temperature peak represented the thermocouple's response as the laser passed over it. The temperature increased when more and more energy was transferred to this position by heat conduction. The thermal excursion decayed when either the energy source moved away from the thermocouple during the deposition of a layer or when subsequent layers were deposited. The thermocouples were attached on the substrate, so the measured temperatures were much lower than those near the molten pool.

As seen in Fig. 4.2a and b, the numerical results are similar to the experimental results, although somewhat lower. The simulated results using different values of absorptivity were compared with the experimental results, and closest fit, approximately 20% difference, was observed for an absorptivity of 0.6. This temperature difference was significantly lower during the cooling stage. The difference in the measurement was approximately 100 °C, which could have been slightly higher because the thermocouple beads were exposed to some laser energy by radiation. Another explanation could be the thermos physical properties used were not appropriate. A slight phase shift was also observed between the graphs of the simulated and experimental results. This shift could

have been due partially to the acceleration/deceleration of the laser; additionally, the dwell times while changing laser tracks between layers was not considered in the model [15].

The cooling rate of the FEA model was extracted from the time difference between when the nodes in the center of the deposited material were seen at the last liquids temperature and at the next solidus temperature. At each nodal location, the solidification cooling rate was determined using Eq. (6):

$$\frac{\partial T}{\partial t} = \left|T_1 - T_S\right| / \left|t_1 - t_s\right| \qquad (6)$$

Where dT/dt is the cooling rate, $T_l$ - Ts is the difference between the liquids and solids temperatures, and $t_l$ - ts is the time interval between $T_l$ and Ts.

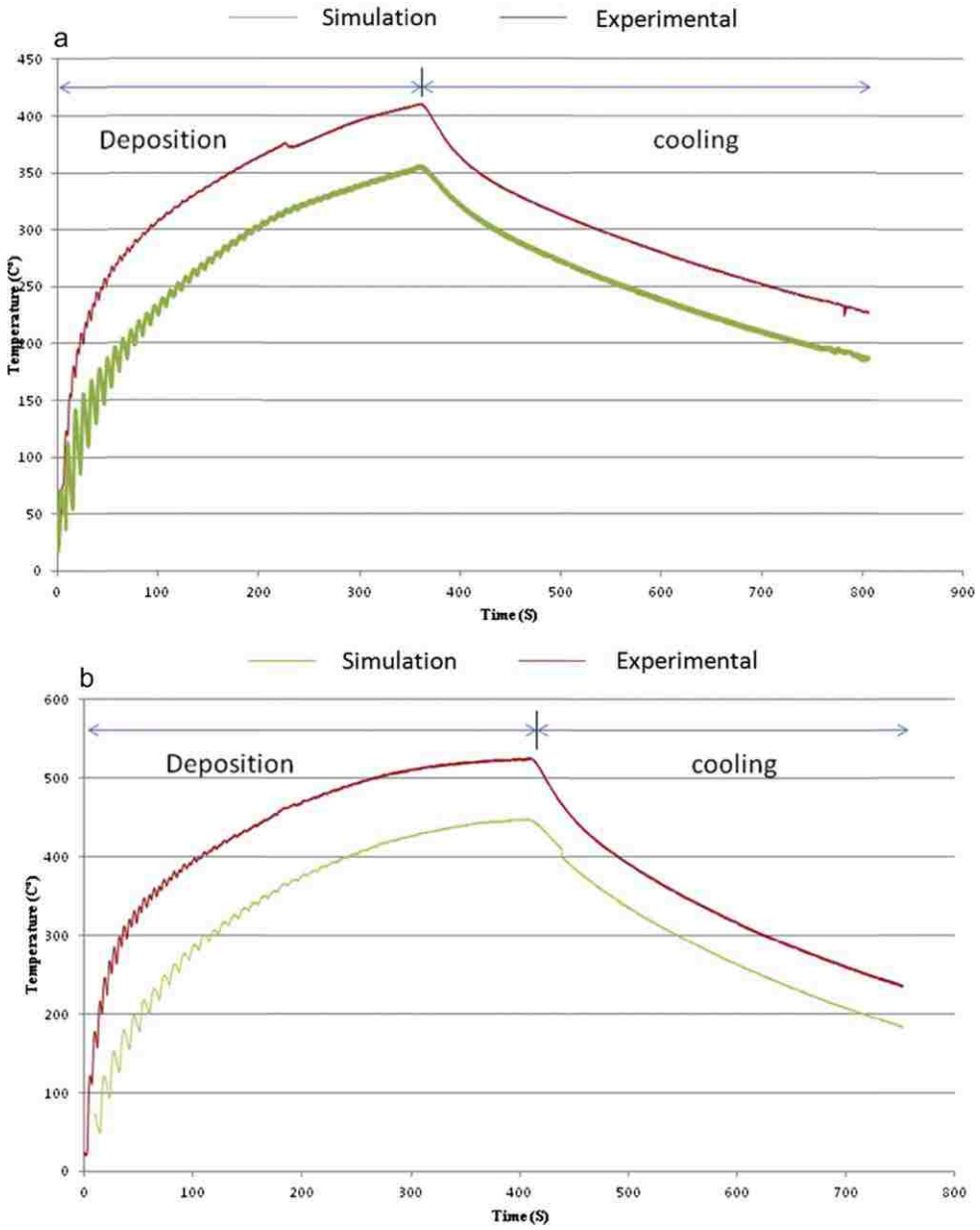


Figure 4.2. Comparison of simulation and experimental results predicted at different reference positions: (a) 600 W, 450 mm/min, 12 g/min, (b) 900 W, 375 mm/min, 8 g/min.

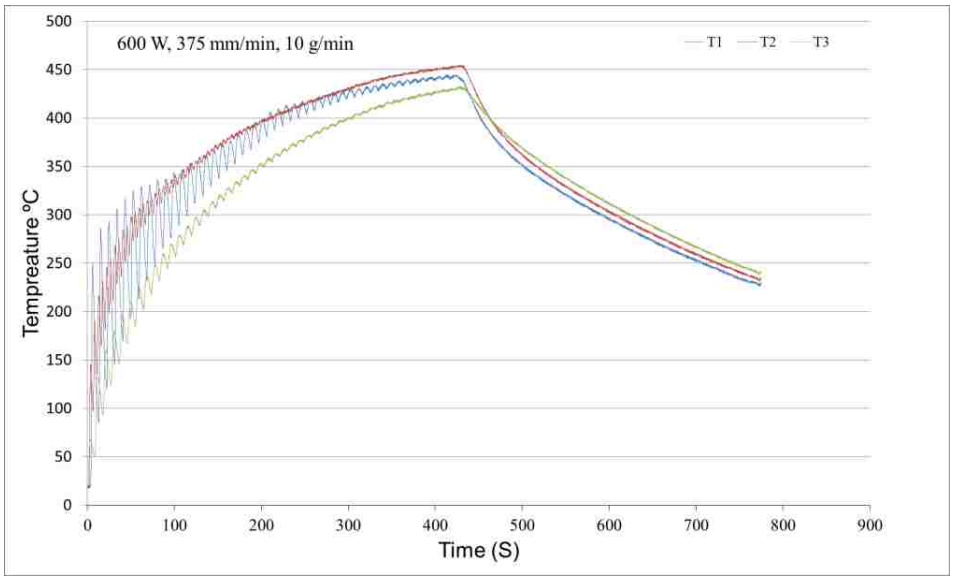


Figure 4.3. Thermal history at the underneath surface of the first deposited layer, while 87 subsequent layers are deposited.

The computed results of the FEA model showed that the cooling rate of the thin wall was affected by the height of the built wall. The cooling rate was high at the beginning of the deposition process in the first and second layers because of the greater heat transferred to the substrate, but then it decreased with the addition of subsequent layers. The predicted cooling rate at the top of the build was around 200 °C/s, while adjacent to the substrate was around 4000 °C/s. This large difference in the cooling rate could be detrimental to the building of a uniform microstructure. Controlling the laser power to follow the increasing height of the deposition would be required to alleviate these phenomena.

**4.2. REMELTING DURING BUILD**

The model was also used to predict the remelting depth during laser deposition, an important factor to consider. The frequent remelting of previous layers can lead to unwanted precipitation of phases or solutes, which can become detrimental metallurgically. Fig. 4.4a and b shows the simulated remelted layer depths of deposited layers. These results were extracted from the simulation when the solidified node remelted ($T > T_m$) each time the laser beam passed over it. In general, the depths of the

remelted layers were high, except for in the first layer, which was adjacent to the substrate and had difficulty melting completely because of the heat extraction by the substrate via heat conduction.

Fig. 4.4a and b illustrates that the remelted depth accompanying the parallel laser scanning path was lower than that accompanying the zigzag path during the early stage of deposition because of the slightly higher cooling rate, though this effect eventually disappeared. Also, a lower laser power resulted in fewer remelted layers as a result of the higher cooling rate of the build wall.

Increasing the laser travel speed and/or decreasing the laser power reduced the melt pool depth. All of these extracted results provide important metallurgical information.

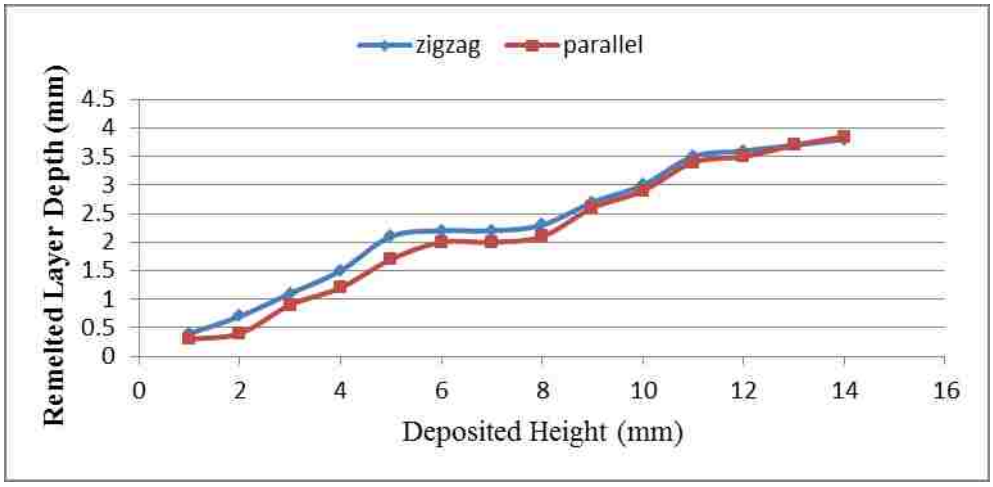


a

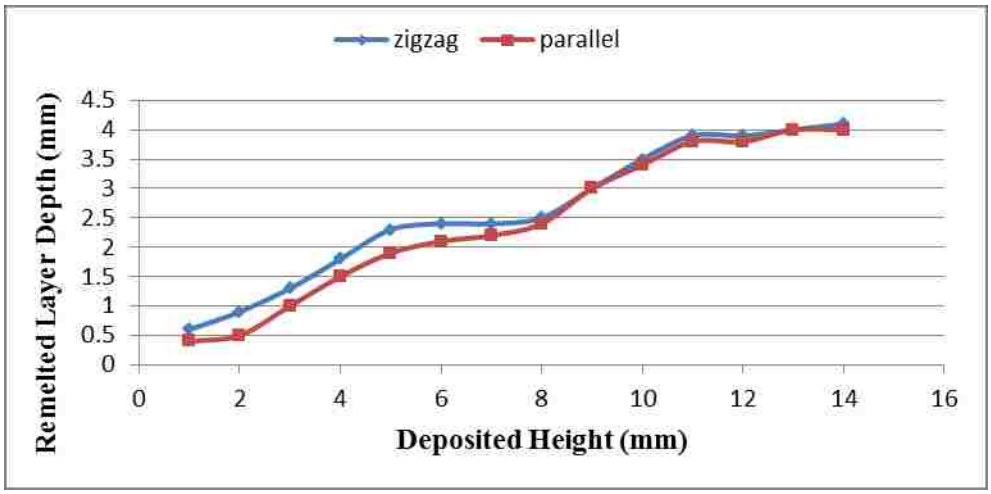


b

Figure 4.4. Computed remelted layer depth at (a) 600 W, 300 mm/min, (b) 900 W, 300 mm/min.

## 4.3. COOLING RATE DURING BUILD

The cooling rate at each location of the build is expected to effect both the microstructure and the hardness of the deposited material. The simulation was used to predict cooling rates and experiments were used to check the predictions.

Fig. 4.7 shows the FEA and DOE results of the effect of the laser parameters on the cooling rate at nine runs. The cooling rate values are the slope just after the peak temperature when the laser beam passes the measured point during the cooling time. The calculated cooling rate values were measured above 900 °C during the cooling time and

were the average of the slope of first few temperature peaks. In the process of rapid solidification with an ultra-high temperature gradient, it is beneficial to obtain an ultrafine microstructure, which results in a more uniform distribution of the components. The microstructure that forms in DLD parts is dependent on the cooling rate of each layer from the peak temperature at a certain point in the peak temperature period. Slow cooling rates result from conditions of high incident energy (high power setting and low travel speed), while fast cooling rates result from low laser power and high laser travel speed.

In general, the cooling rates experienced by laser-deposited 316L stainless steel samples decreased as the distance from the substrate increased due to the increased heat and the build-up of mass during deposition. Also, the highest cooling rate in any layer occurs at the highest travel speed and lowest laser power.

**4.3.1. Microstructure.** The microstructure plays a crucial role in determining the properties of a component. In this study, the optical and scanning electron micrographs of the top surface and cross-section of the laser deposited walls at each DOE point were observed in detail to study the morphology and secondary dendrite arm spacing (SDAS), as well as how these were affected by the laser parameters.

Fig. 4.5 shows SEM micrographs of different positions of the laser deposition zone prepared with an actual power of 600 W, laser travel speed of 300 mm/min. Whenever the laser power increased, the dendritic structures of the deposited material gradually altered from thin to coarse, which means that the primary dendritic spacing was augmented as the dendrite grew.

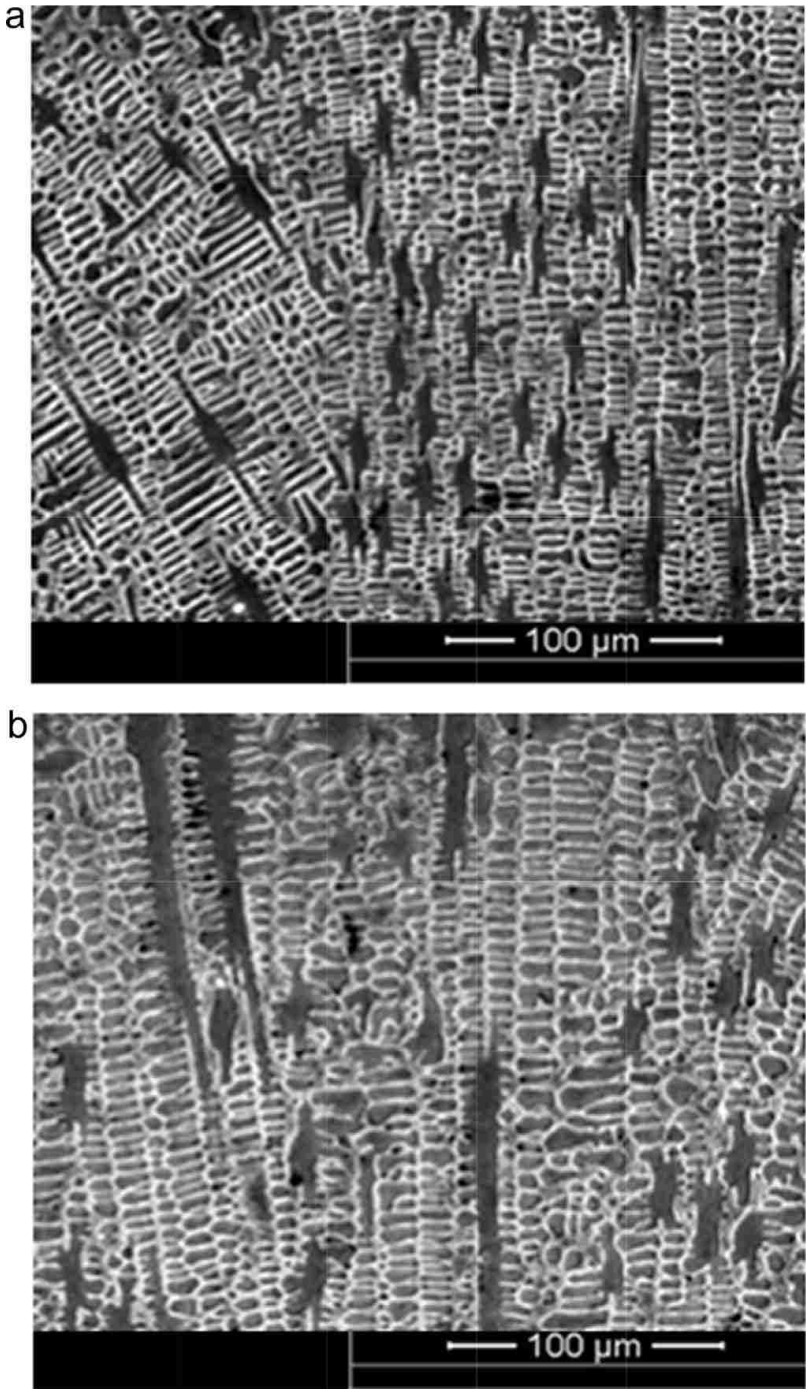


Figure 4.5. Microstructure at 600 W, 300 mm/min in different positions of the laser deposition zone: (a) top layers, (b) bottom layers.

As the laser travel speed increased, the microstructural composition of the deposited layer changed from coarse dendrites to fine dendrites. This change was attributed to a decrease in the ratio of the temperature gradient to the solidification rate, which can be estimated using Eq. (7) [18]:

$$G/R = 2\lambda K(T - T_0)^2 / \eta P v COS\theta \qquad (7)$$

where G is the temperature gradient, R is the solidification rate, v is the laser traveling speed, T is the temperature of the liquid, T0 is the initial temperature of the substrate, h is the laser absorption coefficient, P is the laser power and K is the thermal conductivity of the material.

A homogenous, defect-free, 316L stainless steel deposited microstructure was obtained. Fig. 4.6 shows the homogenous cellular appearance of the microstructure at the cross-section after the direct laser deposition of 316L stainless steel using the defined conditions. The deposition was free of cracks, and the microstructure was mostly cellular, with SDAS ranging from approximately 15-35 mm.

The microstructure of the deposited material has been shown to depend highly on the laser deposition process parameters. Under a narrow range of parameters, a defect-free, homogenous microstructure can be obtained [19,20].

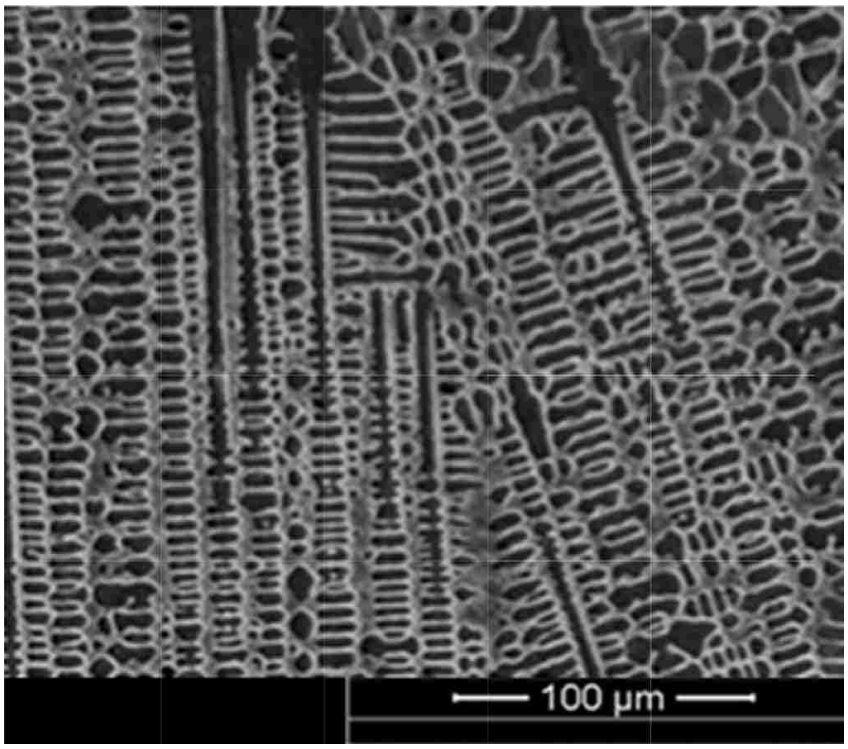


Figure 4.6. Appearance of homogenous cellular microstructure of laser-deposited stainless steel 316L600, 450 mm/min

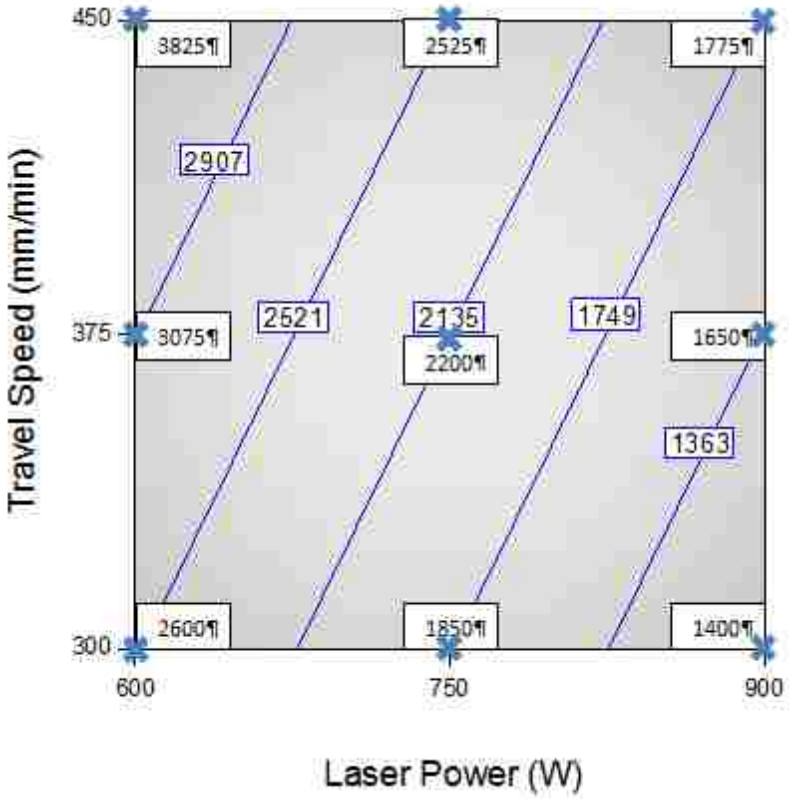


Figure 4.7. Cooling rates (°C/s) calculated from the FEA model for the first few deposited layers at the nine L9 deposition parameters. Note highest cooling rate at highest travel speed and lowest laser power

Observed from the side, the surfaces of the components exhibited a layered structure from the laser deposition and showed large, elongated grains. These grains grew epitaxially, inclined in a direction toward the layers following the temperature field resulting from the moving laser beam. Fig. 4.8 shows the experimental and DOE results of the effect of the laser parameters on the SDAS of the nine runs. The SDAS decreased as the traverse speed increased, as shown in Fig. 4.9a and b, but was largely affected by the power level. Thus, the SDAS also tended to increase with incident energy (= laser power/laser traverse speed), as seen in Fig. 4.9c. This trend was expected because SDAS typically decreases as the cooling rate increases. High energy results from a combination of high power and low travel speed, yielding a low cooling rate. Conversely, low energy results from a combination of low power and high travel speed, yielding a high cooling rate [23]. The SDAS was measured and is illustrated in Fig. 4.10a-c. The SDAS

correlates very strongly with the predicted cooling rates, providing confirmation of the models validity.

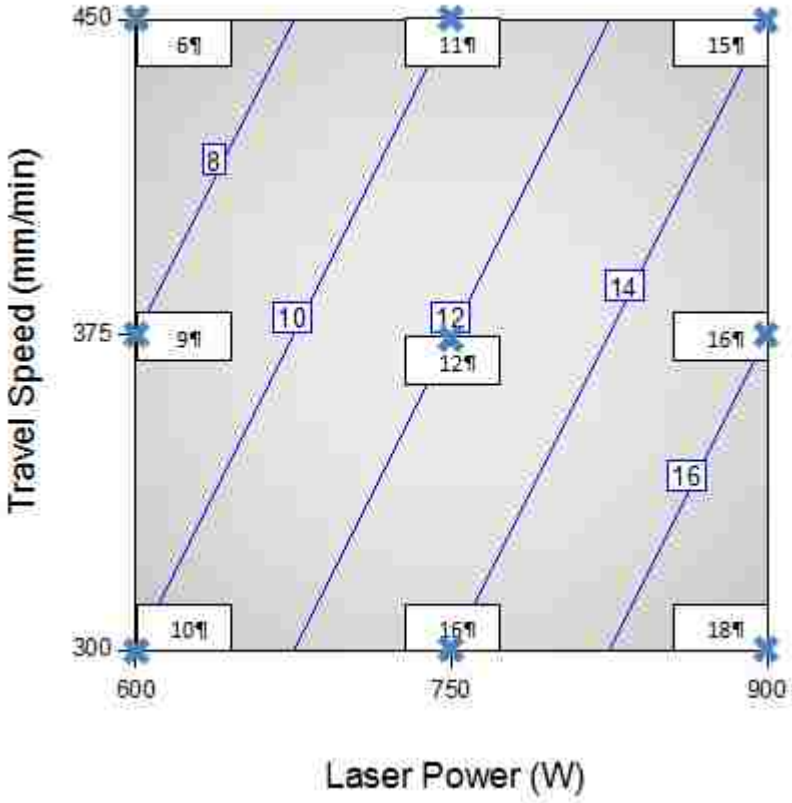


Figure 4.8. Measured SDAS (mm) for the nine L9 set of deposition parameters. Note the smallest spacing occurs at the highest travel speed and lowest laser power, correlating with the predicted cooling rates

In this work, the SDAS of the 316L stainless steel decreased as the cooling rate increased. As the cooling rate decreased, there was enough time for the small dendrite arms to melt and disappear, which occurred as a result of their high surface area to volume ratio increasing their total energy per unit volume. As the small dendrite arms disappeared, the SDAS of the alloys increased [2].

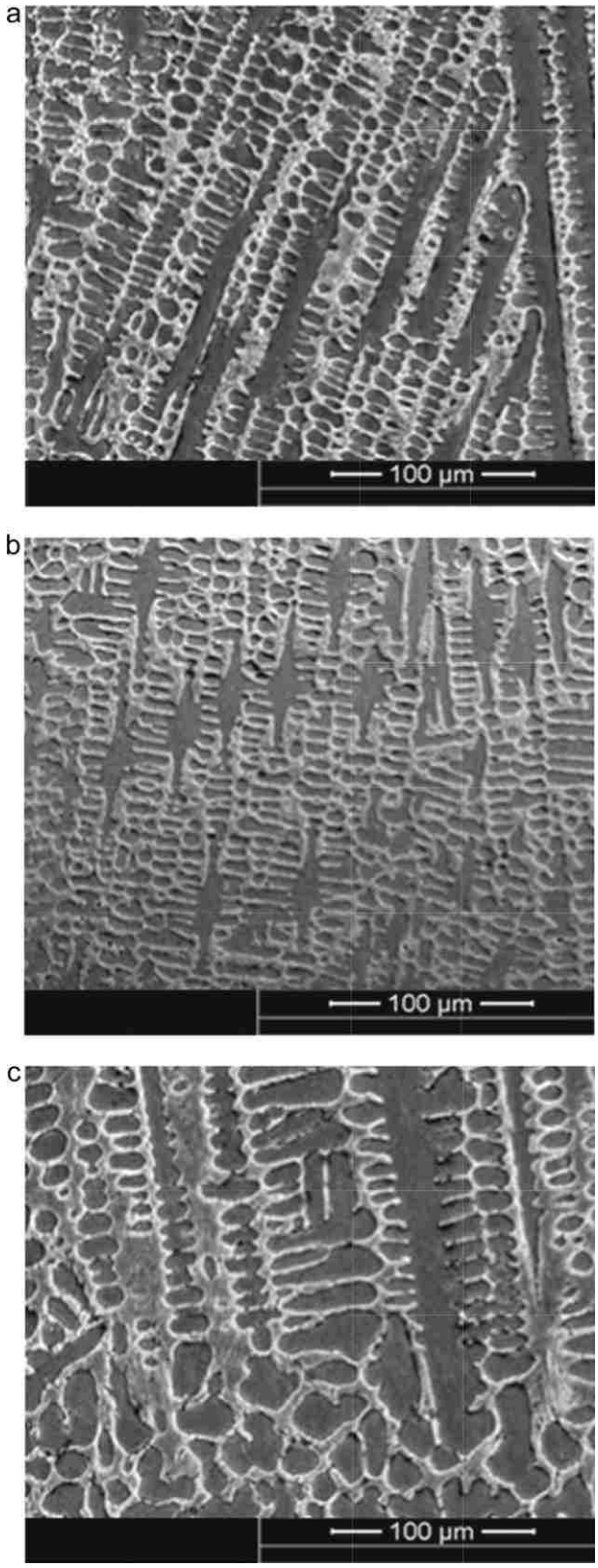


Figure 4.9. Microstructure at (a) 750 W, 300 mm/min, (b) 750 W, 450 mm/min, and (c) 900 W, 300 mm/min

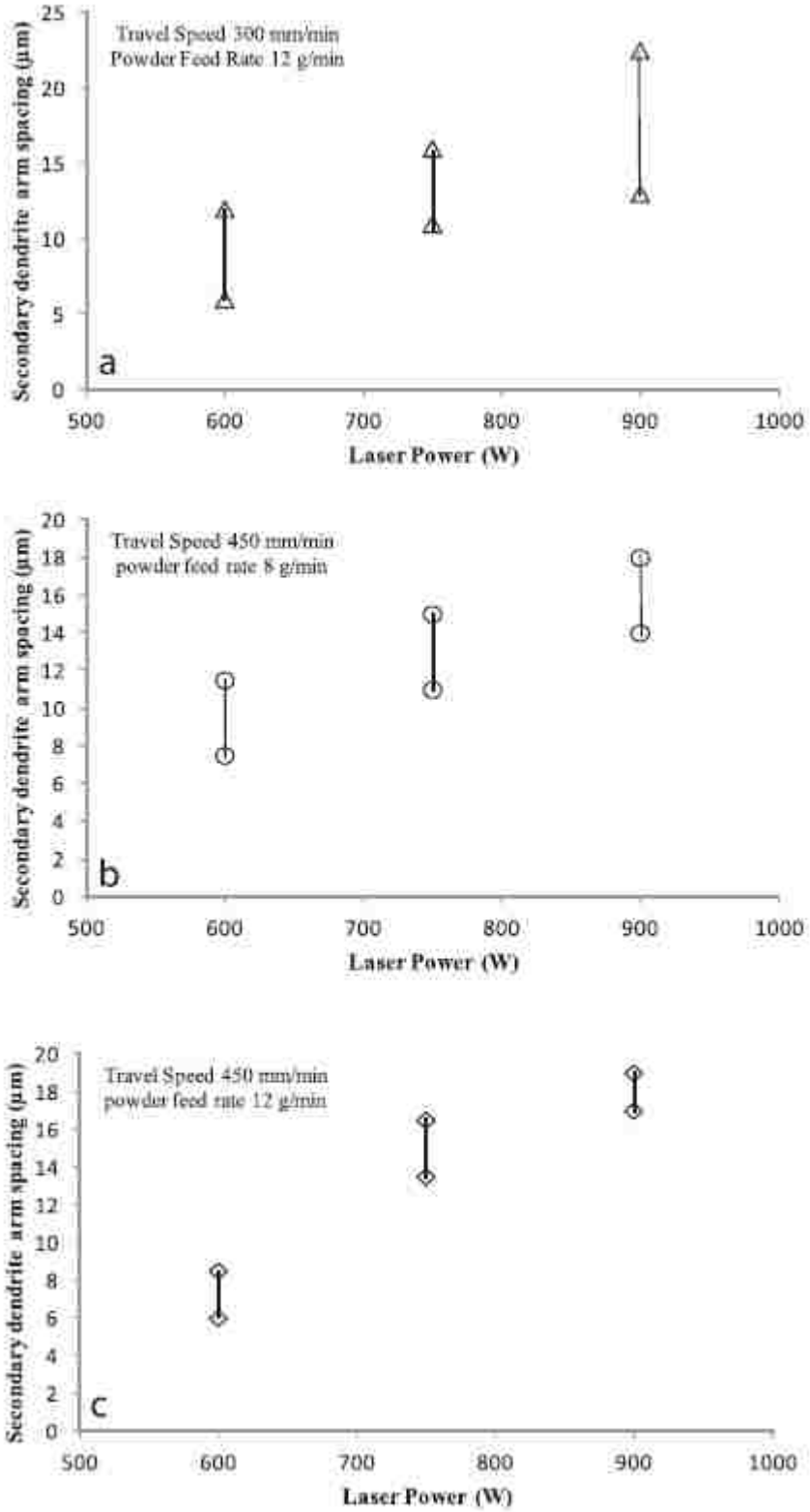


Figure 4.10. Range of secondary dendrite arm spacing (d) as a function of applied laser power for DLD of 316L stainless steel

**4.3.2. Hardness.** The microhardness analysis of the deposited specimens showed that the microhardness varied from 185 to 280 HV across all samples. Hardness variations were observed in both the deposited and heat affected zones. Increased hardness was attributed to the process parameters [21]. A comparison of the hardness values at each set of parameters did not show any correlation with the model or the measured SDAS. Ordinarily, in as-solidified materials, the hardness increases as the SDAS decreases, yet this trend was not observed. Apparently, the subsequent reheating of the deposited layers effected the resulting hardness in a complicated way.

The microhardness profiles of 316L stainless steel samples subjected to the investigated laser parameters are illustrated in Fig. 4.11a and b. Microhardness measurements were taken at increments of 1000 mm for the deposited region and 500 mm for the substrate.

The effect of the laser parameters on the hardness of the deposited material and heat affected zone are summarized in Fig. 4.12. The hardness values reported in the figures are the average values of the hardness measured in the deposited material and heat affected zone.

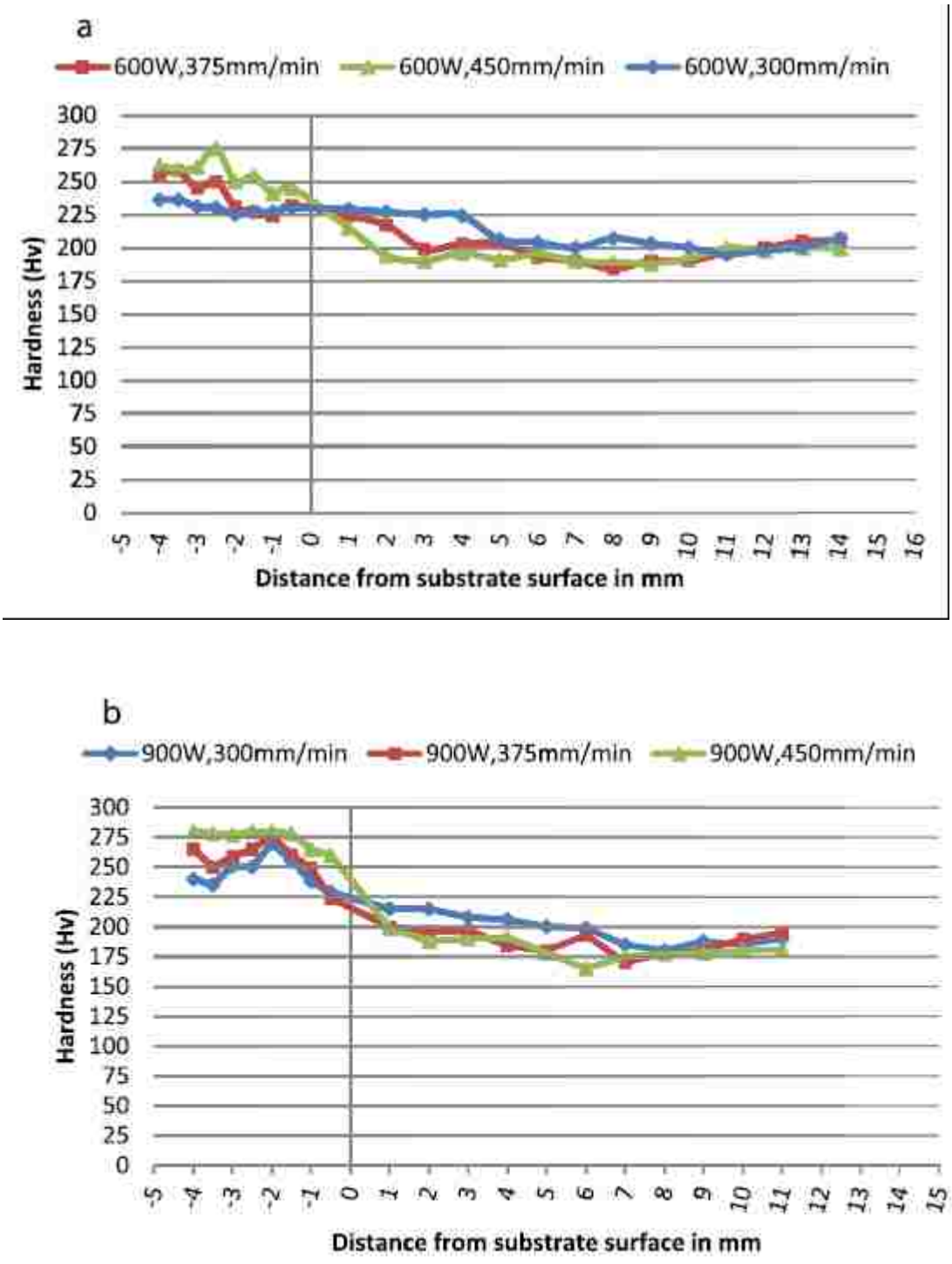


Figure 4.11. Microhardness profile at 300, 375 and 450 mm/min: (a) 600 W, (b) 900 W

In general, the hardness of the deposited material decreased as the laser power increased and as deposition progressed toward the top layers. On the other hand, the hardness of the heat affected zone increased with the laser power. At a constant laser power, the hardness of the deposited material decreased as the travel speed of the laser beam increased.

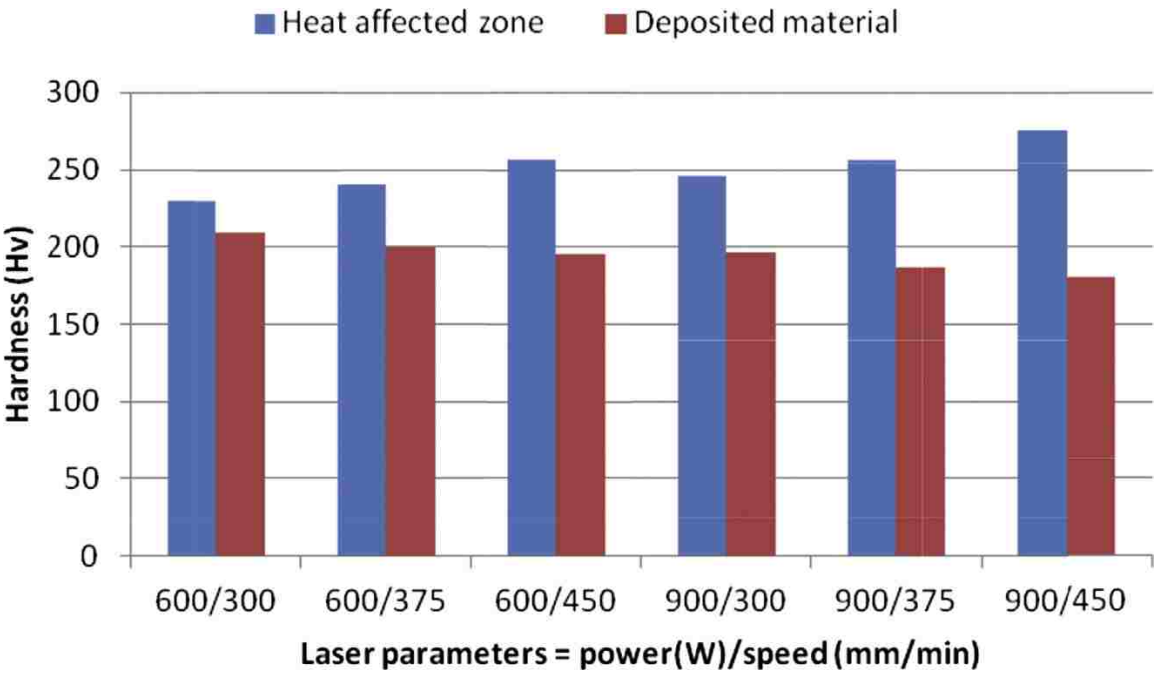


Figure 4.12. The effect of laser parameters on the hardness of deposited material and heat affected zone

Results published in the [22] literature showed reduced thermal activity as the energy source moves away from a substrate during deposition. At the beginning of material deposition, the heat quickly dissipated via the heat conduction of the substrate. This initial thermal transience produced a rapid quenching rate effect at the beginning stage of the laser deposition process, which resulted in increased hardness. As a result, the hardness the heat affected zone varied according to the location at which it was measured. The region close to the deposited material had higher hardness values than regions far away from the deposited material.

# 5. CONCLUSION

The temperature field evolution, thermal cycling characteristics, temperature gradient and effects of different deposition directions on the thermal activity of single-pass, multi-layer laser deposition fabrication were investigated through an FEA simulations and experimental verification.

The thermal behavior associated with the DLD process involves numerous reheating cycles. As a result, the temperature history of the deposited materials can be considered as a series of discrete pulses. A 3D transient thermo-mechanical finite model with a moving laser beam was developed to predict the temperature at any location and time during the laser deposition process. Element removal and reactivation technology was used in the modeling to realize the stepwise pattern of material addition.

The FEA model revealed the significant effects of the processing parameters, such as the laser power and travel speed. The results showed that increasing the laser power and/or decreasing the laser travel speed markedly increased the peak temperatures, cooling rates and dimensions of the melt pool.

The model can be used to determine the laser parameters that would assure a constant molten pool temperature consistent with a multilayer deposition and therefore this validation step is critical in the development of this model. A k-type thermocouple was used to measure the temperature history of multiple layers of deposited material. The measurements were qualitatively and quantitatively compared with the prediction of the 3D transient thermomechanical finite model. The model accurately predicted the shape of the heating and cooling curves but had a 20% lower maximum temperature similar to what other experimenters have reported.

In general, the travel speed and laser power were shown to significantly affect the microstructure of the deposited material. The deposition was free of cracks, and the SDAS, ranged in size from approximately 15e35 mm. The microstructure that forms in DLD parts is dependent on the cooling rate of each layer from the peak temperature at a certain point in the peak temperature period. The most important factor in determining the SDAS is the cooling rate that associated with the DLD process. Increasing the cooling rate during solidification could produce deposited material with finer grains. The DLD

process in the same deposition direction exhibited larger temperature gradients than in the reverse deposition direction, and heat diffusion in the same deposition direction was better. The microstructure, as measured by the SDAS correlated very well with the predicted cooling rates of the model, while the hardness did not. The lack of a correlation of the hardness with the microstructure size is attributed to the reheating which occurred when subsequent layers were deposited.

The model calculated that the remelted depth accompanying the parallel laser scanning path would be lower than that for the zigzag path during the first layers to be deposited; therefore, the cooling rate was higher in the parallel path deposition when compared with the zigzag case. The remelted depth increased approximately linearly with layer height up to a total height of 14 mm for both parallel and zigzag cases, indicating that the cooling rate decreases with subsequent layers in this range of height values.

## REFERENCES


[1] J. Kell, J.R. Tyrer, R.L. Higginson, R.C. Thomson, Microstructural characterization of autogenous laser welds on 316L stainless steel using EBSD and EDS, J. Microsc. 217 (2005) 167-173.

[2] Y. Qin, Yi Qin, Neal P. Juster, Advances in Manufacturing Technology XVII, first ed., 2003, p. 132.

[3] Kai Zhang, Xinmin Zhang, Weijun Liu, Influences of processing parameters on dilution ratio of laser cladding layer during laser metal deposition shaping, Adv. Mater. Res. 549 (2012) 785-789.

[4] Xinhua Wu, Jing Liang, Junfa Mei, C. Mitchell, P.S. Goodwin, W. Voice, Microstructures of laser-deposited Tie6Ale4V, Mater. Des. 25 (2004) pp137-144.

[5] Rasheedat M. Mahamood, Esther T. Akinlabi, Mukul Shukla, Sisa Pityana, Scanning velocity influence on microstructure, microhardness and wear resistance performance of laser deposited Ti6Al4V/TiC composite, Mater. Des. 50 (2013) 656-666.

[6] Fu Yao, Xie Shuisheng, X.U. Xiangyang, Huang Guojie, Cheng Lei1, He Youfeng, Optimization of processing parameters for laser powder deposition using finite element method, J. Wuhan Univ. Technol. Mater. Sci. Ed. 25 (5) (2010) 832-837.

[7] Valerio Giuliani, Ronaldo Hugo, Peihua Gu, Powder particle temperature distribution in laser deposition technologies, Rapid Prototyp. J. 15 (4) (2009) 244-254.

[8] Vahid Fallah, Masoud Alimardani, Stephen Corbin, Amir Khajepour, Temporal development of melt-pool morphology and clad geometry in laser powder deposition, Comput. Mater. Sci. 50 (2011) 2124-2134.

[9] Andrew J. Pinkerton, Lin Li, The significance of deposition point standoff variations in multiple-layer coaxial laser cladding (coaxial cladding standoff effects), Int. J. Mach. Tool Manuf. 44 (2004) 573-584.

[10] Jichang Liu, Lijun Li, Effects of process variables on laser direct formation of thin wall, Opt. Laser Technol. 39 (2007) 231-236.

[11] R. Jendrzejewski, I. Kreja, G. Sliwinski, Temperature distribution in laser-clad multi-layers, Mater. Sci. Eng. A 379 (2004) 313e320.

[12] Goodfellow, Metals, Alloys, Compounds, Ceramics, Polymers, Composites, Catalogue 1993/94.

[13] M. Abid, M. Siddique, Numerical simulation to study the effect of tack welds and root gap on welding deformations and residual stresses of a pipe-flange joint, Int. J. Pressure Vessels Piping 82 (2005) 860e871.

[14] R.S. Long, W.J. Liu, F. Xing, H.B. Wang, Numerical simulation of thermal behavior during laser metal deposition shaping, Trans. Nonferrous Met. Soc. China 18 (2008) 691e699.

[15] D. Deng, H. Murakawa, Numerical simulation of temperature field and residual stress in multi-pass welds in stainless steel pipe and comparison with experimental measurements, Comput. Mater. Sci. 37 (2006) 269e277.

[16] W. Jia, H. Tong, W. He, X. Lin, W. Huang, Numerical microstructure simulation of laser rapid forming 316L stainless steel, Acta Metall. Sin. (Chin. Ed.) 46 (2) (2010) 135e140.

[17] Tarak Amine, Todd E. Sparks, Frank Liou, A strategy for fabricating complex structures via a hybrid manufacturing process, in: Solid Freeform Fabrication Symposium, Proceedings of the Twenty Third Annual Solid Freeform Fabrication Symposium, Austin, TX, August 2011.

[18] T.Z. Kattamis, J.C. Coughlin, M.C. Flemings, Trans. Metall. Soc. AIME 239 (1967) 1504.

[19] Jyotsna Dutta Majumdar, Lin Li, Studies on direct laser cladding of SiC dispersed AISI 316L stainless steel, Metall. Mater. Trans. A 40 (12) (2009) 3001-3008.

[20] Didier Boisselier, Simon Sankar e, Influence of powder characteristics in laser direct metal deposition of SS316L for metallic parts manufacturing, Phys. Procedia 39 (2012) 455-463.

[21] J. Dutta Majumdar, A. Pinkerton, Z. Liu, I. Manna, L. Li, Microstructure characterization and process optimization of laser assisted rapid manufacturing of 316L stainless steel, Appl. Surf. Sci. 247 (2005) 320-327.

[22] J. Dutta Majumdar, A. Pinkerton, Z. Liu, I. Manna, L. Li, Mechanical and electrochemical properties of multiple-layer diode laser cladding of 316L stainless steel, Appl. Surf. Sci. 247 (2005) 373-377.

[23] V. Neela, A. De, Three-dimensional heat transfer analysis of LENSTM process using finite element method, Int. J. Adv. Manuf. Technol. 45 (2009) 935-943.

# V. METHODOLOGY FOR STUDYING EFFECT OF COOLING RATE DURING LASER DEPOSITION ON MICROSTRUCTURE

Tarak Amine, Joseph W. Newkirk and Frank Liou

Journal of Materials Engineering and Performance

## ABSTRACT

The present paper focuses on the effect of cooling rate and other processing variables on microstructure and mechanical properties. A specially designed, namely ‘‘step shape,” was used in the current study. The influences of the step thickness were investigated. Results show that the cooling rate is different at different steps and changes the solidification of the deposition process. The cooling rate was deliberately controlled by employing the substrate of varied dimensions. Thermocouples were used to measure the local temperature of the substrate during the deposition process and cooling stage until it reached room temperature. The results of the temperature-time relationship proved the difference in cooling rate. The influence of the substrate dimension on the microstructure and mechanical properties was investigated. The differed cooling rate led to varied grain size and resulted in affected varied hardness and tensile strength. The small samples possessed larger grains sizes formed by a slower cooling rate. The results open the possibility to acquire continuous varied microstructure and mechanical properties by employing a “step shape” substrate.

**Keywords:** Titanium Ti–6Al–4V, Microstructure, Cooling rate.

# 1. INTRODUCTION

Laser direct metal deposition (DMD) has traditionally been used to build small prototypes and in various applications like component repair and short-run component fabrication. The DMD offer a unique combination of process flexibility, time savings, and reduced cost in producing titanium alloy components.

The Laser DMD process features a high cooling rate due to the small processing volume of materials at each location. A number of researches have been conducted on the influence of cooling rate on process quality, microstructure and mechanical properties. All of the previous researches focused on applying a heat treatment after the laser deposition process to obtain a proper microstructure and thus good mechanical properties [1-3]. Shuangyin et al. [1] have studied the effect of the cooling rate on microstructure and mechanical properties of laser deposited Ti-6Al-4V alloy. The samples were solution treated at 900, 950, and 1000 °C, followed by water quenching, air cooling, and furnace cooling, respectively. Karina et al. [2] studied how changing the melt scan rate effected the microstructure and macrostructure for electron beam melting of Ti-6Al-4V. He found that increasing the melt scan rate from 100 to 1000 mm•s−1 in the EBM fabrication of oriented Ti-6Al-4V cylinders increases the cooling (solidification) rate. Shiang et al. [3] also studied the effects of cooling rate on the microstructure and mechanical properties of Ti-6Al-4V. The Ti-6Al-4V was solution heat-treated at 960 °C for 1 hour and then cooling by either by water-quenching immediately or a 2 bar argon atmosphere quench, respectively. Heat treatment after laser deposition in order to change the microstructure of deposited metal will increase the process cost as well as become time consuming.

Titanium alloys are used widely in the aerospace field because of their high strength-to-density ratios, excellent fracture toughness, very good oxidation and good corrosion resistance at temperatures up to 400°C. Ti-6Al-4V is the most commonly used of all the titanium alloys and presents an α+ β titanium microstructure when they are heated, held in the β region and then cooled. Therefore, various transformed microstructures can be obtained depending on the cooling rate. A martensitic structure or fine widmanstatten structure (a mixture of the grain-boundary α phase and side-plate phase) is formed during high cooling rates. When the cooling rate is lower, a coarse

widmanstatten structure is formed. These structures will produce significant differences in mechanical properties. Thus, the cooling rate is understood to play a very important role in predicting the solidification time and grain structure of laser deposition process. The cooling rate has a significant effect on the structure of solidified alloys. The cooling rate determines the characteristic features of the lamellar microstructure, such as the size of α lamellae (α plates), α colony size, and the thickness of α layers at prior β grain boundaries. In general it can be stated that both microstructural parameters, the width of individual α plates and the size of α colonies, decrease with increasing cooling rate [4].

By applying a ‘‘step shape” technique using different substrates sizes, a range of different cooling rates can be obtained. The approach of this work was (1) to investigate the influence of the substrate size on the cooling rate, (2) to study the influences of associated cooling rate attributed using different substrate sizes on the resulting grain size, which in turn will influence the mechanical properties such as hardness and tensile strength, and (3) to characterize the relationship between the microstructure and tensile strength of Ti-6Al-4V across varying cooling rates. This involves comparing the effects of the cooling rates to data from tensile tests.

Moreover, in this work, a transient thermal model for a single laser track build was developed to reveal the temperature distribution and the cooling rate for laser deposits of Ti6Al4V on different sizes and shapes of substrates.

## 2. THERMAL MODELING

A technique named ‘‘step-shape’’, consists of variation of thickness and size of substrates was modeled. The difference in the thickness and the size of the substrate needed to provide an explicit and sufficient way to study the influence of the substrate thickness on the cooling rate behavior during the solidification process.

A 3D finite element temperature field model for direct laser deposition developed by ABAQUS/CAE software demonstrates the model’s thermal history in Ti-6Al-4V. Transient thermal analysis is first performed within ABAQUS/CAE to determine the temperature history at each point of interest in the deposited material. The process parameter used in the model and also in the experimental runs was a laser power of 900 W, travel speed V = 250 mm/min and powder feed rate of 10 g/min. Two cases of substrate were developed in order to meet the desired “step-shape:

### 2.1. FIRST CASE TWO LEVEL STEP SUBSTRATE SHAPE

A single substrate with two level of thickness was investigated first. The idea was to place a single track across the entire substrate and get two distinct and widely varying cooling rates. The dimensions of the step substrate and the transient temperature distribution contour plot for the first deposited layer are illustrated in Fig. 2.1. The cooling rate along a deposited laser track is shown in Fig. 2.2. The step substrate shape doesn’t show a significant difference of cooling rate.

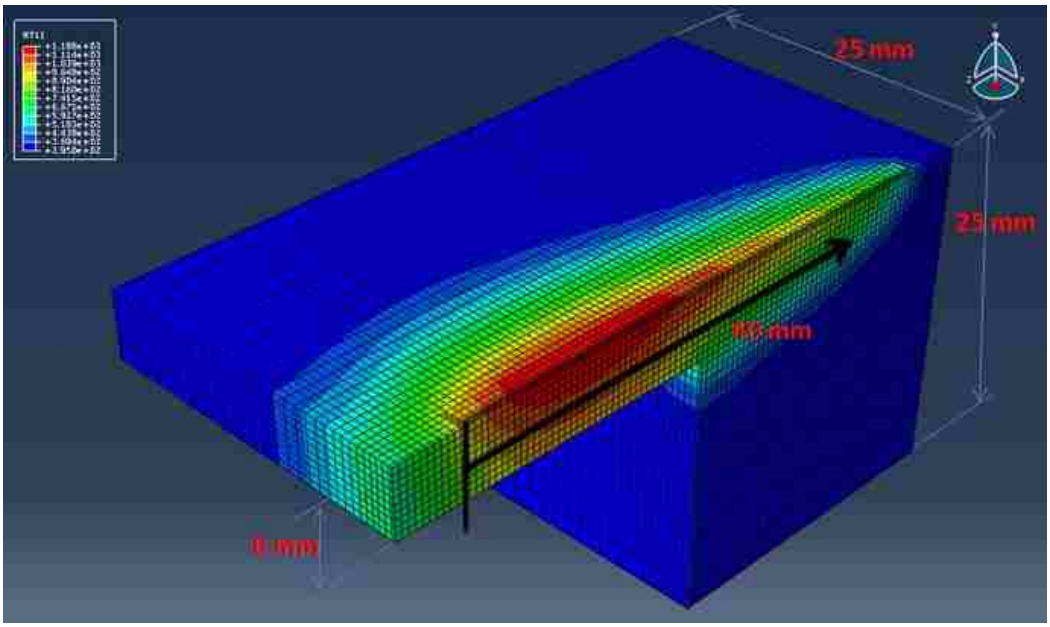


Figure 2.1. Temperature contours for symmetric step substrate shape

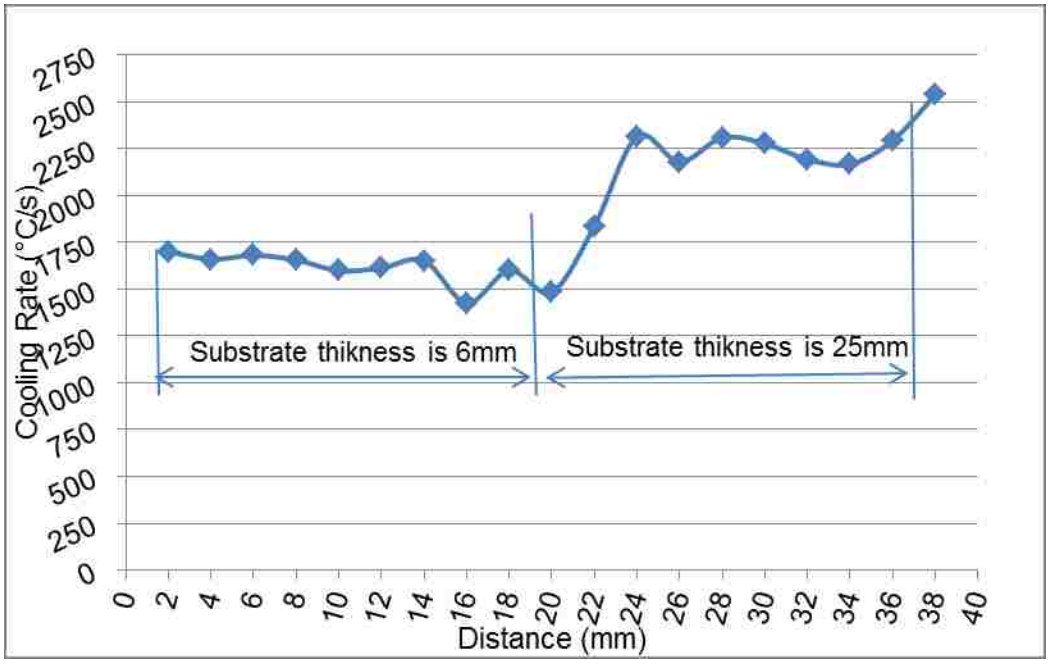


Figure 2.2. The average of the cooling rate along deposited layer

## 2.2. SECOND CASE TWO DIFFERENT SUBSTRATES OF DIFFERENT SIZES

The second idea was to use two different substrates of differing sizes, while depositing sequentially using the exact same parameters. One of the substrates would be significantly larger, resulting in a much higher cooling rate.

**2.2.1. Small Substrate Size.** The dimensions of the substrate are 25*6*4 mm in length, width and thickness, respectively. The transient temperature distribution contour plot for the first deposited layer is illustrated in Fig. 2.3. The average of the cooling rate along laser track is 1500 ºC/s calculated at 890 ºC.

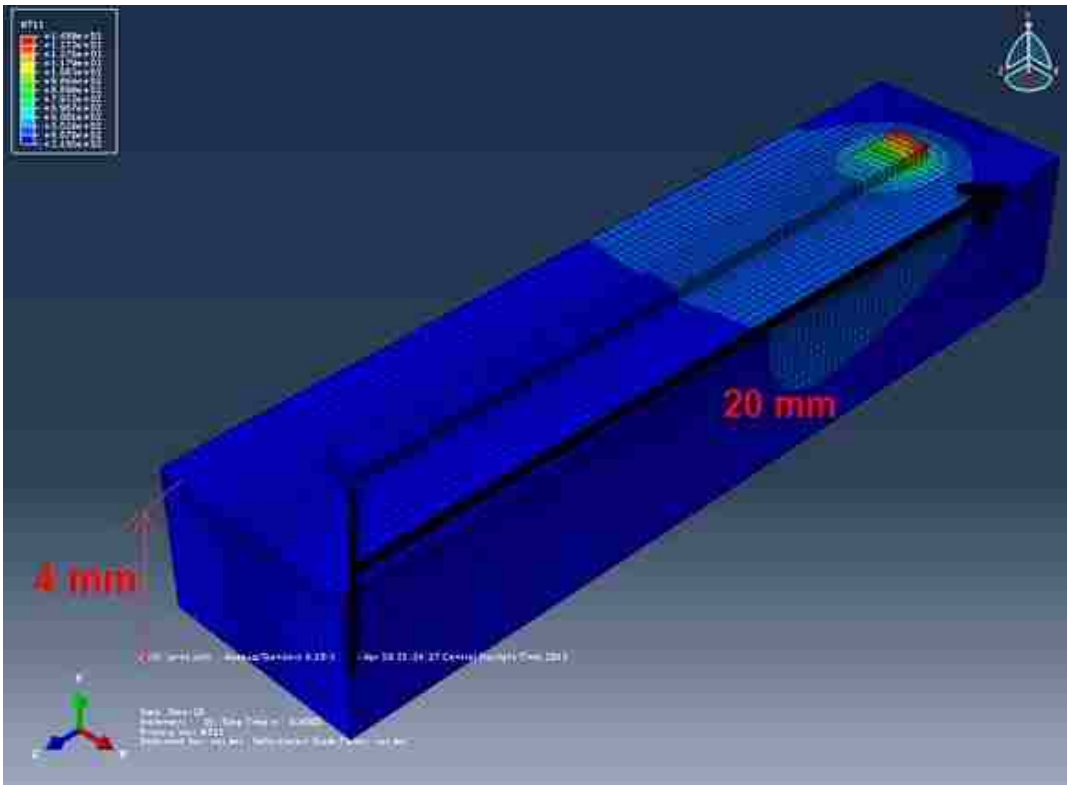


Figure 2.3. Temperature contours for small substrate

**2.2.2. Large Substrate Size.** The substrate measured 50*50*25 mm in length, width and thickness, respectively. Fig. 2.4 illustrates the transient temperature distribution contour plot for the first deposited layer for the large substrate size case. The average of the cooling rate along laser track is 5000 °C/s calculated at 890 °C.

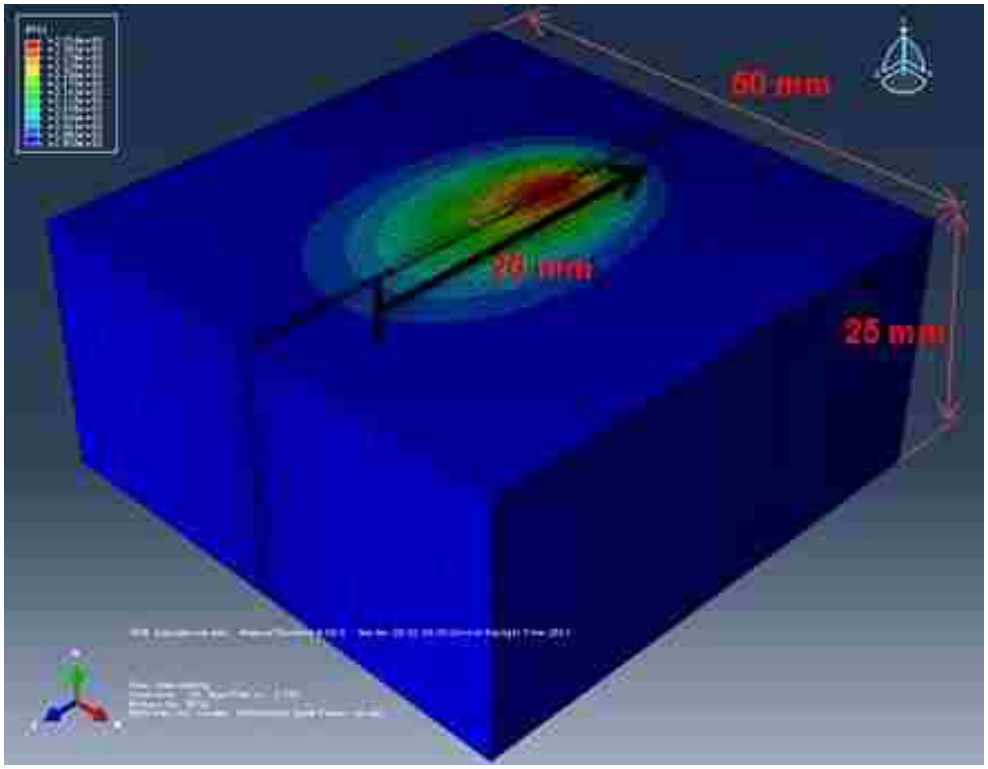


Figure 2.4. Temperature contours for large substrate

# 3. VALIDATION OF MODEL

All of the deposition experiments were conducted at the Laser Aided Manufacturing Process (LAMP) lab at the Missouri University of Science and Technology. The apparatus used for DMD consists of a 1KW diode laser (coherent diode laser), a powder feeder and a 5-axis FADAL computer numerical control CNC (VMC3016). A computer aided design (CAD) file and a CNC control system were used to control the X-axis, Y-axis movement and Z-axis increment. Ti-6Al-4V powder was supplied by Starmet Corp. with size in the range of -60 - 120 mesh. This system has been described in more detail in [5].

In order to validate the model, the temperature history during the (DMD) process was experimentally measured by K-type thermocouples positioned at different depths on the underneath surface of each substrate. The depth of the three thermocouples was 1mm below the top surface of the substrate, as shown in Fig. 3.1. This location was evaluated with the FEA model output as to be sufficiently low in temperatures the thermocouples would not be damaged. These locations will be referred to as the reference positions for the measured temperatures.

The temperatures were recorded with a data logging system at a rate of 100 Hz. The data logging system was initiated prior to the deposition and terminated several minutes after completion of the deposition. In this way, the whole thermal history of the instrumented locations would be recorded, including the deposition process and the cooling period after the deposition. It is essential to keep a constant thermal condition to fabricate parts reproducibly by LAMP technique. The critical thermal parameters include heat gradient and cooling rate, which act as important factors in determining the microstructure evolution. These experiments were used to monitor the heat gradient of the laser track as well as the cooling rate after deposition.

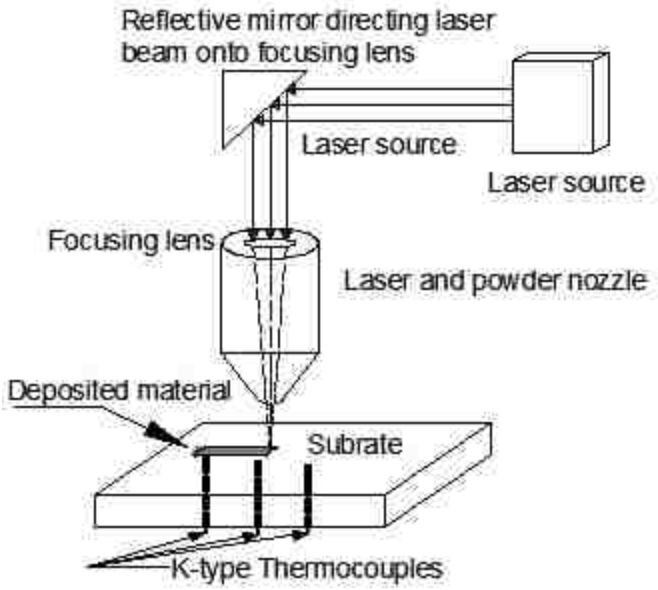


Figure 3.1. Schematics of a direct laser deposition process system, also showing positions of the reference thermocouples

All the samples were deposited with the same amount of total energy (parameters) and same final dimensions except for the cooling rate. The process parameter combinations used are 900W of laser power, 250mm/min of laser speed and 10g/min of powder federate. Each of the designed "step-shape" substrates was evaluated.

**3.1. MATERIAL AND MICROSTRUCTURE**

The substrate material and the powder for deposition is a commercial grade of Ti-6Al-4V. The chemical composition range of Ti-6Al-4V is listed in Table 3.1 To render a sufficient variation in cooling rate, two substrate plates were used with different dimensions, as described above. The large one has a size of 50*50*25 mm in length, width and height, respectively; while the dimensions of the smaller one are 25*6*4 mm in length, width and height, respectively. The offset between the laser head and deposition point was at a constant distance of 5 mm.

For optical microscopy and scanning electronic microscopy (SEM) analysis, samples were mounted, metallographically polished, and etched using Kroll's reagent (2ml HF 4 ml $HNO_3$ 100ml $H_2O$).

Table 3.1. Chemical composition of the Ti-6Al-4V Titanium alloy powder

| Element | Al | Fe | O | C | N | H | V | Si | Ti |
|---|---|---|---|---|---|---|---|---|---|
| Content (W %) | 6.02 | ≤0.15 | 0.13 | ≤0.056 | 0.046 | 0.01 | 4 | ≤0.039 | Rest |

## 3.2. MECHANICAL PROPERTIES

Tensile testing of the as-deposited specimens on each substrate were conducted using a universal testing machine. The tensile testing was conducted at room temperature according to the ASTM E-8. To obtain the displacement equivalent to 0.2% strain, the 226 MPa (113GPa * 0.002) stress line was drawn to intersect with the stress—displacement curve. An offset line for yield strength measurement was then plotted from the x-intercept of the intersection point and parallel to the elastic portion of the curve. The point of intersection of the offset line with the actual curve Stress-Displacement curve thus provides the yield strength value as shown in Fig. 3.2. The results presented are the average from three specimens at each condition.

Hardness tests were utilized to assess the deposited material characteristics. The samples were tested with 100 g load applied for 10 seconds using an automated Vickers hardness tester. Hardness measurements were made on transverse section across the deposited material started from top towards to substrate. Hardness measurements were taken at increment of 100 μm.

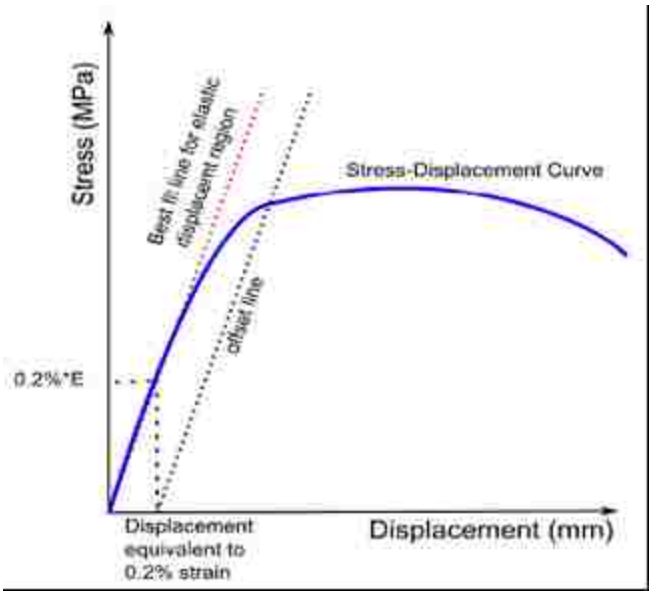


Figure 3.2. Schematic representation for yield strength calculation procedure using the Young's modulus value

# 4. RESULTS AND ANALYSIS

## 4.1. TEMPERATURE DISTRIBUTION

The simulated temperature distribution along the deposited layer and substrate are illustrated in Fig. 4.1, using the laser parameters defined in the caption for both the case of the large and small substrates. The temperature of each nodal point within the solid was calculated as a function of time.

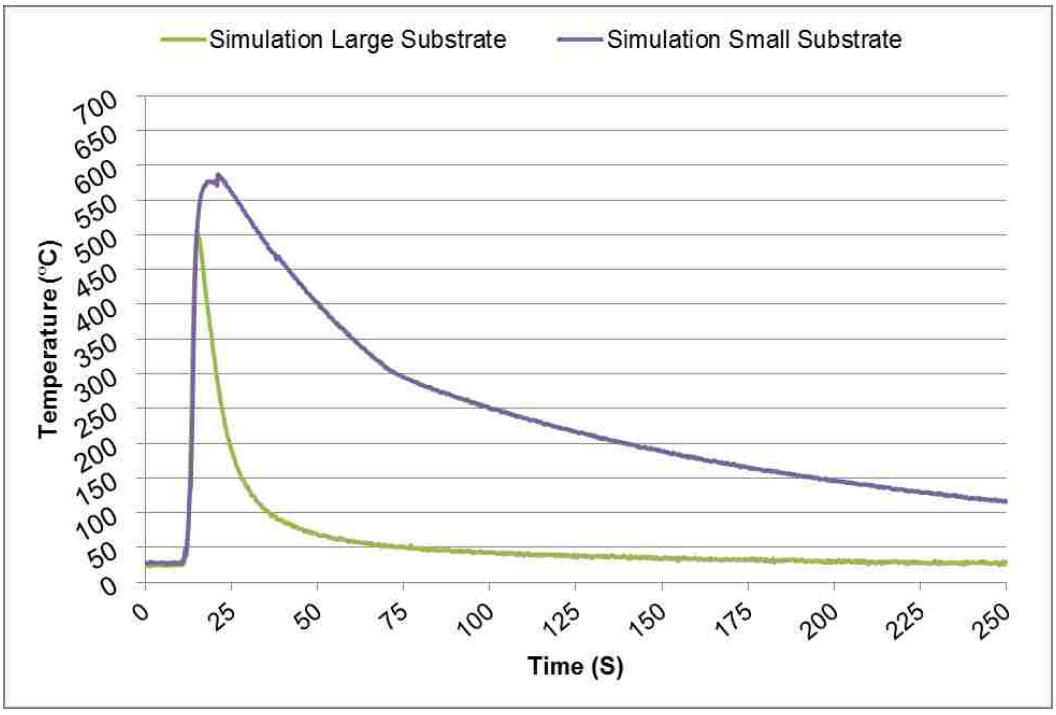


Figure 4.1. Simulation result of temperature distribution of large and small substrates size at element in the middle of laser track 900 W and V = 250 mm/min

Fig. 4.2 shows the measured temperature distribution corresponding to the location at 1 mm underneath the deposited layer for both large and small substrates. The temperature profile shows three stages according to the slope, which corresponded to the thermal history the local material experienced. The temperature peak represents the

thermocouple response as the laser passed over it. The temperature increased when more and more energy was transferred to this position by heat condition. The thermal excursion decays when the energy source moved away from thermocouple position during the deposition of a layer. Since the thermocouples were attached on the substrate, the measured temperatures would be much lower than those actually found near the molten pool. As seen in Fig. 4.3 the simulated results of the temperature distribution are close to the measured experimental results.

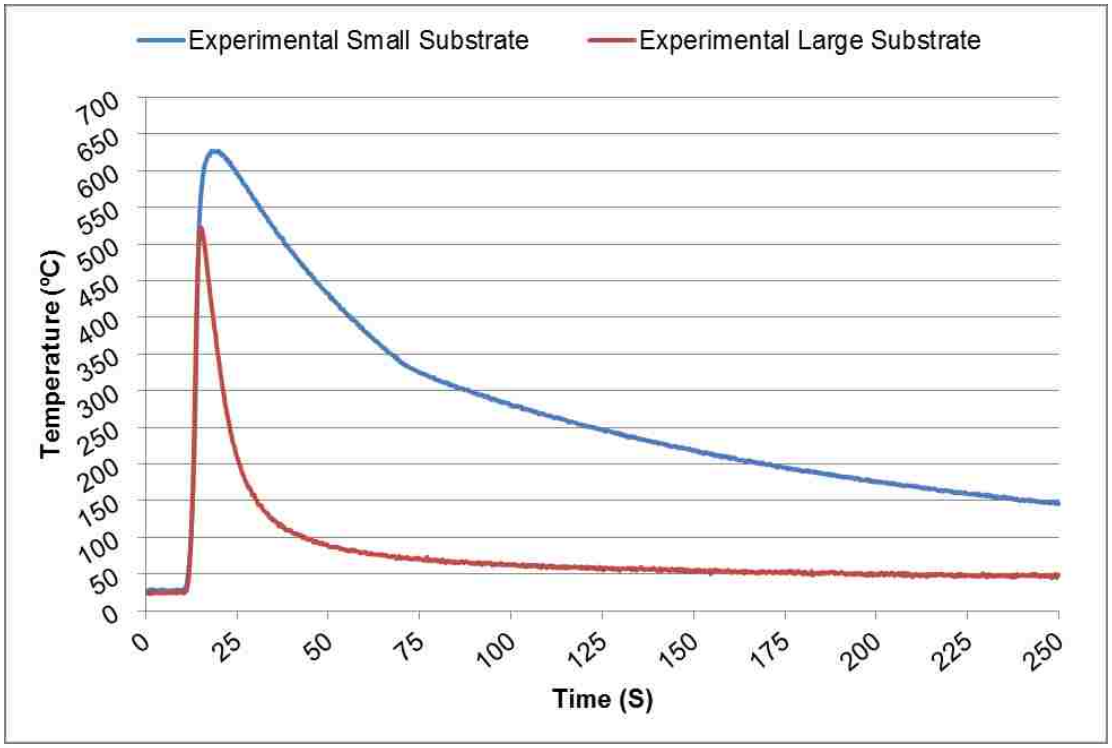


Figure 4.2. Experimental result of heat distribution of deposited material on different substrates size

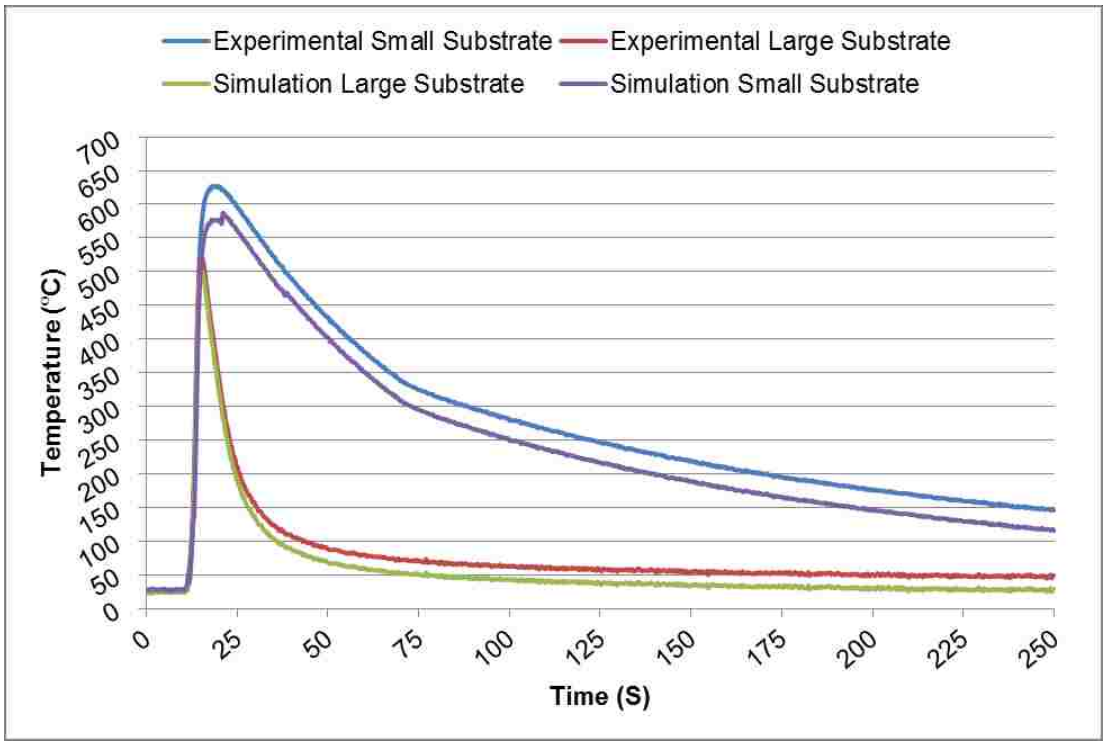


Figure 4.3. Experimental and simulation result of heat distribution for both large and small substrates size

## 4.2. MICROSTRUCTURE

The length and width of more than 20 primary α particles were measured for each specimen to determine the particle length and width, the size distributions, and average particle size.

For the expected Ti-6Al-4V microstructure (Acicular, lamellar, or Widmanstätten), as cooling rate decreases, the α lath thickness is known to increase, leading to lower ultimate tensile strength (UTS), yield strength (YS), and microhardness [6-12].

Titanium is allotropic. It experiences phase transformations at 885 ºC (1625°F) from Hexagonal Close Packed (HCP), to Body Centered Cubic (BCC). Titanium alloys experience phase changes [13] at varying temperatures which depend on the alloying elements and their concentrations. The phase change is characterized by the phase transformation temperature known as the β transus as shown in Fig.4.3 [13]. The β

transus temperature is affected directly by alloying components that act as alpha (α) or beta (β) stabilizers. Hydrogen, for example, is a beta stabilizer, which lowers the β transus temperature. Oxygen, nitrogen, and carbon are alpha stabilizers, which increase the β transus temperature. Metal impurities and alloying elements increase or decrease the β transus depending on the element present. Alloying elements are beta stabilizers if their crystal structure is BCC, much like β-phase Ti. These elements include tantalum, molybdenum, niobium, and vanadium. Beta stabilizer elements do not form intermetallic compounds with Ti. Eutectoid systems can be formed with chromium, aluminum, copper, nickel, and other transition metals. These elements have low solubility in α-phase titanium and act as alpha stabilizers. Together, the β transus temperature can be controlled while taking advantage of mechanical properties given with alloys [14]. The β grain morphology is controlled by the combination of the thermal gradient and the cooling rate. The solidification velocity is related to the thermal gradient and cooling rate by:

Where R is the solidification velocity, G is the thermal gradient, and dT/dt is the cooling rate.

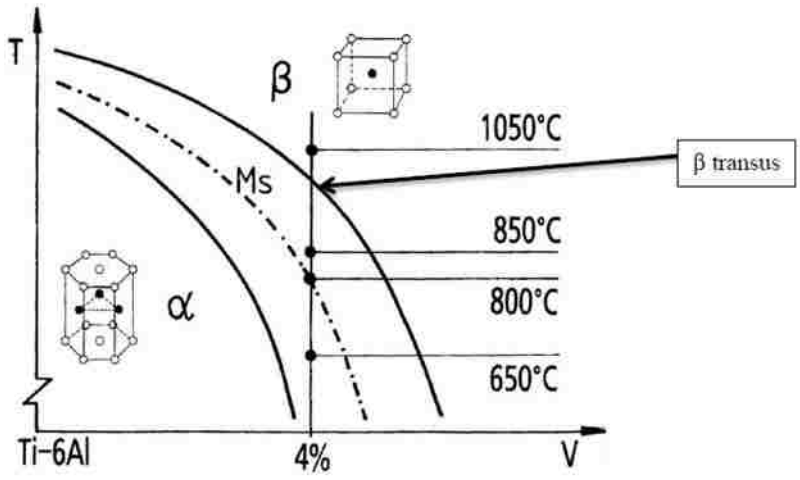


Figure 4.4. Phase diagram of Ti-6Al-4V with unit cells. The β transus marks the minimum temperature where equilibrium α does not exist [13]

The β transus plays a crucial role in determining the microstructure of the alloy. Slow to moderate cooling from above the β transus, for example, leads to the nucleation and growth of α- phase in plate form from β-phase grain boundaries. Slow cooling forms coarse plate-like alpha, whereas air cooling results in finer needle-like α-phase as shown in Fig. 4.4. Figure 4.5 shows SEM micrographs of the deposited Ti-6Al-4V on large and small substrates size.

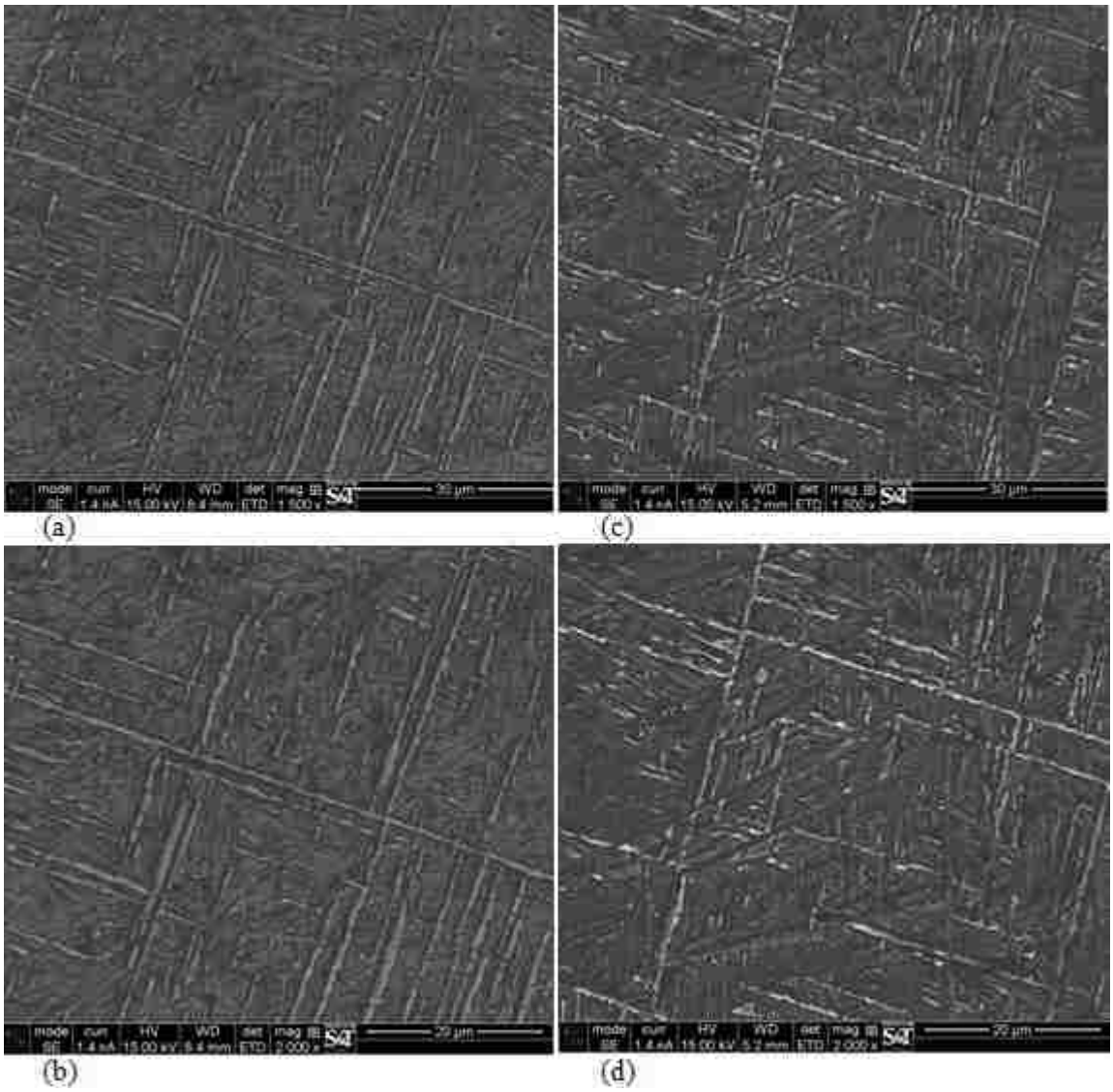


Figure 4.5. SEM micrographs of the Ti-6Al-4V deposit processed by laser deposition, (a,b) deposited on large substrate, (c, d) deposited on small substrate

Fig. 4.6 presents the microstructure of laser-deposited Ti-6Al-4V. The laser deposited Ti-6Al-4V alloys exhibit fully lamellar microstructure, indicating the peak processing temperature exceeded the β-transus temperature. The transformed β microstructure shows basketweave α morphology, which is a typical laser processed Ti-6Al-4V microstructure [15]. It is well demonstrated that laser deposition has high cooling rates, usually in the range of 103 – 106 K/s [16]. At such a high cooling rate, α nucleation

of multiple variants of the Burgers orientation relation becomes dominant and favors formation of the basketweave α over large colony morphology [17].

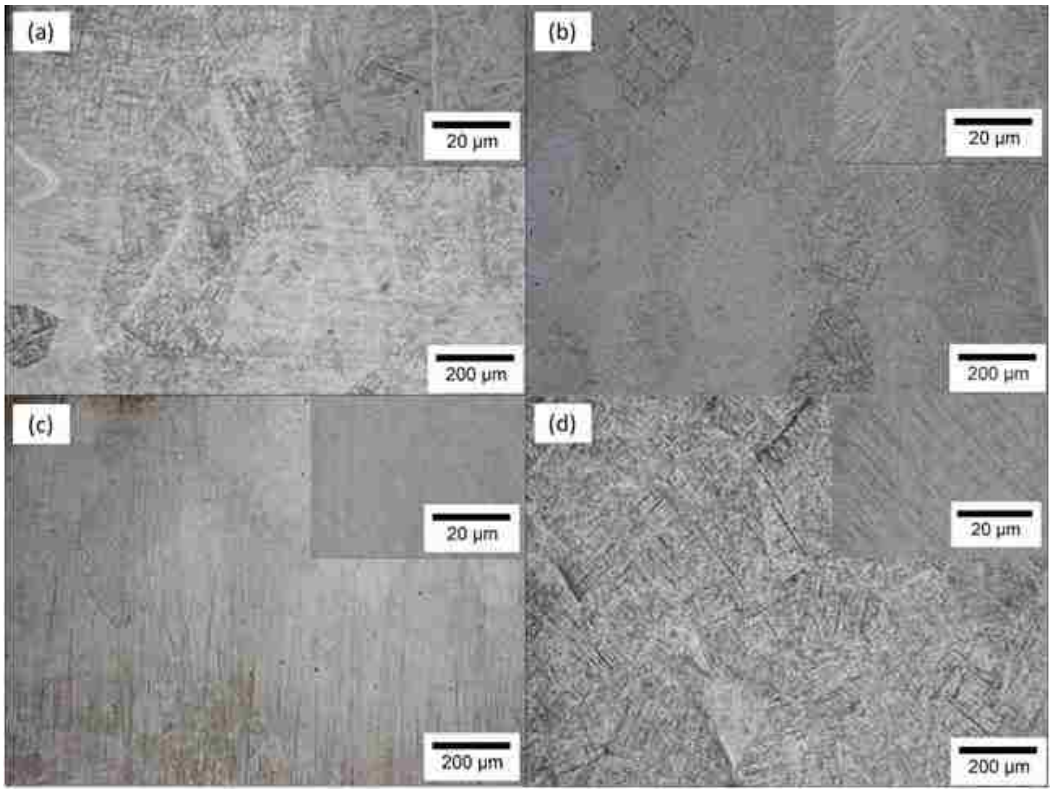


Figure 4.6. Optical microstructure of laser deposited Ti-6Al-4V alloys (a), (b) with small substrate and (c), (d) with large substrate

It is noteworthy that there's a general grain size difference between the deposited layers with different substrate thicknesses. Comparison of the microstructure from the same position in the two depositing as in fig. 4.6b and fig. 4.6d clearly shows the difference. The average prior grain size were ~250 µm and 135 µm in fig. 4.6b and fig 4.6d, respectively. The cooling rate plays a dominant role in determine the prior β grain size in the laser cladding process. In the present work, Ti-6Al-4V substrate acted as the heat sink and the cooling efficiency increased as its size increased. Higher cooling rate restricted the grain growth during solidification and resulted in the finer prior-β grain

size. For phase transformation during further cooling, there's less time for α plate growth under high cooling rate.

## 4.3. MECHANICAL PROPERTIES

The strength of the alloy depends upon the properties and amounts of the phases present in the microstructure. Thus, the observed variation in strength could be explained by considering the changes in the volume fraction of α phase due to processing difference cooling rate.

Mechanical properties of two phase titanium alloys strongly depend on morphology of particular phases. In the case of the alloys with lamellar microstructure, the thickness of α lamellae and diameter of their colonies have the most significant influence [1, 18]. For the expected Ti-6Al-4V microstructure (known as acicular, lamellar, or Widmanstätten), as cooling rate decreases, α lath thickness is known to increase, leading to lower ultimate tensile strength (UTS), yield strength (YS), and microhardness [18-19].

With increasing the cooling rate, the width of primary α lath decreases, the aspect ratio and volume fraction of primary α increases, which make the hardness and tensile strength increases and the ductility decrease [1].

**4.3.1. Tensile Test.** The tensile property results obtained in this work indicate that both σY and σUTS increase when the cooling rate increases from 1500 c°/s to 4500 c°/s. An especially significant increase occurs at cooling rates when different substrate sizes were used compared with step shape substrate as shown in table 4.1.

Table 4.1 presents the results of tensile tests carried out on the several Ti-6Al-4V alloy cooled at different rates. The yield stress was measured at a deformation of 0.2% in compression. The number of grains in the section of different tested samples was measured by ImageJ software observation. The average grains size (D) decreases when the cooling rate increases. This can be readily explained as cooling rate is decreased, the time spent by the alloy in the high temperature a-domain is increased and grains are allowed to grow more. For the deposited on small substrate which had low cooling rate, the dispersion of yield stress results is due to a coarse and heterogeneous structure and to a reduced number of grains in the section of the test pieces. On other hand, for deposited material on large substrate which had high cooling rate, the yield stress gains

homogeneity due to a wholly lamellar and more homogeneous structure. In this cooling rate domain, the average yield stress increases by 25%, from 830 to 1040 MPa. As cooling rates increase the length and thickness of the α-lamellae decrease which leads to higher yield strengths. Elongation remarkable increased from average from 13% to 24% with increase in cooling rate from 1500 ºC/s to 5500ºC/s respectively.

Table 4.1. Tensile strength and hardness results

| Cooling rate | 1500 C°/S | | | 5500 C°/S | | |
|---|---|---|---|---|---|---|
| | **UTS (Mpa)** | **YS (Mpa)** | **Hardness (HV)** | **UTS (Mpa)** | **YS (Mpa)** | **Hardness (HV)** |
| Sample 1 | 845 | 825 | 415 | 1120 | 995 | 405 |
| Sample 2 | 890 | 835 | 425 | 1190 | 1140 | 410 |
| Sample 3 | 850 | 830 | 420 | 1110 | 985 | 400 |

The significant increase in the tensile properties with increasing the cooling rate may be attributed to two main microstructural changes. First, the volume fraction of primary α phase decrease with increasing the cooling rate. Second, the α + β lamellar spacing decreases with increasing the cooling rates [20].

**4.3.2. Hardness.** As seen in table 4.1 the hardness is remarkably affected by the cooling rate. The hardness increased with increasing the cooling rate. The average of hardness of several measured points of deposited material on small and large substrate are 405, 420 HV respectively. The samples have the lowest hardness, which is attributed to the formation of the coarsening α laths.

# 5. CONCLUSION

The current paper focuses on the influence of the cooling rate on the microstructure and mechanical properties in the direct laser deposition process. By applying a “step shape” technique, the investigation of the influence of the step thickness on the cooling rater becomes feasible. Based on such work the following conclusions can be drawn:

- The two level step substrate shape did not have a significant influence on the cooling rate. However, the two different substrates of different sizes resulted in two significantly different cooling rates in the desired range.
- The cooling rate has a notable influence on the microstructure and phase composition of laser deposited Ti-6Al-4V.
- The structure of samples cooled at a rate of 1500°C/sec was studied and showed that increasing cooling rates yield a finer and more homogeneous structure.
- The average length and width of primary α particles decrease and the aspect ratio increases when the cooling rate is increased.
- Ultimate tensile strength and yield strength increase when the cooling rate increase.
- The hardness is remarkably affected by the cooling rate, the average of hardness of deposited material on small and large substrate are 405, 420 HV respectively.
- This “step shape” technique would be applicable to a wide range of alloys, not just Ti-6Al-4V.

## REFERENCES


[1] Zhang, S., Lin, X., Chen, J., & Huang, W. (2009). Effect of solution temperature and cooling rate on microstructure and mechanical properties of laser solid forming ti-6A1-4V alloy. Chinese Optics Letters, 7(6), 498-501.

[2] Karina Puebla, Lawrence E. Murr, Sara M. Gaytan, Edwin Martinez, Francisco Medina, Ryan B. Wicker. Effect of Melt Scan Rate on Microstructure and Macrostructure for Electron Beam Melting of Ti-6Al-4V. Materials Sciences and Applications. 2012, vol. 3, pp 259-264.

[3] Jeng, S. -., & Chiou, H. -. (2013). Effects of cooling rate on the microstructure and mechanical properties of ti-6Al-4V alloy. Applied Mechanics and Materials Vols. 284-287 (2013) pp 103-107.

[4] G. Lütjering, J.C. Williams.(2007) Titanium, 2nd ed.

[5] Amine, T. A., Sparks, T. E., & Liou, F. (2011). A strategy for fabricating complex structures via a hybrid manufacturing process. Paper presented at the 22nd Annual International Solid Freeform Fabrication Symposium - an Additive Manufacturing Conference, SFF 2011, 175-184.

[6] Collings, E.W. The Physical Metallurgy of Titanium Alloys. 1984, Metals Park, OH: American Society for Metals.

[7] Donachie, M.J., Titanium: A Technical Guide. 2nd ed. 1989, Metals Park, Ohio: ASM International

[8] G. Lütjering, J. Albrecht, O.M. Ivasishin: Influence of Cooling Rate and β Grain Size on the Tensile Properties of (α+β) Ti-Alloys, in "Titanium '95", The University Press, Cambridge, UK (1996) 1163-1170.

[9] Lütjering, G. and J.C. Williams, Titanium. 2nd ed. 2007, Berlin: Springer.

[10] Rack, H. J., & Qazi, J. I. (2006). Titanium alloys for biomedical applications. Materials Science and Engineering C, 26(8), 1269-1277.

[11] Tiley, J., Searles, T., Lee, E., Kar, S., Banerjee, R., Russ, J. C., & Fraser, H. L. (2004). Quantification of microstructural features in α/β titanium alloys. Materials Science and Engineering A, 372(1-2), 191-198.

[12] Welsch, G., R. Boyer, and E.W. Collings, Materilas Properties Handbook: Titanium Alloys. 1994, Metals Park, OH: ASM International.

[13] ASM Titanium Alloys, Materials Properties Handbook, ASM International, Materials Park, OH 1994 (p483 - 619).

[14] Davis, J.R. Metals Handbook: Desk Edition Second Edition. Ohio: ASM, 1998.

[15] Kelly, S. M., & Kamper, S. L. (2004). Microstructural evolution in laser-deposited multilayer ti-6Al-4V builds: Part 1. microstructural characterization. Metallurgical and Materials Transactions A: Physical Metallurgy and Materials Science, 35 A(6), 1861-1867.

[16] Vilar R. Laser cladding, Journal of Laser Applications. Vol. 11, No. 2, pp 64-79, 1999

[17] Wanjara, P., Brochu, M., & Jahazi, M. (2005). Ti-6Al-4V electron beam weld qualification using laser scanning confocal microscopy. Materials Characterization, 54(3), 254-262.

[18] Jeng, S., & Chiou, H. (2013). Effects of cooling rate on the microstructure and mechanical properties of ti-6Al-4V alloy. Applied Mechanics and Materials, 284-287, 103.

[19] Gil, F. J., Ginebra, M. P., Manero, J. M., & Planell, J. A. (2001). Formation of α-widmanstätten structure: Effects of grain size and cooling rate on the widmanstätten morphologies and on the mechanical properties in Ti6Al4V alloy. Journal of Alloys and Compounds, 329(1-2), 142-152.

[20] Senkov, O. N., Valencia, J. J., Senkova, S. V., Cavusoglu, M., & Froes, F. H. (2002). Effect of cooling rate on microstructure of ti-6Al-4V forging. Materials Science and Technology, 18(12), 1471-1478.

# SECTION

# 2. CONCLUSION

The temperature field evolution, thermal cycling characteristics, temperature gradient and effects of different deposition directions on the thermal activity of single-pass, multi-layer laser deposition fabrication were investigated through a FEA simulations and experimental verification.

The thermal behavior associated with the DLD process involves numerous reheating cycles. As a result, the temperature history of the deposited materials can be considered as a series of discrete pulses. A 3D transient thermo-mechanical finite model with a moving laser beam was developed to predict the temperature at any location and time during the laser deposition process. Element removal and reactivation technology was used in the modeling to realize the stepwise pattern of material addition.

The FEA model revealed the significant effects of the processing parameters, such as the laser power and travel speed. The results showed that increasing the laser power and/or decreasing the laser travel speed markedly increased the peak temperatures, cooling rates and dimensions of the melt pool.

The model can be used to determine the laser parameters that would assure a constant molten pool temperature consistent with a multilayer deposition and therefore this validation step is critical in the development of this model. A k-type thermocouple was used to measure the temperature history of multiple layers of deposited material. The measurements were qualitatively and quantitatively compared with the prediction of the 3D transient thermo-mechanical finite model.

In general, the travel speed and laser power were shown to significantly affect the microstructure of the deposited material and the deposition was free of cracks. The microstructure that forms in DLD parts is dependent on the cooling rate of each layer from the peak temperature at a certain point in the peak temperature period. The most important factor in determining the grain size is the cooling rate that associated with the DLD process. Increasing the cooling rate during solidification could produce deposited material with finer grains. The DLD process in the same deposition direction exhibited

larger temperature gradients than in the reverse deposition direction, and heat diffusion in the same deposition direction was better.

The model calculated that the remelted depth accompanying the parallel laser scanning path would be lower than that for the zigzag path during the first layers to be deposited; therefore, the cooling rate was higher in the parallel path deposition when compared with the zigzag case.

Moreover this work focuses on the influence of the cooling rate on the microstructure and mechanical properties in the direct laser deposition process. By applying a “step shape” technique, the investigation of the influence of the step thickness on the cooling rater becomes feasible.

# BIBLIOGRAPHY

[1] J. Kell, J. R. Tyrer, R. L. Higginson & R. C. Thomson. Microstructural characterization of autogenous laser welds on 316L stainless steel using EBSD and EDS. Journal of Microscopy, Vol. 217, (2005), pp. 167–173.

[2] Y. Qin, Yi Qin, Neal P. Juster. Advances in manufacturing technology XVII, (1st Edition), page 132, 2003.

[3] S. Ghosh, J.Choi, Modeling and experimental verification of transient/residual stresses and microstructure formation in multi-layer laser aided DMD process", Heat transfer division of ASME, Vol. 128, July 2006.

[4] Valerio Giuliani, Ronaldo Hugo, Peihua Gu, 2010, Powder particle temperature distribution in laser deposition technologies. Rapid prototyping journal, 15/4 (2009) 244-254.

[5] Vahid Fallah, Masoud Alimardani, Stephen Corbin, Amir Khajepour. Temporal development of meltpool morphology and clad geometry in laser powder deposition. Computational materials science, 50 (2011) 2124-2134.

# VITA

Tarak Amine was born on February 5, 1979 in Tripoli, Libya. In June 2001, he received his B.E. in Mechanical and Production Engineering from Altahadi University, Al-Brega, Libya. After graduation, he was employed by National Bureau for Research & Development as manufacturing engineer from January 2003 to July 2008. He enrolled in Tripoli University to begin his graduate study in Production Engineering and received his M.S in December 2006. Following graduation, he came to the Missouri University of Science and Technology, Rolla, Missouri. He was a member of the Laser-Aided Manufacturing Processes (LAMP) Lab. In January 2015, he received the Key Scientific Article contributing to excellence in engineering, scientific and industrial research in Advances in Engineering Ltd. During this period he has held the position of graduate teaching assistance in the Department of Mechanical and Aerospace Engineering. He received his Ph.D. in May 2015.